

Sverre Gauden

Development of an Internally Actuated GFRP Rigid Wing Sail for an Autonomous Surface Vessel

Master's thesis in TMM4960 Engineering Design and Materials

Supervisor: Andreas T. Echtermeyer

June 2021

Sverre Gauden

Development of an Internally Actuated GFRP Rigid Wing Sail for an Autonomous Surface Vessel

Master's thesis in TMM4960 Engineering Design and Materials
Supervisor: Andreas T. Echtermeyer
June 2021

Norwegian University of Science and Technology
Faculty of Engineering
Department of Mechanical and Industrial Engineering



Abstract

Autonomous surface vessels (ASVs) are growing in their capabilities and can serve as valuable tools in oceanographic data acquisition. For long term missions complete energy self sufficiency is key, and propulsion by wind is an excellent contributor to this [1]. Rigid wing sails are much better suited for automated control than traditional fabric sails, but they have been difficult to build rigid and light at a reasonable cost [2]. This challenge is targeted in this thesis, as part of the Oceanographic Research Craft Autonomous (ORCA) project which entails the development of such a vessel.

A glass fibre reinforced polymer (GFRP) rigid wing sail has been developed and a full scale prototype manufactured by means of vacuum assisted resin transfer moulding (VARTM). The wing sits on a fixed mast, and a drive unit situated within the wing facilitates unlimited rotation for enhanced manoeuvrability. The transmission through a worm and worm gear reducer allows the wing to maintain its position without any power consumption. Weather conditions in the open ocean are rough, and the wing has been designed to operate in $20 \frac{m}{s}$ winds.

Through comparative testing against a carbon fibre reinforced polymer (CFRP) wing of equal external size and shape, it is found and concluded that this GFRP wing is between $\frac{1}{2}$ and $\frac{1}{3}$ as stiff with an added mass of 36%. Material costs are reduced by between 55% and 75%. Actuation under loads up to $140 Nm$ is achieved during testing, but it is evident that with a replacement actuator the design load of $211 Nm$ will be reached.

The prototype is left fully functional and ready to be mounted on the vessel hull for sea trials. Through assembly tests the design was shown to be user friendly, and a comprehensive assembly guide ensures that persons unfamiliar with the product may handle it.

Samandrag

Autonome overflatefartøy vert stadig meir velfungerande og kan nyttast som verdifulle verktøy til innsamling av data i verdas store havområde. Skal dei operere over lang tid må fartøya vere sjølvforsynte med energi, og å nytte vind til framdrift er nøkkelen for å oppnå dette [1]. Ved automatisert styring er rigide vingesegl betre eigna enn tradisjonell seglduk, men desse har vist seg å vere krevjande å byggje sterke og lette til ein fornuftig kostnad [2]. Denne utfordringa er forsøkt handtert i denne oppgåva, som er ein del av ORCA prosjektet som har til hensikt å utvikle ein slik farkost.

Eit rigid vingesegl av glassfiberforsterka plast GFRP har blitt utvikla og ein fullskala prototype er produsert ved hjelp av vakuumassistert resinstryking VARTM. Vinga roterer ubegrensa rundt ei mast, ved hjelp av innvendig motor og drivverk. Overføringa skjer gjennom eit snekkegir som gjev tilstrekkeleg utveksling medan ingen straum krevst for å halde vinga fast i ein posisjon. På det opne havet kan vêrforholda bli ekstreme, og vinga er konstruert for å fungere i vind opp til $20 \frac{m}{s}$.

Gjennom komparativ testing opp mot ei karbonfibervinge med same storleik og profil, vart det kome fram til at denne glassfibervinga er mellom $\frac{1}{2}$ og $\frac{1}{3}$ så stiv og 36% tyngre. Innsparinga i materialkostnader vil vere mellom 55% og 75%. Vinga lot seg aktuere under last opp til $140 Nm$. Dimensjonerande last er $211 Nm$, og testdata tyder på at dette vil bli nådd når den delvis dysfunksjonelle motoren bytes ut med ein ny.

Prototypa er fungerande og klar til å samanføyast med skroget for testing på sjøen. Samanstillingstesting har vist at produktet er brukarvenleg, og ei detaljert samanstillingsrettledning vil forsikre at personar som ikkje er kjende med vinga kan handtere henne.

Contents

Abstract	iii
Samandrag	v
Contents	vii
Figures	ix
Tables	xi
Acronyms	xiii
1 Introduction	1
1.1 Autonomous Surface Vessels ASVs	1
1.2 Rigid Wing Sailing	2
1.3 Vacancies in the State of the Art	3
1.4 The ORCA Project	3
1.5 Thesis Research Question and Objectives	4
1.6 Thesis Structure	5
1.7 Thesis Limitations	5
1.8 Foundation	6
2 Theory on Composites and Vacuum Assisted Resin Transfer Moulding	9
2.1 Laminate Theory	9
2.1.1 Laminate Failure	9
2.2 Vacuum Assisted Resin Transfer Moulding VARTM	10
2.2.1 Basic VARTM process description	10
2.2.2 VARTM in Literature	11
2.3 Cutting, Drilling and Machining of Glass Fibre Reinforced Polymer Composite Laminates	13
3 Development	17
3.1 Development of the Wing Structure	17
3.1.1 Foundation	17
3.1.2 Design	19
3.1.3 Modelling	21
3.1.4 Static Analysis	23
3.1.5 Dynamic Analysis	26
3.1.6 Discussion	27
3.1.7 Pre-production Evaluation of Design	29
3.2 Development of the Wing Drive Unit	30
3.2.1 Foundation	30

3.2.2	Worm Gear Transmission	31
3.2.3	Elaboration of Drive Unit Design Criteria	31
3.2.4	Drive Unit Design	33
4	Manufacturing	47
4.1	Making the GFRP Wing	47
4.1.1	Test Infusions	48
4.1.2	Mould Type	49
4.1.3	Mould Design and Manufacturing	52
4.1.4	VARTM of Wing Components	53
4.1.5	Assembly	59
4.2	Manufacturing the Drive Unit	62
4.2.1	Assembly	63
4.3	Estimation of Cost	64
5	Experimental Testing of the Wing Assembly	67
5.1	Experimental Setup and Method	68
5.1.1	Test 1 - Mass	68
5.1.2	Setup	68
5.1.3	Test 2 - Assembly	68
5.1.4	Test 3 - Static Loading	69
5.1.5	Test 4 - Actuation	70
5.2	Results	72
5.2.1	Test 1 - Mass	72
5.2.2	Test 2 - Assembly	72
5.2.3	Test 3 - Static Loading	73
5.2.4	Test 4 - Actuation	76
6	Discussion	79
6.1	Lab tests	79
6.1.1	Test 1 - Mass	79
6.1.2	Test 2 - Assembly	80
6.1.3	Test 3 - Static Loading	80
6.1.4	Test 4 - Actuation	81
6.2	Manufacturing Methods and Cost	83
7	Conclusion	87
7.1	Conclusion	87
	Bibliography	89
A	Wing Assembly Guide	93
B	Mechanical Drawings	107
C	Previous FEA	121
D	Relevant Data Sheets	123

Figures

1.1	ORCA project logo.	3
2.1	Schematic demonstration of the VARTM process.	10
2.2	Mechanisms of delamination in drilling.	14
3.1	Carbon fibre rigid wing.	18
3.2	4-part GFRP wing concept.	18
3.3	Previous wing finite element analysis (FEA) result.	19
3.4	FEA of wing: orthotropic GFRP lamina properties.	22
3.5	FEA of wing: laminate layup visualisation.	22
3.6	FEA of wing: deflection under torque loading.	24
3.7	FEA of wing: Tsai-Hill index under torque loading.	24
3.8	FEA of wing: deflection under pressure loading.	25
3.9	FEA of wing: Tsai-Hill index under pressure loading.	25
3.10	FEA of wing: eigenfrequencies.	26
3.11	Measure to increase the lowest eigenfrequency.	27
3.12	NACA0018 wing profile: $\frac{C_l}{C_d}$ versus angle of attack.	27
3.13	Bevel gear actuation unit for the wing.	30
3.14	Computer aided design (CAD) model of drive unit.	32
3.15	Drive unit component explanation.	33
3.16	RMD-X8 Pro servo motor.	34
3.17	CAD model of the bearing support structure.	35
3.18	FEA of bearing support: stress distribution.	36
3.19	FEA of bearing support, improved: stress distribution.	37
3.20	CAD model of the connection between the worm shaft and motor.	37
3.21	FEA of shaft connection: stress distribution.	39
3.22	FEA of redesigned shaft/motor connection: stress distribution.	39
3.23	CAD model of motor support bracket.	42
3.24	Sealing ring location.	42
3.25	Section view of a BASL sealing ring.	43
3.26	Box bottom plate explanation.	44
3.27	FEA of bottom plate: deflection.	45
3.28	Drive unit enclosure.	46

4.1	EPICOTE™/EPICURE™ resin system temperature development. . . .	48
4.2	VARTM on foam test mould.	50
4.3	GFRP thin skin test mould.	51
4.4	The parts made on the two test moulds.	51
4.5	Mould structure design: profile offset.	52
4.6	Infusion processes of the two laminates for mould making.	54
4.7	Mould assembly stages.	55
4.8	The overlapping joint in a ply oriented at 45°.	56
4.9	Leading edge VARTM process.	57
4.10	VARTM process error: air intrusion.	58
4.11	Abrasive water jet cutting (AWJC)	58
4.12	Flange insertion in wing components.	59
4.13	Solar panel bolting detail.	61
4.14	Bottom section reinforcement.	61
4.15	The sealing ring fitted into the bottom plate.	63
4.16	The drive system assembled.	64
5.1	Full experimental setup for wing stiffness and actuation testing. . .	67
5.2	Experimental setup details: measurements.	69
5.3	Experimental setup drawing: measurements.	70
5.4	Experimental setup details: load and boundary conditions.	71
5.5	Test 3A graphical presentation of results: deflections.	75
5.6	Test 3B graphical presentation of results: deflections.	75
5.7	Test 4 graphical presentation of results: unloaded actuation power consumption.	76
6.1	Motor support bracket, suggested design improvement.	82
B.1	RMD-X8 Pro actuator mechanical drawing.	107
D.1	[0/90] woven fabric data sheet.	125
D.2	RMD-X8 Pro actuator data sheet.	128

Tables

1.1	Wing design objectives.	4
1.2	Thesis research questions and method.	5
1.3	Vessel hierarchy of design goals.	6
1.4	Vessel design requirements.	6
1.5	Wing design specifications.	7
3.1	The results of Dyrseth's [5] GFRP wing FEA.	17
3.2	Data on the acquired solar panels.	21
3.3	FEA of wing: mesh convergence test.	23
3.4	FEA of bearing support: deflection and stress results.	36
3.5	Material properties for the worm shaft and motor connector flange	38
3.6	FEA of motor connector flange: deflection and stress results.	38
3.7	FEA of worm shaft connection: deflection and stress results.	38
3.8	Worm shaft and bearing press fit calculation results.	41
4.1	Summary of VARTM process details.	53
4.2	Summary of components machined for the drive unit.	62
4.3	Cost estimate: VARTM process consumables.	65
4.4	Cost estimate: wing structure.	65
4.5	Cost of purchased drive unit components.	66
5.1	Test 1 results: CFRP wing mass.	72
5.2	Test 1 results: GFRP wing mass.	72
5.3	Test 2 results: wing assembly time.	72
5.4	Test 3A-CFRP results: deflections.	73
5.5	Test 3A-GFRP results: deflections.	73
5.6	Test 3B-CFRP results: deflections.	74
5.7	Test 3B-GFRP results: deflections.	74
5.8	Test 4 unloaded actuation results: current draw.	76
5.9	Test 4 loaded actuation results: function and current draw.	77

Acronyms

- ASV** autonomous surface vessel. iii, vii, 1, 4
- AWJC** abrasive water jet cutting. x, 14, 15, 32, 42, 43, 53, 58, 60, 62, 83
- BLDC** brushless direct current. 33
- CAD** computer aided design. ix, 18, 21, 32, 35, 37, 42, 79, 107
- CAE** computer aided engineering. 21
- CAPRI** controlled atmospheric pressure resin infusion. 11, 12
- CFRP** carbon fibre reinforced polymer. iii, xi, 4, 5, 17, 18, 68, 70, 72–74, 79, 87
- CSM** chopped strand mat. 12, 53, 59, 60
- DBVI** double bag vacuum infusion. 12
- FEA** finite element analysis. ix, xi, 5, 17, 35, 36, 38, 44, 56, 80
- GFRP** glass fibre reinforced polymer. iii, v, viii–xi, 4, 5, 13–15, 17, 18, 22, 44, 46, 47, 50–52, 68, 70, 72–74, 79, 81, 87
- MDF** medium-density fiberboard. 49, 50, 52, 59
- NACA** National Advisory Committee for Aeronautics. 2, 6, 7, 17, 27, 31
- ORCA** Oceanographic Research Craft Autonomous. iii, v, vii, 3–6, 85
- RTM** resin transfer moulding. 11, 47
- SCRIMP** Seemann Composites Resin Infusion Moulding Process. 11
- VARI** vacuum assisted resin infusion. 10, 12
- VARTM** vacuum assisted resin transfer moulding. iii, v, vii–xi, 5, 10–13, 47, 48, 50, 52–54, 57, 65, 66, 84, 87

Chapter 1

Introduction

With our planets climate rapidly changing, acquisition of data is key to understand what is happening and how we should face our challenge. The ocean covers over 70% of the face of the earth and is the worlds larges ecosystem [3], and through oceanographic surveillance our scientists may be supplied with data on weather, oceanic currents, fish stocks, water temperature and acidity etc. The advent of autonomous navigation may provide invaluable service in this respect.

1.1 Autonomous Surface Vessels ASVs

In the last 20 years there have been extensive developments in the field of autonomous sailing, both from commercial and academic instances. Stelzer and Jafar-madar [1] summarise the key characteristics of robotic sailboats as follows:

- Wind is the only source of propulsion.
- It is not remotely controlled; the entire control system is on board.
- It is completely energy self-sufficient.

and the main strengths of unmanned autonomous sailboats for ocean surveillance tasks as

- Long mission ranges.
- Negligible operational costs.
- Potential for towing sensors.
- Real time data transmission.
- Real time data localisation.
- Very low noise generation.

Further, by the vessels being unmanned, people are removed from harms way where extreme conditions makes operation dangerous.

1.2 Rigid Wing Sailing

An object in relative fluid motion will experience some forces acting on it. Very simplified, there is a drag force generated by the object altering the fluid motion, and a lift force normal to this generated by a pressure difference due to fluid particles travelling at different velocities around different parts of the object. By properly orienting an adequately shaped object with respect to the wind, the net resultant force vector may have a component in the desired direction of travel. Through the history of mankind, people have capitalised on this by use of conventional fabric sails for wind generated propulsion [4].

An alternative to fabric sails are rigid wings. The article *Rigid wing sailboats: A state of the art survey* by Silva *et al.* [2] presents a thorough investigation of the latest developments in the field of rigid wing sailboats. They convey the main advantages of rigid wings over traditional fabric sails as their ability to maintain their shape in low wind conditions, better robustness due to the absence of ropes, suffer from less drag, have higher efficiency and can sail closer to the wind. These are aspects that make rigid wings more suitable for automation than fabric sails. The most frequently mentioned drawbacks are the difficulties to build rugged, light and inexpensive wing sails, the fact that their size cannot be reefed in high winds and that wing sails are not particularly stable when sailing downwind [2].

As the vessel must be able to sail with the wind at both sides, symmetrical profiles are common practice. Profiles in the National Advisory Committee for Aeronautics (NACA)00xx series are frequent choices. One of the authors predecessors in this project, Dyrseth [5], used a NACA0018 profile and designed the wing to be a balanced rig. This means that the resultant lift of the wing goes through the centre of the mast, or slightly behind, reducing the power needed for rotation. This is a concept also used in most of the rigid sails mentioned in [2]. Still the actuation, of the rigid wing sail as well as the rudder, is said to often be the most significant power consumer. Therefore, this aspect must be carefully considered. Some have handled this by leaving the wing free to rotate, with a small flap behind the main wing actuated by a modest linear actuator. By actuating the flap, the wing will maintain a certain angle to the apparent wind. Others apply direct actuation, with servos, DC or stepper motors. Little relevant detail on the specific mechanisms is found in the publications. Among common attributes weighted in the literature in regard to both vessel and wing design is the facilitation of simple storage, transport and rigging. Also the buoyancy capability of the wing is emphasised in case of submersion and capsizing.

Neal [6] set out to prove the feasibility of a low-cost and low-complexity autonomous sailing vessel, by the building and testing of a 1.5 m prototype. Along with several later projects, as summarised in [2], they suggest an approximate size of 3 m suitable for a versatile and seaworthy sailing vessel for oceanographic re-

search purposes.

Among successful unmanned sailing vessels in later years is the 2 m long Sail-Bouy by Offshore Sensing, which was the first unmanned surface vessel to cross the Atlantic Ocean [7]. It does not sail autonomously, but can navigate to defined waypoints. The most successful commercial vessel is the Saildrone. Its hull is of a somewhat larger scale, 7 m long, and it has been out on multiple missions spanning over several months doing surveys on fish for fishery authorities and weather for climate scientists, among other things [8]. Common with these and other commercial craft is that they share little or no information on the mechanical structure and actuation of their wings.

1.3 Vacancies in the State of the Art

Silva *et al.* [2] state further work should be invested to improve the reliability and robustness of the vessels, and to ensure that they can stand prolonged periods at sea. They identify a recurring challenge in rigid wing sailing vessels being to build a wing that is structurally rugged, light and inexpensive. Also Neal [6] had earlier pointed to the construction of strong and lightweight rotatable wings at reasonable cost as something needing further investigation. This very subject forms the basis for this thesis. Dyrseth [5] designed a rigid wing sail using carbon fibre PrePreg, which introduces a considerable material cost.

1.4 The ORCA Project



Figure 1.1: ORCA project logo.

This master thesis is a contribution to the Oceanographic Research Craft Autonomous ORCA project. The project is described by its founder A. Echtermeyer as:

[...]a new initiative that will develop a small autonomous vehicle that can be out at sea for very long times(years). The vehicle should be able to perform measurements of water quality, currents, weather etc.[...] This project focuses on the design of such a vehicle, not the instrumentation.[...]

The vision is for the ORCA to serve as a low-cost oceanography platform for long term missions. Its design should be suitable for batch production.

A few different people have been involved in the project since its initiation in the fall of 2019. Gården Rovik [9] wrote a project thesis exploring various overall design solutions for an ASV. As already mentioned in Section 1.2, a master thesis on the development of a carbon fibre reinforce polymer CFRP rigid wing was written by Dyrseth [5] in 2020. Her work will reoccur frequently through this thesis, both as a foundation to build on, and as something to compare up against.

The author wrote a project thesis last year, S. Gauden, ‘Development and prototyping of an ocean going autonomous surface vessel for research applications,’ 2020, available from the author or his supervisor. The relevant results of this will be further discussed in Section 3.1.1 and Section 3.2.1.

A. Brandal has worked along side the author for the past year with the main focus in his thesis on the hull and rudder of the boat. L. Digerud has been working with the development of a hydrogenerator.

1.5 Thesis Research Question and Objectives

Can glass fibre reinforced polymer GFRP be used to build a rigid wing sail with comparable performance to the carbon fibre wing developed by Dyrseth [5] while adhering to the design objectives in Table 1.1?

- 1 Rigidity
- 2 Low mass
- 3 Low cost
- 4 Assemble/disassemble easily
- 5 Design for manufacturing
- 6 User friendly

Table 1.1: Wing design objectives.

To explore this research question a design has been developed, a prototype

has been manufactured and lab tests concerning stiffness, mass and actuation have been performed. This is be summed up in Table 1.2.

Table 1.2: Thesis research questions and method.

Questions:	Relevant design objectives
Can a GFRP design compare to the CFRP wing?	1, 2, 3
Can this be manufactured in a reasonable manner?	3, 4, 5
Answer these questions by:	
Developing, manufacturing and testing a wing.	
Developing, manufacturing and testing a drive unit.	
With the intention of:	
Leaving a functional prototype for the future of the project.	4, 6

1.6 Thesis Structure

Chapter 1 introduces the concepts and argues for the applicability of this thesis. The research question and method is stated. A brief introduction to previous work and other contributions to this project is presented.

Chapter 2 introduces some relevant theory on laminate composites and the manufacturing method of Vacuum Assisted Resin Transfer Moulding VARTM.

Chapter 3 goes through the development and documents decisions made in creation and analysis of a design.

Chapter 4 handles the manufacturing of the prototype.

Chapter 5 contains experimental testing, describing the setup and results.

Chapter 6 brings a discussion on the results of the experimental testing, the suitability of the design and the manufacturing methods.

Chapter 7 summarises what is learnt through the thesis and poses some concluding remarks.

It is assumed that the reader has basic understanding of mechanics, finite element analysis FEA and common engineering materials.

1.7 Thesis Limitations

A paramount objective is to leave future project and master thesis students in the ORCA project with a functioning physical platform. This elevates the importance of prototype production, which has been very time consuming, on the expense of detailed design, analysis and optimisation. This also affects the academic level of the thesis, as a very practical approach has been utilised.

Despite entailing the development of a wing, this thesis does not analyse nor discuss any aerodynamics. On this aspect, the author places his full faith on the work of his predecessor Dyrseth [5], and the fact that the NACA wing profile used has been thoroughly investigated for many decades.

The aspect of fatigue of the metal components in the actuation mechanism is not properly addressed. The design is intended as a functional proof-of-concept, and should be reevaluated before long term deployment.

1.8 Foundation

In the earlier startup phase of the project, a set of requirements and a hierarchy of design goals were determined for the vessel as a whole, respectively Table 1.3 and Table 1.4

Table 1.3: Vessel hierarchy of design goals.

- 1 Durability
- 2 Cost
- 3 Ease of manufacturing
- 4 Ease of repair
- 5 Stability
- 6 Manoeuvrability
- 7 Environmental friendliness
- 8 Speed
- 9 Seaworthiness/Certification

Table 1.4: Vessel design requirements.

Design aspect	Requirement
Approximate vessel size	3 m
Minimum service speed	1.5 $\frac{m}{s}$
Energy consumption	Less than or equal to energy generation
Maximum apparent wind speed	20 $\frac{m}{s}$
Lifetime, supervised	25 years
Lifetime, unsupervised	1 year

Out of all the aspects which together form the ORCA vessel, this thesis handles the sail structure, i.e. what exists from the top of the hull and up. An extreme case loading condition for the wing was derived from the design requirements. Under 20 $\frac{m}{s}$ winds the wing should be able to turn normal to the wind, without the structure or actuator failing. In the simplest way possible, an object acted on by a

Table 1.5: Wing design specifications.

Wing Specs	
Profile	NACA0018
Cord length	1200 <i>mm</i>
Height	2400 <i>mm</i>
Design wing load	691 <i>N</i>
Design torque	211 <i>Nm</i>
Safety Factor	≥ 2

fluid may be seen in terms of its area. The theoretically largest force F_w exerted on the area A by a fluid of density ρ and velocity v coming to a halt is [4]

$$F_w = \frac{1}{2}\rho v^2 A. \quad (1.1)$$

With the wing dimensions in Table 1.5 and extreme load condition this yields a wind load $F_w = 691 \text{ N}$ causing a torque about the mast axis $T = 211 \text{ Nm}$. It was earlier decided that a safety factor towards failure $SF \geq 2$ should be achieved for any component or mechanism. If this is not the case, a proper contemplation on why the result is acceptable should follow. However, in certain instances for the purpose of proof-of-concept prototyping, this demand is not as strictly observed.

A wing design was suggested and performed an initial feasibility study on by the author in S. Gauden, ‘Development and prototyping of an ocean going autonomous surface vessel for research applications,’ 2020. This is elaborated in Section 3.1.1 and further developed and concretised in this thesis.

Chapter 2

Theory on Composites and Vacuum Assisted Resin Transfer Moulding

2.1 Laminate Theory

Laminate theory can be seen as a basic requirement to understand composite behaviour. In this thesis it was mainly used to determine suitable composite lay-ups in Section 3.1.3 and Section 4.1.4. Should the reader feel the need for a recap of this, some is available in the authors own project thesis [10] and in composite textbooks like [11].

2.1.1 Laminate Failure

Failure of a composite is a complex subject. As the properties are so different in tension and compression and in different directions, conventional von Mises stress stops making sense. There is also the question of how to define a failure. In a composite laminate one often refers to first ply failure. Abaqus provides 5 different lamina failure criteria and among these the Tsai-Hill index was used in Section 3.1.4. The criterion is defined as

$$I_F^{T-H} = \left(\frac{\sigma_L}{\sigma_{Lx}} \right)^2 + \left(\frac{\sigma_T}{\sigma_{Tx}} \right)^2 - \frac{\sigma_L \sigma_T}{\sigma_{Lx}^2} + \left(\frac{\tau_{LT}}{\tau_r} \right)^2 \leq 1, \quad (2.1)$$

where σ_L , σ_T and τ_{LT} are longitudinal stress, transverse stress and in plane shear stress respectively. σ_{Lx} , σ_{Tx} and τ_r are the respective limit stresses, with the x referring to tension or compression. $I_F^{T-H} > 1$ indicates failure. Near free edges and discontinuities, the conditions for such failure theories become invalid due to edge effects. In-plane shear stress and in-plane normal stresses go to zero,

while through thickness shear stress rises to a peak. This may lead to initiation of delamination [11].

2.2 Vacuum Assisted Resin Transfer Moulding VARTM

VARTM is an open mould polymer composite manufacturing process. A vacuum source creates a pressure difference with respect to the atmospheric pressure, which pulls the resin into a fibre preform. It is the pressure difference between the vacuum and the environmental pressure that compacts the preform fibre into the shape of the mould by the flexible vacuum bag. A schematic representation of the process with relevant nomenclature can be found in Figure 2.1. The standard procedure followed at the NTNU Polymers and Composites Lab is presented in Section 2.2.1 before an investigation into the literature in Section 2.2.2. This section is of utmost relevance, as the production method of VARTM is repeatedly applied in the making of wing components in Section 4.1. The process goes by many names, and the term vacuum assisted resin infusion (VARI) is also used frequently. However, VARTM is used in this thesis as this seems to be the most general term for the process occurring across literature.

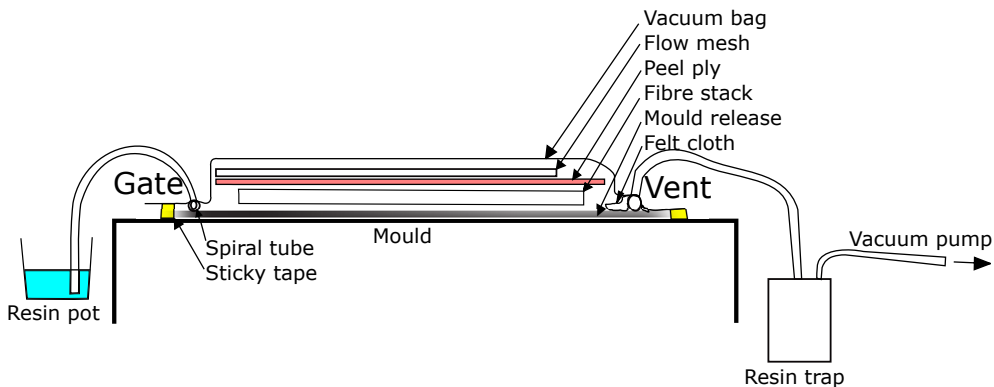


Figure 2.1: Schematic demonstration of the VARTM process.

2.2.1 Basic VARTM process description

- Start off with a smooth, clean and tight mould surface.
- Adhere masking tape along the mould edges before applying a mould release agent to the entire surface within the area. Mould release comes in shape of a liquid to be applied in multiple layers or a wax.
- Remove the masking tape and apply sticky tape along the perimeter, without removing the protective paper.
- Place the fibre preform stack.
- Place the peel ply atop this. Make sure it is larger than the fabric.

- Add flow mesh. The amount and placement of this will vary with the individual processes. Generally, you want contact with the gate so there's no bottleneck there for the resin flow.
- Prepare the gate with spiral tube for resin distribution. Cover the vent with felt cloth to prevent the vacuum bag from being sucked in and stopping air flow.
- Apply the vacuum bag and carefully seal all edges and openings.
- Connect the vent tube through a resin trap to the vacuum pump.
- Clamp the gate tube, and start the vacuum pump. Make sure there are no leakages.
- Mix the resin thoroughly. De-gas it in a vacuum chamber to remove air trapped within.
- Place the end of the gate tube into the resin pot and remove clamp.
- The resin will now flow in through the gate. The flow front advances rapidly in the flow mesh, before the resin is pulled down into the fibres and eventually saturates the fibre tows through capillary effects.
- When resin reaches the vent, you clamp it. If there are still some dry spots, you may let it continue, as excess resin will be caught in the resin trap.
- Make sure both gate and vent are properly clamped, and let the part cure.

2.2.2 VARTM in Literature

Resin transfer moulding (RTM) is a closed mould process. Contrary to VARTM the resin is not pulled into the mould by a vacuum at the vent, but pushed in by increasing the pressure at the resin reservoir. Hand lay-up is an open mould process where fabric and resin is applied manually layer by layer. According to Hsiao and Heider [12] VARTM combines the benefits of high quality, repeatability and clean handling of RTM with the advantages of flexibility and scalability of open mould hand layup processing, allowing for complex large composite parts of high quality.

Many variations of vacuum assisted resin transfer moulding processes have been developed by academic and commercial actors. Van Oosterom *et al.* [13] performed an objective comparison of 6 different methodologies, some of which contain noteworthy features. The introduction of a consumable flow media in the stack, patented as Seemann Composites Resin Infusion Moulding Process (SCRIMP) in 1990, comes with significantly reduced infusion time, and is a widely used form of resin infusion. This is what was referred to as flow mesh in the process description above. In controlled atmospheric pressure resin infusion (CAPRI), the fibre layup is cyclically compacted by vacuum 10-20 times prior to infusion. This decreases the stack thickness and increases the fibre volume fraction that can be achieved at a set vacuum level. Subsequently, the infusion is performed in a vacuum chamber at $\frac{1}{2} atm$. This reduces the pressure difference across the laminate, and hence reduces the thickness gradient. CAPRI achieved the highest fibre volume fraction in the test, with no significant variation between inlet and outlet.

Double bag vacuum infusion (DBVI) utilises two vacuum bag chambers to increase vacuum integrity and reduce laminate relaxation. However, its benefits are contested.

Rydarowski and Koziol [14] performed a comparative study of the repeatability of VARTM processes and hand layup. They proved that the VARI/VARTM method may be advantageous over hand lay-up, showing distinctively better repeatability with respect to volume fraction and mechanical properties. The fibre volume fraction, flexural and impact strength of plain weave fabric is comparable with the two methods, but for chopped strand mat chopped strand mat (CSM) they showed that VARTM yields a fibre fraction $\frac{1}{2}$ higher and flexural and impact strength $\frac{1}{3}$ higher than by hand lay-up. The two latter properties being dependent on the first, both on a local and global scale. Both methods show a gradient towards the centre of the board. VARTM additionally has a distinct gradient towards the direction of the vacuum. Although comparable properties were attained by both methods, the coefficient of variation in the properties was shown to be much more advantageous in laminates obtained by VARTM. This can at least in part be attributed to the more frequent occurrence of local technological flaws in hand lay-up laminates.

Hsiao and Heider [12] mention several aspects to be kept in mind when designing and performing a VARTM process.

- Typical fibre volume fraction achieved by VARTM is 40 – 50%, and mainly depends on the preform. The cyclic compressing and relaxing of the preform, as introduced above in CAPRI, will better compact it, so to achieve higher fibre fraction.
- The flow process design includes, but is not limited to - locations and number of vents and gates, locations and sizes of flow distribution lines, type, number of layers and locations of flow distribution medium, timing to open/close gates/vents. In some cases one might want to control the vacuum pressures of different vents to steer the resin flow.
- Resin viscosity is temperature dependent. Mould and room temperature control may be factors to consider.
- Vacuum pressure can never be true zero, hence there is always a considerable chance of air entrapment inside final composite parts. Causes for dry spots: resin reaches vents before all air inside preform is displaced, resin becomes too viscous to flow before filling mould, leakage. Also microvoids may form, due to the incompatible dual scale flow behaviour of the wetting process inside fibre tows, controlled by capillary effects, and in the gap between the tows, governed by Darcy's law.
- With the transparent vacuum bag, this paper poses the possibility of spotting a dry spot as it occurs, and drawing the air out with a vacuum needle.
- A disadvantage of the VARTM process is the high chance of air leakage, which is highly dependant on worker's skill, which may cause dry spots or

incomplete infusion.

- Once the resin reaches the vent, one may allow some extra resin to be bled out for a few more minutes to remove tiny air bubbles in the flow front. To maintain uniform pressure, keep the vent open after closing the inlet to maintain the vacuum, leading to a more even thickness part.
- VARTM mould filling slowing down issue can be mitigated by using a thicker flow distribution medium layer, using a flow distribution layer with higher permeability or using a fibre preform with higher through-thickness permeability.
- It is possible to perform an analytical assessment of the flow to be helpful in process design, determining: locations of gates and vents, arrangement and selection of flow distribution medium, mould filling time and flow front region profile. For large or complex structures this may be useful.
- A longer time between completion of resin filling and resin gelation will permit a more complete relaxation process and a more uniform VARTM part. Using more vents, or switching injection gates into vents during post-filling compaction relaxation stage can also accelerate the compaction relaxation process.
- Due to low thermal conductivity and exothermic thermoset reaction, the centre temperature of thick composite panels can rise quickly. Out of control thermal spiking can cause thermal degradation of resin, cracks due to expansion, deformation of part due to non-uniform thermal-mechanical evolution. Reaction rate increases exponentially with temperature. Thick parts can be manufactured through multiple sequential VARTM processes, to avoid this problem.
- Spring-in is a dimensional infidelity problem where residual stress or strain causes curved parts to bend inward after demoulding. The spring-in angle is typically in the range of $1-4^\circ$ for a 90° curve-shaped part. The angle can if necessary be predicted analytically to modify the mould.

All this information is helpful when designing and performing the VARTM processes in Section 4.1.4.

2.3 Cutting, Drilling and Machining of Glass Fibre Reinforced Polymer Composite Laminates

Machining and processing of composites pose difficulties due to their heterogeneity and anisotropy. As it cuts through the material, the tool continuously encounters alternate matrix and fibre materials, which may behave entirely different in response to machining [15]. In the GFRP laminates considered in this thesis these are soft epoxy and brittle glass. The following considerations are of relevance in the post-processing of the composite parts in Section 4.1.

Kavad *et al.* [16] defines two main modes of delamination associated with tra-

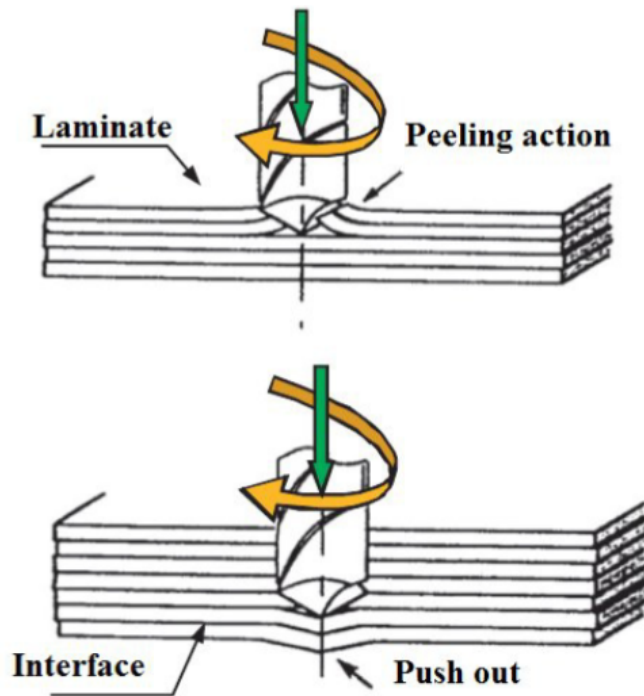


Figure 2.2: Mechanisms of delamination: peel-up at entrance and push-out at exit [16].

ditional drilling of GFRP laminates, namely peel-up at entrance and push-out at exit, visualised in Figure 2.2. Peel-up delamination is generated as the drill flute cuts through the upper plies in the laminate. The tangential force at the circumference acts through the slope of the drill flute, yielding an upwards component which separates the upper laminae from the lower ones held in place by the thrust force. Push out delamination occurs as the drill bit is about to exit the laminate. As the uncut thickness gets smaller, a point is reached when the thrust force exceeds the interlaminar bond strength. Push-out delamination has been proven to be the more severe problem.

In conventional drilling, machining at higher speed, with harder tool material and lower feed rate lessens delamination of the GFRP. The use of High Speed Machining is suitable to assure low levels of delamination. More advanced drilling methods may further reduce the problem. Vibration assisted drilling and Ultrasonic assisted drilling are superior alternatives as they have lesser thrust [16]. In any case, backup support at entrance and, more importantly, exit is a recommended measure to limit the delamination.

Abrasive water jet cutting AWJC is an unconventional machining process where rough abrasive particles mixed with water are ejected at high pressure and velocity through a jet nozzle. Material is removed by erosion. With objective of achieving

high material removal rate, straightness in the kerf and less taper angle, Kumar *et al.* [17] recommend to machine with high jet pressure, low standoff distance and moderate feed rates for desirable results. The procedure is performed with computer numerical routing on two dimensional thin plates. A known problem in AWJC of composite laminates is the delamination at initial penetration, in a similar manner to the push-out mechanism described in the above paragraph regarding drilling.

Komanduri [15] names tool wear as a considerable limitation when machining GFRP composites, due to the abrasive action by the glass fibres on the cutting tool. A dull tool will in turn dissipate considerable heat into the workpiece, negatively affecting the polymer matrix. Local heating of work piece is an important issue in machining overall, as polymers in general have low thermal conductivity and are vulnerable to changes in temperature. Conventional cutting and abrasive material removal methods are also prone to induce delaminations, and adjustments of process parameters will often be a trade-off between avoiding this and overheating problems.

Chapter 3

Development

This chapter goes through the development of the wing and its mechanism of actuation, and is split into two main sections. First the structure of the wing is described, analysed and discussed, before the drive unit is presented in a comparable manner.

3.1 Development of the Wing Structure

3.1.1 Foundation

Dyrseth [5] developed a Carbon Fibre Reinforced Polymer CFRP wing with a NACA0018 profile, shown in Figure 3.1. This was mass optimised for a prescribed stiffness. She assessed the structure for a load case where the wing was in the lift condition, which means the resultant force acts more or less through the mast axis. Table 3.1 lists the results from her static finite element analysis FEA. The theoretical weight of the wing was calculated to 4.5 kg including mast. For the manufactured prototype this is far from the truth, and is further addressed in regards to a comparative performance test in Chapter 5.

Table 3.1: The results of Dyrseth's [5] GFRP wing FEA.

Load Case	Resultant Force [N]	Total deflection [mm]	Tsai-Wu failure index
1	43.76	1.66	0.027
2	218.8	8.46	0.134

In the authors project thesis [10] a new wing design was suggested, and its feasibility investigated for through FEA. Building on the work done by [5], the same area and profile was maintained. The redesign made was to better the agreement with two important objectives, with reference to Table 1.1.

- Objective 3, keeping low cost by changing material from CFRP to GFRP.



Figure 3.1: (a) Assembly of the CFRP wing. Notice the specific placement of the internal structure. (b) CFRP wing atop catamaran test hull.

- Objective 4, facilitating transport and storage by being possible and easy to disassemble/assemble.

A CAD model of the wing design is shown in Figure 3.2. The wing is made up of 4 main parts - leading and trailing edge plus two side panels. A simple internal structure ensures the required rigidity. Other benefits of this design are access to the internal of the wing and possibility to replace one part if damaged. Building the wing like this also better ensures the intended wing profile is attained, compared to a two part wing joined at the tips.

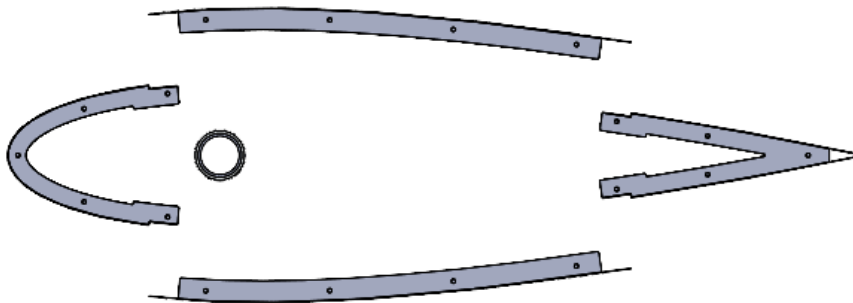


Figure 3.2: The GFRP wing design comprised of 4 main parts - leading edge, trailing edge and side panels.

A key feature distinguishing this design from Dyrseth's [5] initial design is that the wing rotates around a fixed mast, instead of the mast being integrated into the wing and rotate within the hull. This is to lower the complexity of the hull, reducing the risk of water leakage into the vessels main body of buoyancy. By doing so, the actuation of the wing is re-positioned, from within the hull to within the wing. Also, bending forces about the mast base can to a large extent be transferred by the mast itself, reducing load on the wing structure. A 70 mm extruded aluminium profile of 4 mm thickness was then found to be suitable. Ex-

truded aluminium was chosen due to low cost, off-the-shelf availability and good corrosion resistance. A larger diameter was not used to better fit within available bearings, gears etc. A fixed mast going through the whole wing and coming out on top allows instruments mounted aloft, e.g. wind sensor, to follow the orientation of the vessel. More detail on the design in Section 3.1.2.

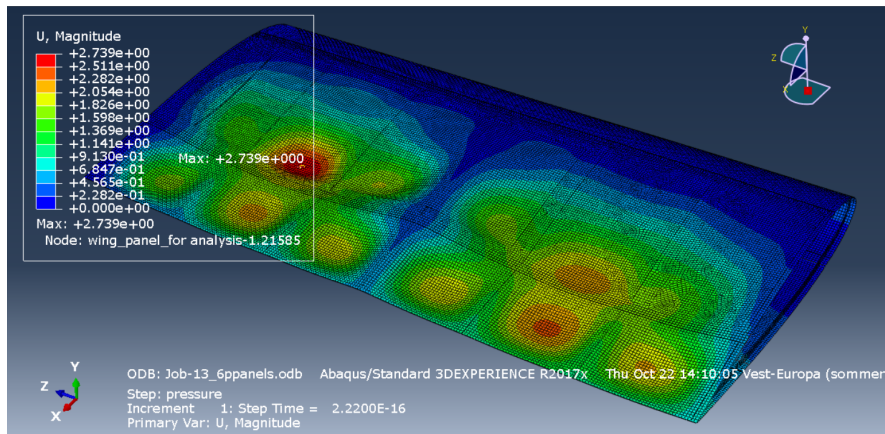


Figure 3.3: Deflections visualised for an earlier analysis of the wing. $[0/90/90/0]$ layup amounting to 1 mm for the skin. Structure supported on three points and subjected to 700 N distributed as pressure.

The previous analysis campaign was conducted in a manner where the skin layup was reduced step by step over multiple analyses with different load cases. A table summarising these is available in Appendix C. Figure 3.3 visualises the deflection due to a load case with a 700 N distributed load acting on the wing on a 3-point support, i.e. the bottom fixed and middle and top sections allowed to slide and rotate. This should, according to the design load case in Table 1.5, correspond to worst case face load, and had the skin caving in up to 3 mm . A skin thickness of 1 mm and 2 mm internal structure thickness ended up looking feasible. With the same load and wing attached to the aluminium mast encastered at base, deflection amounted to 23 mm .

3.1.2 Design

Design

The flanges in the internal structure serve the purpose of maintaining the shape of the skin. Their exact placement has little impact on the torsional stiffness. They are equally spaced, close enough to prevent the skin from caving in. The number 7 seemed to suffice, with reference to Figure 3.3. At top and bottom, solid sections close the wing. An additional section at the middle provides added rigidity.

The flanges are to be adhered to the skins with epoxy and glass fibre. The 4 wing parts plus sections are bolted together.

The bottom section plate is radially and axially fixed to the mast through a bearing. The drive unit also sits fixed to this section plate, controlling the rotational degree of freedom with respect to the mast. At the middle and top wing section plates, sliding bearings limits only the radial translation.

Making the whole wing a sealed compartment is very difficult. However, it is desirable that it remains buoyant in itself. The idea is therefor to fill the vacant space within with airbags, balloons, bubble wrap or similar to displace the volume.

The density of the epoxy resin is approximately $\rho_{epoxy} = 1.1 \frac{g}{cm^3}$, and for glass the number is $\rho_{glass} = 2.5 \frac{g}{cm^3}$. Assuming a 50% fibre fraction, the density of the composite is $\frac{1.1+2.5}{2} = 1.8 \frac{g}{cm^3}$. Multiplying this with the volume calculated by *SolidWorks* yields a total wing mass of 14.97 kg. This is without accounting for extra mass added by the assembly epoxy and fibre. Mast and solar panels also come as an addition.

Solar Panel Incorporation

If the vessel is to remain self-sufficient, as highlighted by [1] and set as a design requirement is Table 1.4, harvesting energy from the sun is key. The wing provides a large area which may be utilised for this purpose.

According to Sharma [18], the conversion efficiency of solar panels is almost constant between angles of incidence of 0-45° and is reduced by 1.7% at 60°. Beyond 60° efficiency drops sharply [19]. At our latitude in Trondheim, the noon sun angle with respect to the horizon stays within this domain all year round. Travelling south to the Mediterranean and Rome, the noon sun angle exceeds 60° from May through July [20]. Hence, the feasibility of vertically mounted panels for power generation is there, but both location and season must be considered in the accounts of power. This, however, is outside the scope of this thesis.

To comply with objectives, a suitable solar panel should be available off-the-shelf at a reasonable price, be rated for marine environments, thin, light and semi-flexible to follow the curvature of the wing profile. Several options were considered in the power area of 100-200 W. Table 3.2 summarises the main data on the 150 W panels that were acquired. To seamlessly integrate the solar panel, the wing side panels are indented according to the respective dimensions.

Table 3.2: Data on the acquired solar panels.

Product Name	Gotland 150 watt
Manufacturer	SunWind
Power	150 W
Dimensions	1480x540x2.5 mm
Mass	3.65 kg
Charging Current	9 A
Charging Voltage	12 V
Price	NOK3499

3.1.3 Modelling

Solidworks has been used for modelling. The software tool used for structural analyses was *DS Abaqus computer aided engineering (CAE)*. Based on the pre-mentioned results in Section 3.1.1, a new round of analyses was performed in *Abaqus*. The model was rebuilt from the bottom up, for better confidence in its correctness. Some features were simplified in comparison to the earlier model, and other more accurately depicted.

Model Set Up

Some simplifications to the wing were made in the CAD model for analysis. The indentation for solar panels in the side panels was removed. This feature had earlier proved to complicate the meshing. By default, an indentation stiffens a thin plate by increasing its second moment of area. Thereby, this simplification should not affect the validity of the analysis. Further, the bolt holes were removed to be re-defined as discussed below.

The geometry was exported from *Solidworks* as .STEP files, and imported into *Abaqus*. To assign a composite laminate layup requires a shell model. Therefore, the middle surface was extracted from the geometry, so that the model could be converted. The flanges were connected to the skin by using tie constraints. One should keep this constraint in mind when interpreting the results in Section 3.1.6. Consistent definition of constraint master and slave node regions is a prerequisite for the analysis to run properly.

Mesh-independent fasteners were used to simulate the bolted connection points. According to *Abaqus* documentation [21], mesh-independent fasteners couple layers of material to each other, without requiring the coupled region to be separated by a partition. Instead their location is defined by attachment points. To define the location of multiple fasteners, patterns of attachment points may be created. In this case, the distance from an edge and number of points over the length is sufficient to fully define the positions. Any nodes falling within a set radius of the

point are included in the constraint. Using this constraint means assuming the shear forces occurring at the connections do not exceed their capacity, i.e. no slip.

Static ply properties for an unidirectional orthotropic glass fibre-epoxy lamina were defined according to Figure 3.4. Values stem from Echtermeyer *et al.* [22].

E1	E2	Nu12	G12	G13	G23
44600	1700	0.262	3490	3770	3460

(a)

Ten Stress Fiber Dir	Com Stress Fiber Dir	Ten Stress Transv Dir	Com Stress Transv Dir	Shear Strength
1240	774	43.9	179	55.8

(b)

Figure 3.4: (a) Elastic and (b) failure properties of the orthotropic GFRP lamina, as defined in Abaqus. The unit is MPa for all except the unitless in-plane Poisson's ratio Nu12.

According to laminate theory various attributes of the composite layup affects the behaviour of the laminate, and quasi-isotropic layups that are either symmetric or anti-symmetric are viable for the wing. The possible layups were dependant on available fabrics. The intention was to use $[0/90]$ woven roving and $[\pm 45]$ biaxial fabric. Adjacent $[0/90]$ UD plies were used to simulate woven roving, which is standard practice and its validity argued for by Lasn *et al.* [23].

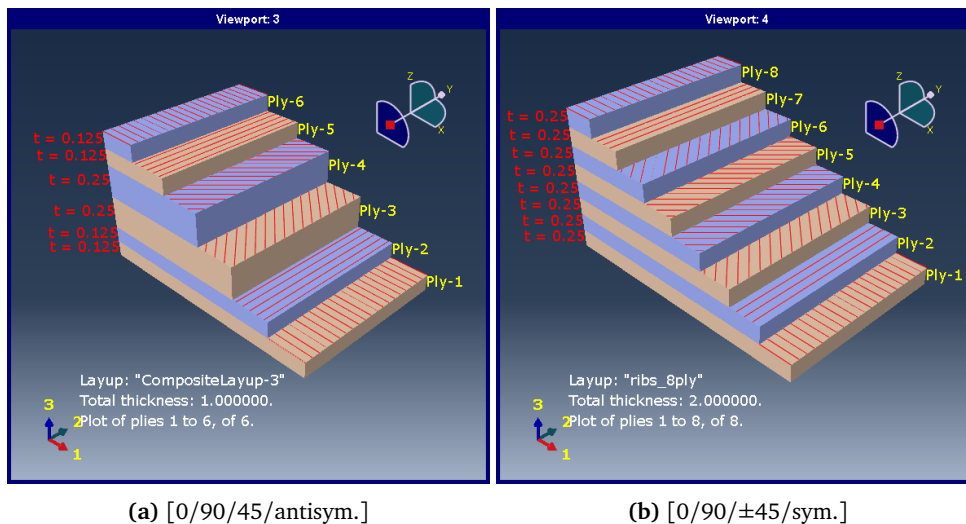


Figure 3.5: Visual representation of the laminate layup used for the skins(a) and internal structure(b).

At this development stage, the exact fabrics and their suppliers were not set.

The layups were created to reasonably coincide with available known products. This is further discussed in Section 4.1.4. Adjacent $[0/90]$ plies of 0.125 mm emulate one ply of 0.25 mm thick woven roving. Adjacent $[\pm 45]$ plies equalate one 0.5 mm biaxial fabric. Figure 3.5a visualises the layup assigned to the skin regions, which amounts to 1 mm . Figure 3.5b displays the 2 mm thick laminate for the internal structure components.

Mesh

The mesh is quad dominated, with thin shell elements. This means the mesh will consist mainly of S4R elements, while allowing the meshing algorithm to use S3 elements where the geometry requires it.

This design is mainly driven by stiffness, not strength, so a convergence test with regards to displacement is conducted. The test is performed on the leading edge part only. This part contains the complicated geometric features occurring in the various parts of the assembly, and a converged mesh coarseness of this part should indicate the applicability of the same mesh size on the other parts. The part is fixed at one end and loaded with a 1 N test load on the other. Table 3.3 shows the deflection at one certain node, and relative processing time. The results scatter within 1.3% deviation between the largest and smallest deflection, but show no declining or increasing trend. This can be interpreted as to that convergence of deflection to some extent is already occurring at the coarsest considered mesh. As the cost of refinement is reasonable, the global mesh size of 10 mm was chosen.

Table 3.3: Convergence test results for the wing leading edge. Processing time is given relative to that of the elected element size.

Global mesh size, mm	20	15	10	2
Deflection $\times 10^2$, mm	7.77	7.73	7.67	7.77
Relative processing time	0.33	0.5	1	17

3.1.4 Static Analysis

Torque

The torsional stiffness of the wing is important, in order for the wing to maintain its shape and orientation. A pure torque is applied to a reference point on the mast axis at the top of the wing. The reference point is coupled to the top flanges. The bottom flanges are coupled to another reference point at the bottom of the mast axis. This point is encastered. Applying a pure torque, i.e. the dimensioning torque of 211 Nm (211000 Nmm), to the top yields the results in Figure 3.6.

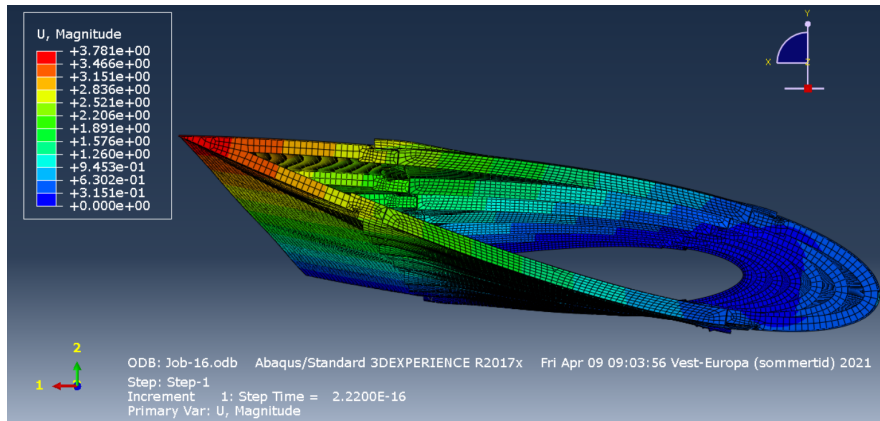


Figure 3.6: Deflection of the wing subject to 211 Nm torque about the mast axis.

Maximum deflection is 3.78 mm. This corresponds to an approximate relative rotation of the wing profile of $\theta = \arcsin \frac{3.78}{900} = 0.24^\circ$. The Tsai-Hill index remains below 0.1 in all nodes, i.e. far less than the $I_F^{T-H} \leq 0.5$ providing the required safety factor of 2 in this project. Through thickness visualisation of the Tsai-Hill index in one of the most highly stressed elements is shown in Figure 3.7. The element is located on the side panel along the middle flange.

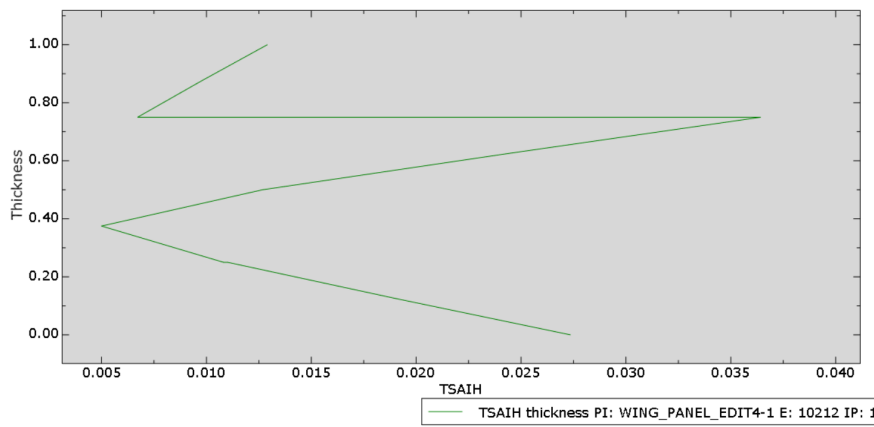


Figure 3.7: Through thickness distribution of the Tsai-Hill index at a highly stressed element in the skin over the side panel middle flange.

Pressure

With a thickness 1 mm, the panels have very low bending stiffness about the weak axis. In order to look at the resistance of the external shape towards caving in, an analysis under pressure was performed. The skin caving in between the supporting structures/flanges may be a problem. A 2000 N distributed load was applied

over the surface of the whole exterior wing, i.e. both sides. The symmetric surface load should result in deflection symmetric about the XZ plane. The internal sections at the middle and ends are considered infinitely rigid in this analysis.

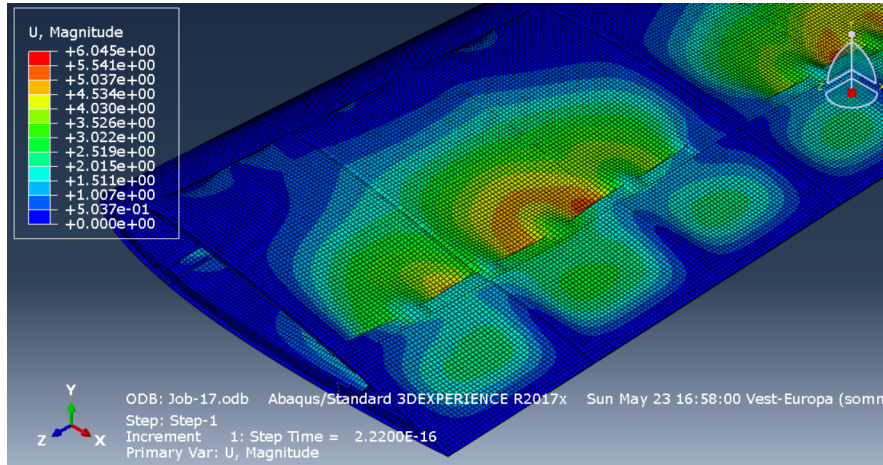


Figure 3.8: Deflections of the wing skin subject to pressure.

The largest deflections occur between the bolts along the interconnection between the trailing edge and the side panels, up to 6 mm at the most, as seen in Figure 3.8. The Tsai-Hill index reaches its highest values in at the mesh-independent fasteners, with a value of 0.1 and through thickness distribution as shown in Figure 3.9.

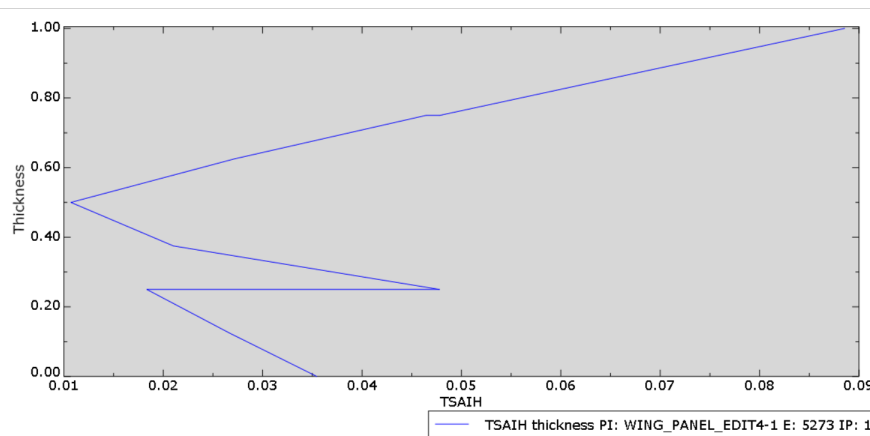


Figure 3.9: Through thickness distribution of the Tsai-Hill index at a highly stressed element near a bolt.

3.1.5 Dynamic Analysis

The wing was supported as a 3 point beam, fixed around the hole of the bottom section and allowed to rotate and slide at middle and top.

Initial Analysis Results

Figure 3.10 displays the first four eigenmodes.

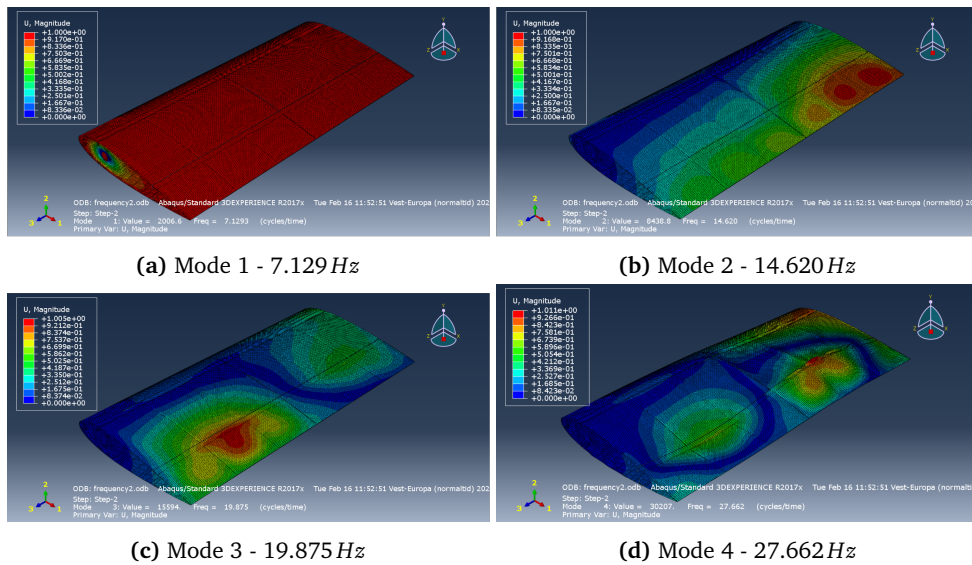


Figure 3.10: The 4 first eigenmodes attained in the initial frequency analysis of the wing.

Design improvement

The lowest eigenfrequency of 7 Hz was due to the deflection of the bottom plate, where the wing is constrained to ground. To push this mode up to a higher frequency, the bottom plate was reinforced as shown in Figure 3.11. Such a structural improvement drastically increases the second moment of area of a thin plate.

Re-analysis Results

The frequency of the first mode was increased by the addition of the stiffeners, to 14.932 Hz. The other modes are not affected by this alteration, such that the twisting mode at 14.650 Hz remained the lowest eigenfrequency.

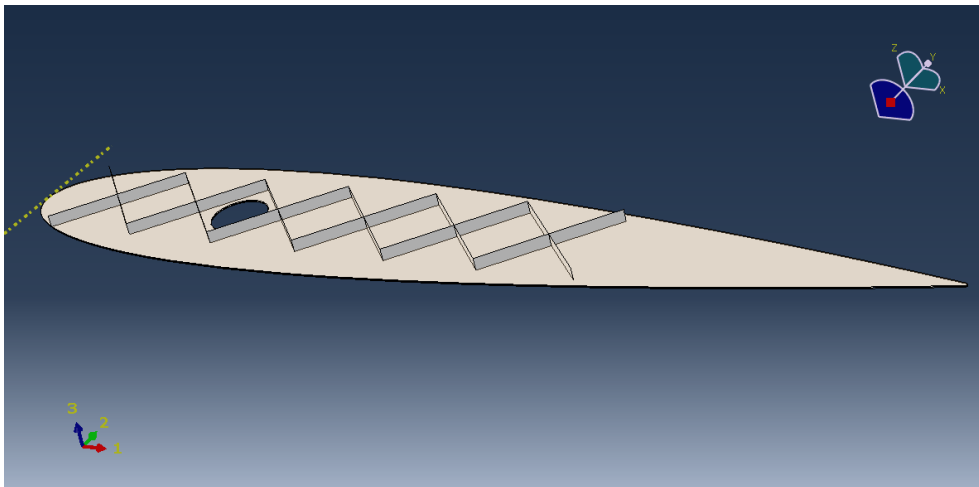


Figure 3.11: The bottom plate of the wing stiffened to increase the lowest eigen mode.

3.1.6 Discussion

Torque

A 0.24° rotation of the airfoil section under this load is low. In a lift condition, looking at the lift/drag ratio with respect to angle of attack in Figure 3.12, this alteration of the orientation is close to negligible.

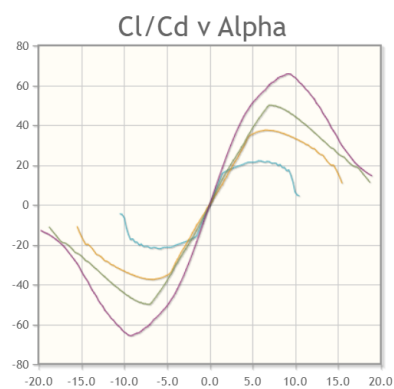


Figure 3.12: Coefficient of lift over coefficient of drag with respect to angle of attack for a NACA0018 at various Reynolds numbers, which correspond to different speeds. Figure taken from [24].

There are a few aspects that can lower the faith in these results. The boundary conditions are quite rigid and are limiting certain movements of the structure in an unrealistic manner. Modelling the sections as rigid is one example. Their compliance to compression is indeed very low, but they might allow some twisting movement in reality.

As mentioned in Section 3.1.3, it is assumed that the bolted connections hold. This assumption has not been investigated, and could turn out to be incorrect.

The flanges, which are tied in the model, will in reality be adhered, meaning the fixture strength essentially is the strength of epoxy. This has not been looked at in detail, and the lamina failure index brings little enlightenment here. The epoxy has a tensile strength $\in (60-75) \text{ MPa}$ according to the data sheet [25], while the dominating stress component $S_{11} < 30 \text{ MPa}$ in the highest stressed elements of the skin close to the bottom and middle flanges. The other components S_{22} and $S_{12} < 4 \text{ MPa}$. This should serve as an indication that the joints will hold. Further, dependant on the amount of fibre reinforcement used in the joints, the load will be distributed over a larger area, reducing stress.

Pressure

The results show that the caving of the panels is most extensive towards the trailing end of the wing profile. This is expected, as this is where the curvature is smallest. It must be kept in mind that in this model, the contact in the interface between the side panels and the edges is not accounted for. They are only connected in the fasteners. This could provide some additional support in the most deflected areas in the wing.

The dimensioning face load was in Section 1.8 calculated to 691 N one-sided, Table 1.5. A deflection of 6 mm can be acceptable for the stalled wing in storm conditions. In lift situations maintaining the shape is more important. The panels on the negative pressure side will experience tension, while on the positive pressure side there is compression. Resulting deflection will make the profile slightly asymmetric, which should not have a negative effect on the wing behaviour. The forces are also smaller in the lift condition, referring to the loads reported by [5] in Table 3.1.

The linearity of the I_F^{T-H} -distribution in the upper 0 and 90 plies of Figure 3.9 indicate bending about both axes. According to the deflections this makes sense.

Frequency

One should consider environmental dynamic stimuli that might coincide with the structures lowest eigenfrequency. Water/wave motion is the first thing of interest. The experienced dynamic stimulation from this may be assumed to have a much lower frequency for a vessel with such low intended speed, i.e. $1.5 \frac{\text{m}}{\text{s}}$ as of Table 1.4. Vibrations caused by rotating machinery aboard the vessel should be considered. The wing actuator, presented in Section 3.2.4, has a peak operating speed of 225 rpm or 3.75 Hz , making it of no concern. Aerodynamic forces may

have a dynamic influence under certain conditions, but this is outside the scope of this thesis.

The frequency analysis is done for the wing structure only. Assembling with the mast and a finitely rigid connection between these will alter the dynamic. The total system will have lower eigenfrequencies.

3.1.7 Pre-production Evaluation of Design

These two isolated load cases analysed are not analogue to any real life situations. In a general sailing load case, the torsional deflection will add up with the face deflection and the deflection of the mast. However, if the magnitude of these attained analyses results is in the vicinity of the truth, the design looks promising in regards to stiffness.

From the very simple dynamic analysis and little knowledge about the total system, having the mode 1 eigenfrequency of torsion about the mast at 14Hz is good.

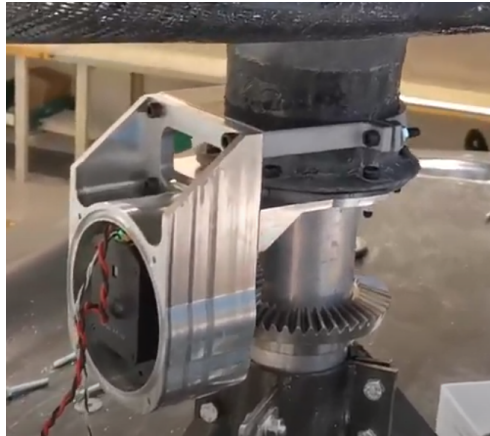


Figure 3.13: Bevel gear actuation unit for the wing.

3.2 Development of the Wing Drive Unit

3.2.1 Foundation

Figure 3.13 shows the direct actuation drive unit made by the author during the project thesis [10].

The transmission between motor and mast happens through bevel gears. A bevel gear transmission is characterised by transferring rotation between two orthogonal crossing axes. It has high efficiency, and works equally well driven both ways.

There are some positive and negative sides to this solution:

- Pros
 - Mechanically simple.
 - Compact.
 - High efficiency.
- Cons
 - Either a brake must be applied, or the motor must work to maintain the position when the wing is subject to external forces.
 - The actuator may be subjected to axial and radial forces from the shaft.

It proved difficult finding or designing a suitable braking solution. The torque levels, both at mast and at drive shaft, are high. An alternative to a brake for fixing the position is retractable locking pins. This however, limits the angular precision. Accurate wing orientation with respect the wind is important in order to achieve as much thrust as possible. Figure 3.12 shows the lift over drag ratio $\frac{C_L}{C_D}$ at varying angle of attack, generated from *airfoiltools.com* [24]. Maintaining the ideal angle of attack boils down to a compromise between maximising thrust and minimise power consumption.

Based on this, and having tested that solution as is, the need for a new drive unit solution became clear.

3.2.2 Worm Gear Transmission

To eliminate the requirement of a brake in the bevel gear drive train design, a worm gear was introduced.

A worm and worm gear transmission is a reduction which is intended to drive one way. The worm is the driving element, and the worm gear driven. It is a widespread belief that worm gears are inherently self locking, but this is not always the case [26]. Depending on the rise angle and the coefficient of friction, a worm and worm gear configuration may be self locking or not. It must be kept in mind that contact between two materials generally exhibits different coefficients of friction depending on the condition. If a worm gear which is self locking by the static coefficient of friction is subject to vibrations or shocks, it might suddenly be the dynamic coefficient which governs. The latter generally having a lower value could allow the occurrence of slippage.

Worm Gear

The Norwegian supplier *Jens S. Transmisjoner AS* delivered the bevel gears, produced by German gear manufacturer *Maedler*. As they offered a wide range of products and great customer service, they were also the go-to supplier for worm and worm gear. A worm and worm gear with ratio $i = 40$ was decided upon and is further described in the next subsection.

Maedler state in their worm gear data sheet [27] that output torque is

$$T_{out} = T_{in} \cdot i \cdot \eta, \quad (3.1)$$

where the efficiency $\eta = 0.46$. To counter the design torque of 211 Nm , this calls for 11.467 Nm required motor torque, not accounting for other losses.

3.2.3 Elaboration of Drive Unit Design Criteria

The change of gear type brought a total reconfiguration of the drive system. The design was developed with respect to the following requirements:

- The design constraint regarding size entails fitting inside the NACA0018 wing profile.
- Keeping mass to a minimum is paramount. Any added mass contributes to elevating the vessel centre of gravity, thus negatively impact stability. It also increases the inertia of the wing.

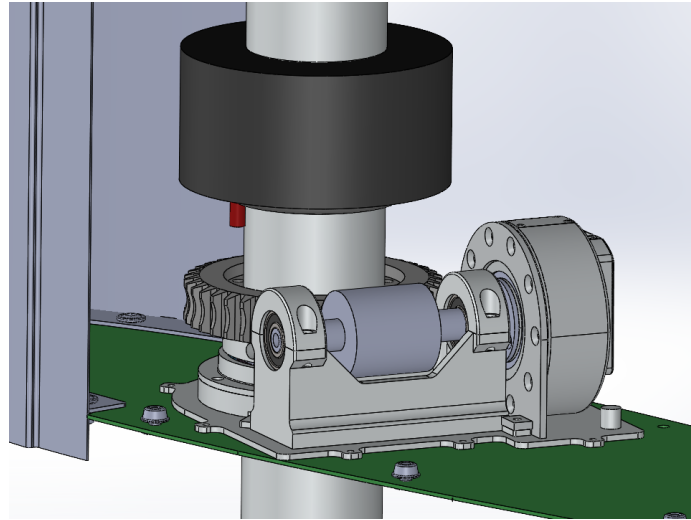


Figure 3.14: CAD model of drive unit.

- One aspect which provides added demands is that the worm transfers considerable axial loads. These must be absorbed by the supporting structures. The actuator is not designed to take axial loads of this scale.
- The axes of the worm and worm gear must be precisely positioned. Misalignment or deformations of the loaded structure can lead to excessive wear and failure, in addition to unwanted slack/backlash.
- The design must facilitate $n360^\circ$ rotation. This is an advantage for several sailing manoeuvres, e.g. jibing.
- Easy access and assembly/disassembly of the main components is of essence, in accordance with objectives 4 and 6, Table 1.1.
- A marine environment is extremely demanding in terms of corrosion. Any component must either be protected or have material of excellent resistance towards corrosion. A4 stainless steel and certain aluminium alloys are applicable. However, if even these are in electrical contact galvanic corrosion must be considered.
- Components should be possible to buy or manufacture in-house using available equipment and materials. Specifically, this means that parts for machining should be designed for 3-axis milling (either manual or CNC), turning and/or abrasive water jet cutting AWJC. Various metallic plates, bolts and tubes are available. This includes different aluminium alloys and steels, including AISI316 stainless. Acquisition of components should preferably be through Norwegian vendors, with short delivery time to stay within schedule.
- Design requirement load case described in Section 1.8.

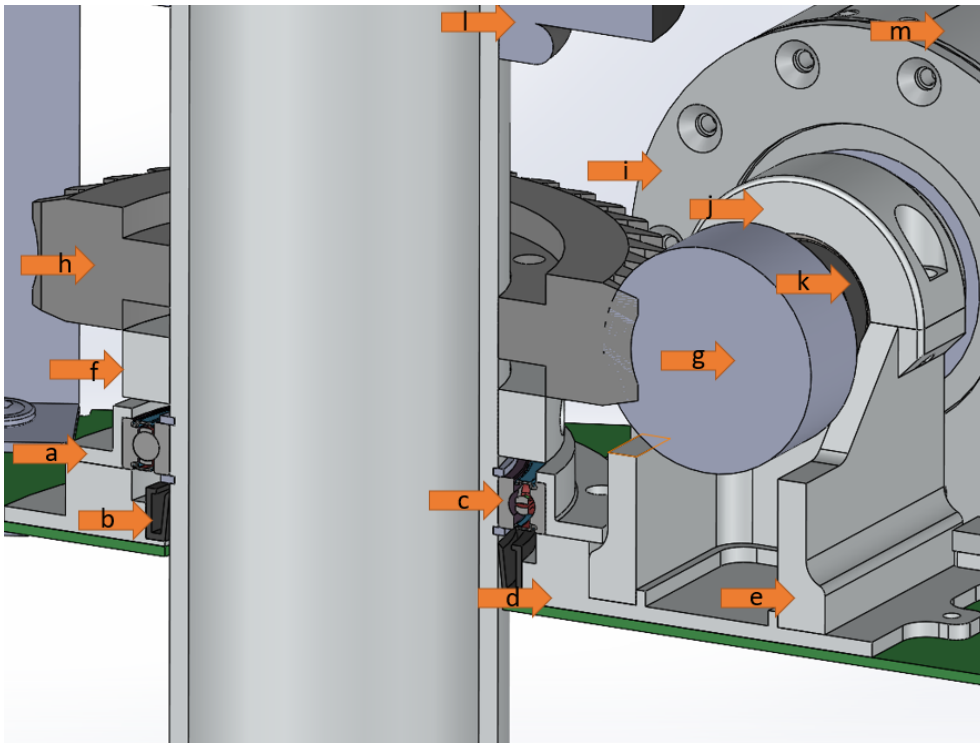


Figure 3.15: (a) Mast bearing cap. (b) Simmer ring. (c) Mast bearing. (d) Bottom plate. (e) Shaft bearing support structure, lower. (f) Gear ring. (g) Worm. (h) Worm gear. (i) Motor support bracket. (j) Shaft bearing support, upper. (k) Shaft bearing. (l) Slip Ring (m) Actuator.

3.2.4 Drive Unit Design

Figure 3.14 and Figure 3.15 display the design developed as a result of these requirements. Each component is in the following pages presented and their respective processes and features are discussed. Machine drawings for all components are available in Appendix B. It must be stated that the following analyses of stiffness and strength performed on the various components are not to be taken as proof of design adequacy. Their purposes are to give an indication that said component is in the ballpark of something which will not break immediately upon prototype loading.

Actuator

The **RMD-X8 Pro** in Figure 3.16 is a brushless direct current (BLDC) servo motor of a type frequently used in robotics, which comes at around \$500 a piece. It is very compact, and has a planetary gear built into it, such that it can deliver 35 Nm out at 80 rpm , with a maximum speed of 225 rpm . It has a built in closed loop controller communicating via CANbus protocol. Mechanical drawing available in Appendix B and full data sheet in Appendix D.

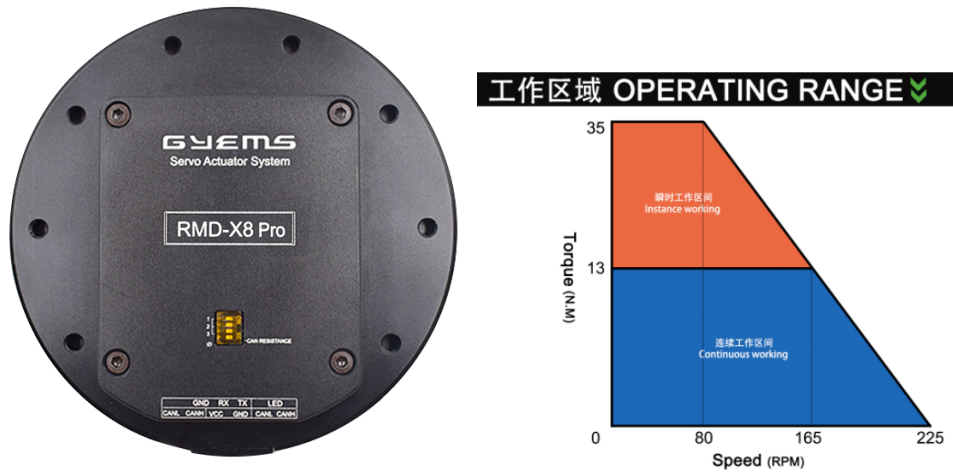


Figure 3.16: RMD-X8 Pro actuator and its operating range. Taken from manufacturer homepage [28].

Shaft Bearings

There were a few simple, but important, design criteria active in determining the bearing solution.

- External dimensions of bearing and bearing housing should be as small as possible, as to not interfere with the worm gear while leaving space for the actuator. Studying the design, a constraint was set to 50 mm .
- Inner dimension must be sufficient for the shaft to handle the driving torque.
- Each bearing must handle the axial load. The worm shaft will transmit up to 3517 N . If fitted properly this load will distribute evenly on both bearings, but to meet the requirement of $SF \geq 2$ the design should consider a load distribution situation where one bearing slides and the other absorbs the load.

A foot bearing, where a bearing is pre-installed in housing, was considered as a possible solution. They however have a few disadvantages to our application. The axial force will be transformed to a considerable moment at base. The size and shape of available models was difficult to make comply with the design constraints.

If instead the housing is designed and manufactured in-house, determining the bearing is easier. Choice fell on a 4201-BB-TVH double row deep groove ball bearing with the dimensions $12 \times 32 \times 14\text{ mm}$. Deep groove ball bearings are rated in terms of radial load capacities. In the data sheet, which is available in Appendix D, the basic static radial load rating $C_0 = 6100\text{ N}$. According to the Shaeffler ball

bearing design guide [29], double row deep groove ball bearings have an axial load carrying capacity $\leq 0.5C_0$. Exceeding this load level will lead to considerable reduction of service life. This equvalates 3050 N for the bearing in question. As $3050 N < 3517 N$ this is not in accordance with the pre-mentioned criteria, and corresponds to $SF = 1.73$. For this prototype application, this is accepted. These bearings are supplied by *Abra Kulelagersenteret AS* in Trondheim.

Shaft Bearing Support Structure

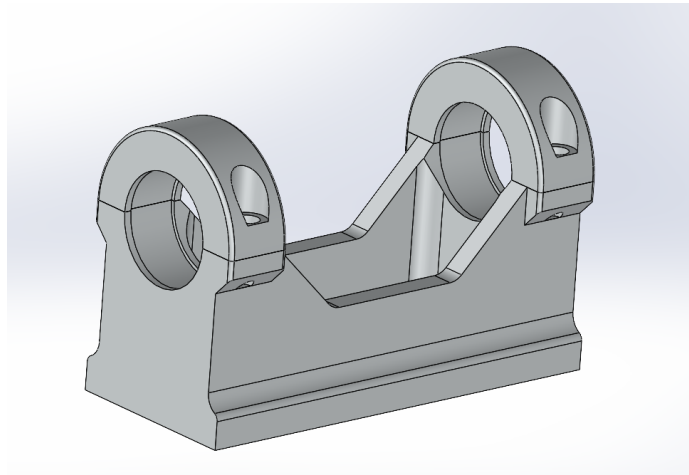


Figure 3.17: CAD model of the bearing support structure.

Figure 3.17 shows the shaft bearing support structure. It is comprised of one lower part and two upper parts. The purpose of this component is to hold the worm shaft with bearings in place, and transfer the axial forces from the shaft to the surrounding structure. When the bearings are inserted, the upper parts are secured with 2 M6 bolts each. The structure is fixed to the base plate through 8 countersunk M4 bolts, inserted from below.

A FEA was performed to verify that the structure can withstand the load, both with respect to deflection and stress.

The structure was encastered at base. The bolted connection was modelled as a rigid coupling, which might be the most questionable aspect of this analysis with respect to the realistic situation. A point load acts on a reference point located on the shaft axis. The point is in turn coupled to the hub face.

Table 3.4 lists the results of simulation performed with two sizes of tetrahedral mesh. The deflection is to a large extent converged. The stress keeps rising, however the peaks are in areas of infinitely sharp edges. This is a known attribute of mesh refinement. According to Abaqus documentation [30] this causes unrealistic predicted stress close to the corner, but does not affect the general response

of the model. The stress distribution is visualised in Figure 3.18.

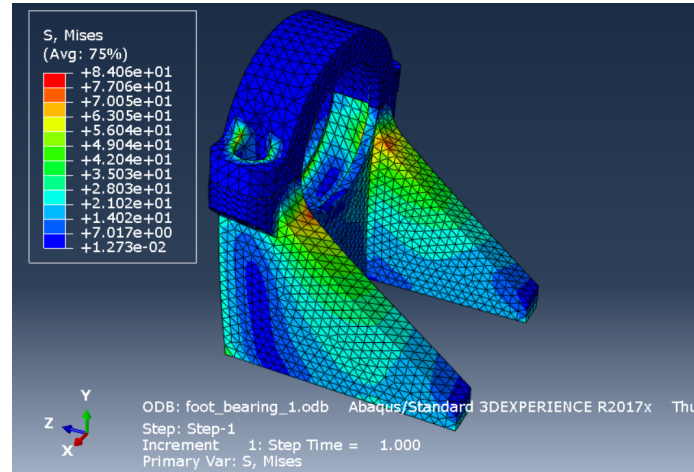


Figure 3.18: Visualisation of the stress distribution in the first design of the bearing support structure.

Table 3.4: Analysis results with mesh refinement for the bearing support.

Load Case	Mesh Size	Max Deflection	Max von Mises Stress
3500 N axial force	4 mm	6.525e-3	69.87
	2 mm	6.584e-3	84.06

The resulting deflection is very small, and does not pose a problem. According to supplier of aluminium products *alumenco.no* [31], the alloy EN AW-6082 T6 has yield strength around 250 MPa. Among the readily available alloys in both bulk, plate and extruded profiles, this seems the best choice for these applications. However, the material available for prototyping come from a box of miscellaneous unmarked pieces of aluminium. Hence, assuming 6082, the SF to yield is approximately 3. It could however be as low as 1.5 in the prototype.

The FEA was performed at an earlier design stage for this part, and some alterations of the structure have been performed thereafter. This was mainly done for machinability and manufacturing. Material was only added, not removed, so the stiffness and strength of the part may only have been enhanced by this. A quick analysis, without assessing mesh convergence, indicates this. Figure 3.19 visualises the stress distribution.

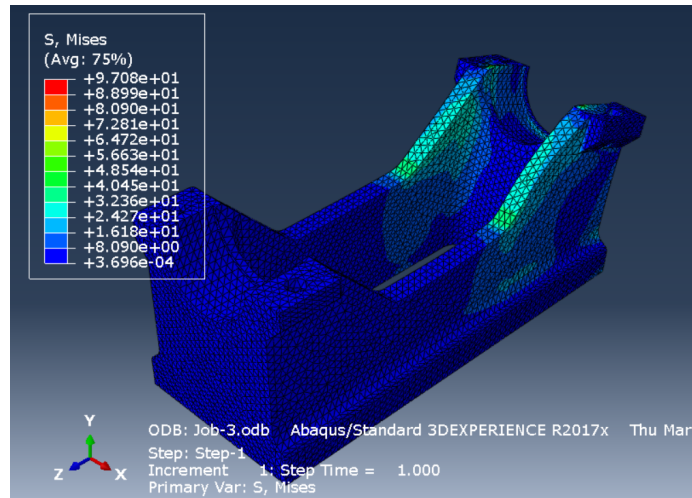


Figure 3.19: Results of a quick analysis of updated bearing support design.

Worm Shaft and Motor Connector Flange

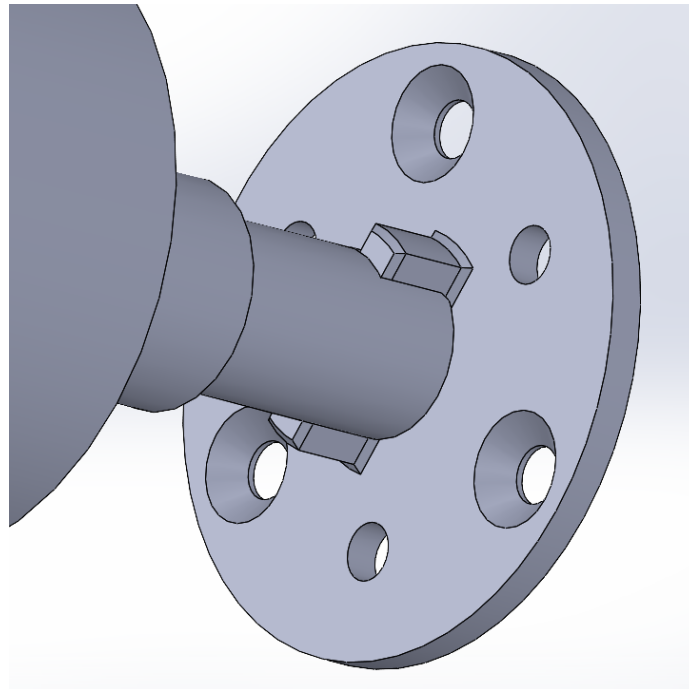


Figure 3.20: CAD model of the connection between the worm shaft and motor.

The actuator outputs the rotary motion through a connector face with three pins and three threaded holes. Figure 3.20 shows the first iteration connection, comprised of flange with connector tap and shaft with groove. The motor, with flange

attached, should be easily inserted and removed while the shaft is in place. This tap and groove connection allows the motor to be slid into place. The connection transfers torque only, and no axial force as this may damage the motor.

Table 3.5: Material properties for the worm shaft and motor connector flange

Part	Material	E [MPa]	ν	σ_y [MPa]
Worm Shaft	Steel C45	210000	0.3	310
Connector Flange	AISI 316	193000	0.3	205

The design torque of $11.5 Nm$, was used in the analysis. The two connecting parts were analysed separately, both as solids meshed with tetrahedral elements. Properties were given according to Table 3.5. Table 3.6 and Table 3.7 list the results of the analysis of the flange and shaft connectors respectively. Certain nodes have been neglected, as the stress peaks are a result of infinitely small radii and unrealistic boundary conditions.

Table 3.6: FEA results with refining mesh for motor connector flange.

Load Case	Mesh Size [mm]	von Mises Stress [MPa]	Deflection [mm]
11.5 Nm	2.3	122.1	8.517e-3
	1	140.2	8.791e-3
	1 and 0.5 local	152	8.801e-3

Table 3.7: FEA results with refining mesh for worm shaft connection.

Load Case	Mesh Size [mm]	von Mises Stress [MPa]	Deflection [mm]
11.5 Nm	1	162.3	1.433e-2
	1 and 0.5 local	197.44	1.437e-2

Figure 3.21 shows a visualisation of the von Mises stress in the worm shaft connection slot. Stresses above $200 MPa$ are greyed out. Stress concentrations at the top may be neglected, but those at the bottom of the slot are a real threat to the integrity. The situation is similar in the counterpart as well.

From the analysis of this connection, it comes out as not sufficiently strong, with $SF_{y,worm} \geq 1.57$ and $SF_{y,flange} \geq 1.34$. Although static stresses are within the elastic regime of the material, these components may be prone to fatigue. A redesigned connection is described and analysed below. The reason that the preliminary design is included here at all, is that the author got ahead of himself and

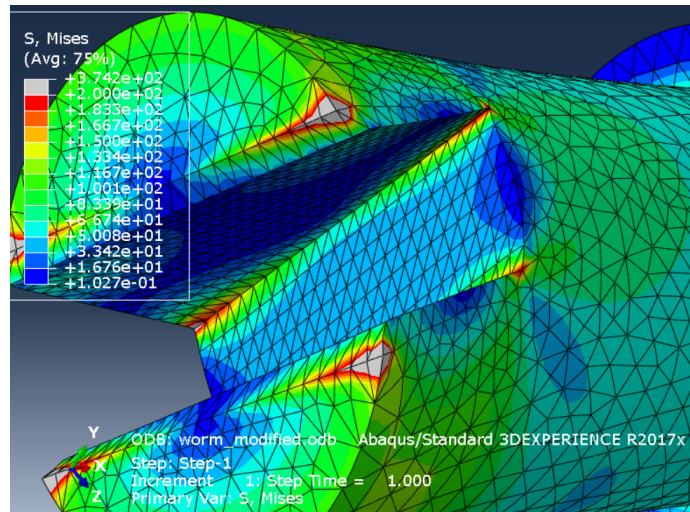


Figure 3.21: Close view of worm shaft connection slot. Stress concentrations at the top may be neglected, but those at the bottom of the slot are a real threat to the integrity.

commenced manufacturing before completion of the analyses.

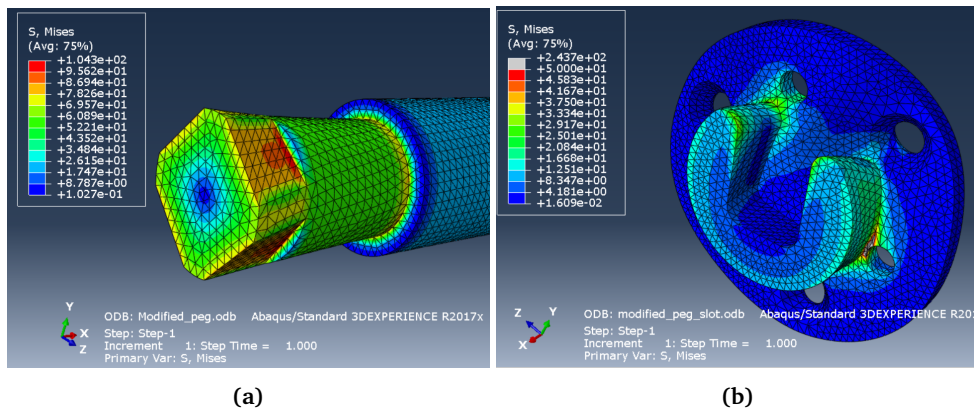


Figure 3.22: Redesigned connection analysed, providing a more moderate stress situation. Unrealistic stress concentrations greyed out.

By inverting the roles of the two parts, both a larger area and polar moment of inertia can be achieved. Figure 3.22 show the stresses in the components under the same torsional load. By comparing to the yield strengths σ_y given in Table 3.5, $SF_{y,worm} \geq 2.98$ and $SF_{y,flange} \geq 4.1$.

Worm Shaft Bearing Fit

This design requires that the shaft must sit tight in the bearings. A press fit could assure this.

Symbol explanations for the following equations are given in Table 3.8. According to Härkegård [32] the mean interference of shaft and hub is given as

$$\delta_m = \frac{1}{2}[(es + ei) - (ES + EI)]. \quad (3.2)$$

The probable maximum deviation from the mean is

$$\Delta\delta = \frac{1}{2}\sqrt{(es - ei)^2 + (ES - EI)^2}, \quad (3.3)$$

making the probable interference

$$\frac{\bar{\delta}_{max}}{\bar{\delta}_{min}} = \delta_m \pm \Delta\delta. \quad (3.4)$$

The fit pressure p is related to the radial displacement through

$$\frac{\delta}{2} = (\alpha_{ni} + \alpha_{ay}) \cdot p, \quad (3.5)$$

where α_{ni} and α_{ay} are the influence coefficients of the hub and shaft respectively, given by

$$\alpha_{ni} = \frac{1}{E_n} \frac{r_{ni}^2}{r_{ny}^2 - r_{ni}^2} r_{ni} \left[1 - \nu + (1 + \nu) \frac{r_{ny}^2}{r_{ni}^2} \right] \quad (3.6)$$

and

$$\alpha_{ay} = \frac{1}{E_a} \frac{r_{ay}^2}{r_{ay}^2 - r_{ai}^2} r_{ay} \left[1 - \nu + (1 + \nu) \frac{r_{ay}^2}{r_{ai}^2} \right]. \quad (3.7)$$

The shear force F transmittable by the fit will then be

$$F = \mu \cdot p \cdot \pi \cdot D \cdot b, \quad (3.8)$$

where $D = 2r$ is the nominal diameter and b the width.

The stress experienced by the hub has two major components, radial compression stress $\sigma_{r,ni}$ and tangential tension $\sigma_{\phi,ni}$, given by

$$\sigma_{r,ni} = -p \quad (3.9)$$

and

$$\sigma_{\phi,ni} = p \frac{r_{ny}^2 + r_{ni}^2}{r_{ny}^2 - r_{ni}^2}. \quad (3.10)$$

The resultant stress can be calculated according to von Mises as

$$\sigma_{mises} = \sqrt{\frac{(\sigma_1 - \sigma_2)^2 + (\sigma_2 - \sigma_3)^2 + (\sigma_3 - \sigma_1)^2}{2}}, \quad (3.11)$$

in the static situation, not loaded with shear force.

The bearing is by the manufacturer given with tolerance ${}_{+4}^{+11} \mu m$. This does not directly comply with any ISO standard tolerances. Table 3.8 shows the calculated values for the press fit between the worm shaft and the bearings, if the worm is machined according to n6 tolerance.

Table 3.8: Calculated values for press fit between worm shaft and bearings, with shaft machined to n6 tolerance.

Description	Symbol	Value
Poissons ratio	ν	0.3
Hub internal radius	r_{ni}	6 mm
Hub external radius	r_{ny}	9 mm
Shaft internal radius	r_{ai}	0 mm
Shaft external radius	r_{ay}	6 mm
Shaft lower tolerance	ei	12 μm
Shaft upper tolerance	es	23 μm
Hub lower tolerance	EI	4 μm
Hub upper tolerance	ES	11 μm
Mean interference	δ_m	16 μm
Maximum probable deviation	$\Delta\delta$	6.5 μm
Hub influence coeff.	α_{ni}	8.7×10^{-5}
Shaft influence coeff.	α_{ay}	2.1×10^{-5}
Pressure	p	$\in (46.3 \pm 30.1) MPa$
Hub radial stress	$\sigma_{r,ni}$	$\in (-46.3 \pm 24.3) MPa$
Hub tangential stress	$\sigma_{\phi,ni}$	$\in (120 \pm 78) MPa$
von Mises stress	σ_{mises}	$\in [52 - 244] MPa$
Force limit* given $\mu = 0.2$	F	$\in (4887 \pm 3177) N$

From the table one can clearly see that, especially in the upper part of the tolerance area, stresses are very high. It is worth mentioning that only the inner ring cross section of the bearing has been taken into the calculation. Nonetheless, shaft diameter in the lower end of the tolerance area should be strived for.

Motor Support Bracket

The motor should mainly experience torsional forces, and this is seen to by the above mentioned connection. The structure securing the motor may then be de-

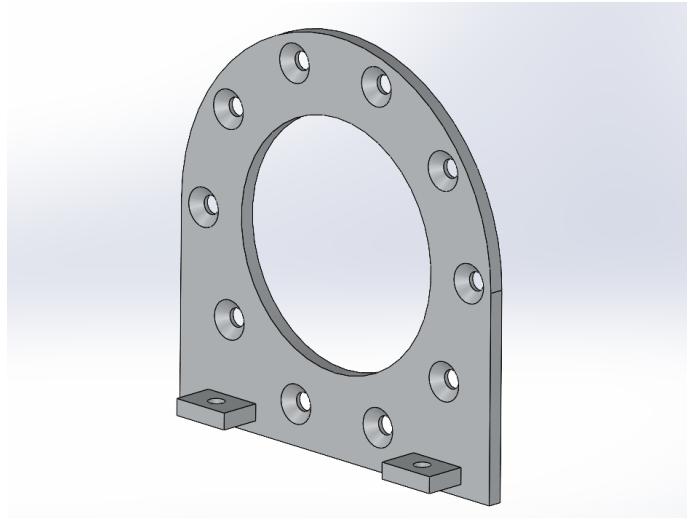


Figure 3.23: CAD model of motor support bracket.

signed with only this in mind. The motor support bracket, Figure 3.23, is merely a plate with screw holes correctly located. The motor should be fixed to this before insertion. The bracket fastens with two M4 bolts accessible straight down from top. The part can be cut by AWJC from a thin aluminium plate. The protruding parts can be cut separately, inserted into slots and welded. The part has not been analysed for strength or stiffness.

Sealing Rings



Figure 3.24: Sealing ring (black) sitting tight below the bearing in the bottom plate.

The compartment must be kept tight, not letting fluids in or out. This is no issue for any static application, but here there is relative rotary motion with respect to the mast. Sealing rings, also known as simmer rings, located at mast entry and exit see to this. One sits in the bottom plate as shown in Figure 3.24, and the other in the box top.

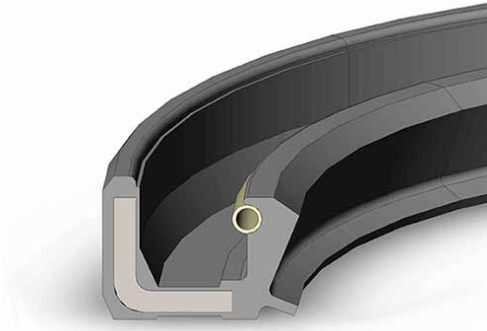


Figure 3.25: Section view of a BASL sealing ring.

Simmer rings of the type BASL 70-80-10 are used. They are made from rubber and steel, and have a spring which squeezes the rubber lip around the shaft, see Figure 3.25.

Mast Bearing

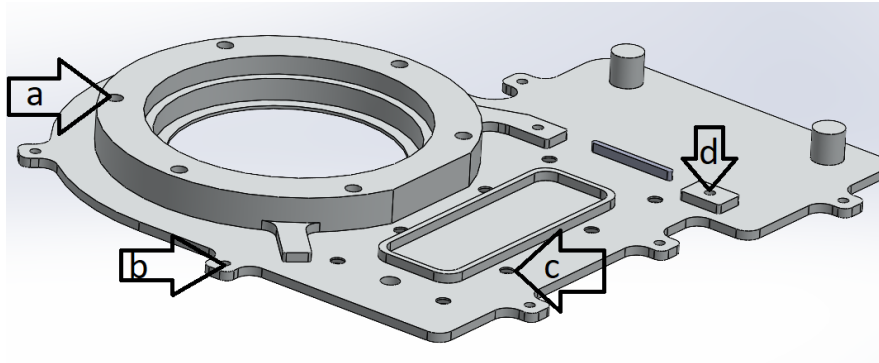
The wing is supported by the mast in three points. A ball bearing at the bottom transfers both radial and axial forces. Two sliding rotating bearings located at the middle and top of the wing transfer only radial forces. The axial load is essentially only the weight of the sail, along with inertial loads related to the acceleration of its mass as the vessel moves up and down. The total mass of the wing resides somewhere between 20 and 30 kg, corresponding to 300 N. In any case, the axial load is in magnitude 1 kN.

The bearing is a single row deep groove ball bearing of the type 61814-2RZ-Y with dimensions 70x90x10 mm. Deep groove ball bearings are rated in terms of radial load capacities. In the data sheet, which is available in Appendix D, the basic static radial load rating is given as $C_0 = 12400 N$. According to the Shaeffler ball bearing design guide [29], single row deep groove light series ball bearings have an axial load carrying capacity $F_a \leq 0.25C_0$. This means that the axial loads it will experience will be well within the tolerable area.

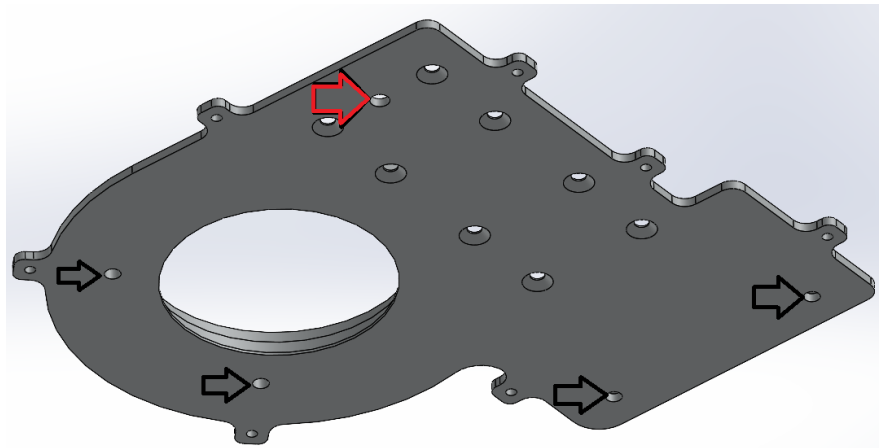
Bottom Plate

The bottom plate serves two main purposes. It places the different components at precisely the right location, and it closes the bottom of the compartment. Figure 3.26 shows the plate from the over- and underside. The purpose of all holes are explained in the captions. The part is designed for manufacturing. The external shape is to be cut by AWJC from an aluminium plate before features are

milled on a 3-axis CNC machine. The plate is secured to the wing bottom section with five bolts in addition to gluing with epoxy.



(a) (a) 6 threaded m6 holes for fastening the bearing cap. (b) 7 threaded M4 holes for fastening the box. (c) 8 $\text{\O}4$ holes for fixing the shaft bearing support. Countersunk on the underside. (d) Two threaded M4 holes for motor support bracket.



(b) Holes for fixing the plate to the GFRP wing bottom plate. Black: threaded M6. Red: $\text{\O}6$ open to threaded M6 hole in shaft bearing support.

Figure 3.26: Box bottom plate explanation.

Realistic FEA of this component is somewhat difficult. Considerable additional stiffness will be brought by the GFRP plate underneath and the enclosing box structure. An analysis without accounting for any of this was performed. A normal force is applied in a reference point on the worm axis. The point is coupled to the footprint of the worm shaft support. As boundary condition the structure is pinned where the mast bearing will be fastened. Figure 3.27 show the deflectional response to this, with maximum value 0.25 mm .

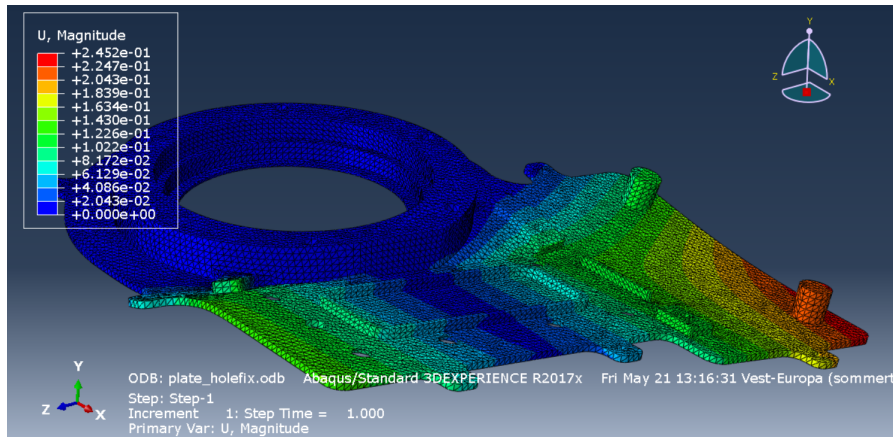


Figure 3.27: Deflection of bottom plate loaded with 3500N through the shaft axis.

Worm Gear and Connector Ring

The selected worm gear is of module 3 and has 40 teeth. This leads to a gear ratio $i = 1 : 40$ to the worm shaft. It is rated to 189 Nm.

The worm gear is made of GG25 cast iron. The decisive strength criterion is, according to the manufacturer [27], for small modules the pitting resistance of the worm gear flanks and for larger modules usually the tooth-root strength of the worm gear. The tooth root safety factor is minimum $SF=2$. This means that a gear rated to 189 Nm with a safety factor of 2, still has a safety factor of 1.79 for the design torque of 211 Nm.

The centre of this gear needs to be milled out to the diameter of the mast. It will be bolted to an aluminium ring, which in turn is secured to the mast. The latter may for permanent fixture be done by welding. However, for prototyping, where disassembly is wanted, M8 bolts serve the purpose.

Slip Ring

$n \cdot 360^\circ$ rotation of the wing was set as a criterion, as of the design criteria in Section 3.2.3. A slip ring provides connection of wiring between parts in relative rotary motion, and will allow power and signal to go between the components within the wing and the central electric system.

Wires from the hull go through the mast internally, come out by the slip ring and connect to the stator.

The slip ring was bought from the Chinese company *CENO Electronics*, and features four 15A power circuits and a CANbus line. This facilitates connection of

the actuator and the solar panels. Mechanical drawing available in Appendix B.

Oil Submersion

Even though the compartment is theoretically completely sealed, there is need for redundancy. Ingress of water is still a possibility, and condensation is another aspect of concern.

Electronic circuits are not affected by submersion in non-conductive liquids. This is something capitalised on in liquid cooling of high power computers and servers [33]. Neither may corrosion occur in a non-conductive medium. Thereby, filling the entire compartment with mineral oil may protect actuator, electronics, gears and all else confined within the box described in the next paragraph. This means that materials can be used in these components irrespective of their corrosive properties. The oil also ensures abundant lubrication of the gears.

Box

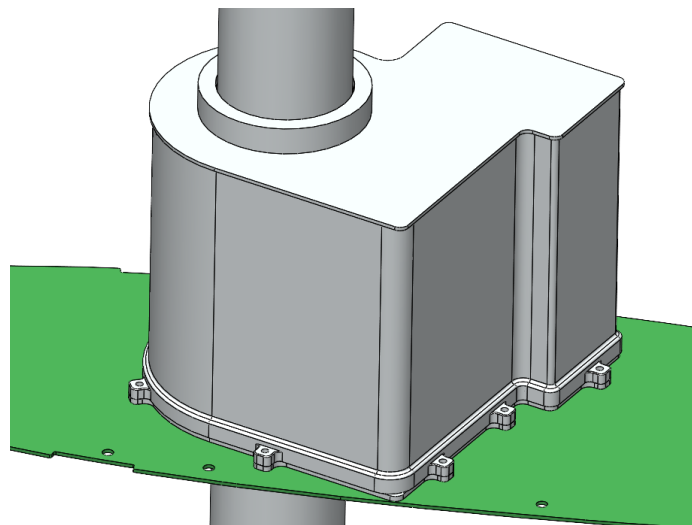


Figure 3.28: The sealed compartment envelopes the entire actuation mechanism.

The purpose of the box is to keep the drive mechanism shielded from the environment. First iteration may be 3D-printed. In the long run it might be more sustainable to mould it from GFRP. Figure 3.28 shows a 3D model of the containment. It is bolted to the bottom plate and has a o-ring groove along the connections.

Chapter 4

Manufacturing

This chapter tries to shed light on the manufacturing and crafting of the prototype. It is organised such that it goes through the wing first, then the drive unit and their assembly together.

4.1 Making the GFRP Wing

Vacuum assisted resin transfer moulding VARTM, as described in Section 2.2, was decided to be the method of production for the components forming the wing structure. As argued for by [12] and [14] in Section 2.2.2, it is advantageous over hand layup and RTM. The wing components are as follows:

- Side panels skin
- Leading edge skin
- Trailing edge skin
- Structural reinforcement:
 - Leading edge flanges
 - Trailing edge flanges
 - Side panel flanges
 - Profile sections for bottom, middle and top

The first may be moulded on a flat surface and bent into shape. The curvature is so small that strain will be negligible. The leading and trailing edge skins need to be produced to near net shape. The mould is discussed in Section 4.1.2. The structural reinforcement parts are also planar, and can be moulded on a flat surface and cut to shape.

All GFRP parts are made with EPICOTE™ Resin MGS™ RIMH135 together with EPICURE™ Curing Agent MGS™ RIMR137 and/or RIMR134. This is a DNVGL approved resin system, specially designed for infusion processes. It is suitable for wind turbine blades, boat and ship building, sports equipment etc. The resin has a long gelation time, which allows for a complete relaxation process in post filling,

as mentioned in Section 2.2.2. Figure 4.1 shows the temperature development of the resin in the pot. Full data sheet is available online [25]. According to [34] epoxy resin has the best resistance towards water absorption of normal thermoset resins, so it should be a good choice for this marine application.

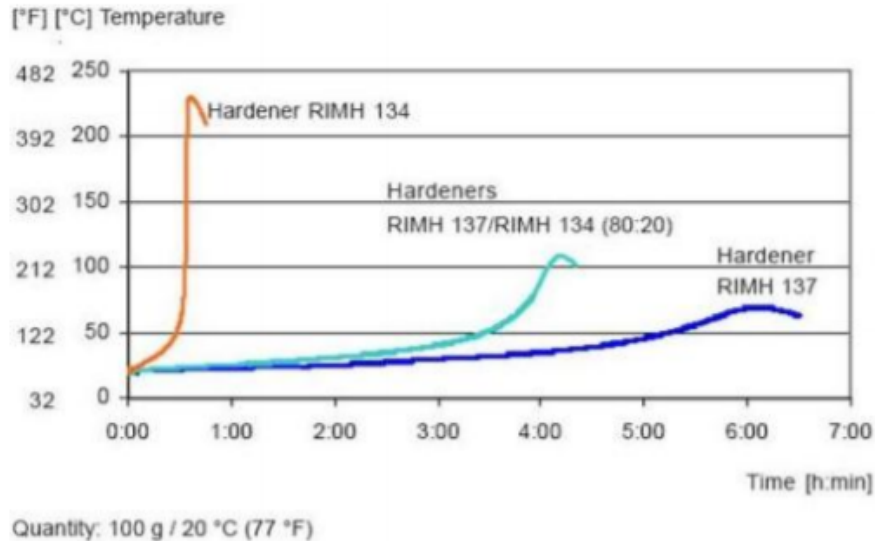


Figure 4.1: Temperature development in the pot of the EPI-COTE™/EPICURE™ resin system [25].

4.1.1 Test Infusions

The VARTM process is, as discussed in Section 2.2.2, highly dependant on worker skill. Therefore, before diving straight into producing large scale components, the author performed some smaller test infusion. Some lessons were learnt from these and the test mould infusions in Section 4.1.2, adding to the list of important process aspects in Section 2.2.2:

- Do not be afraid to use extra vacuum bag. Creation of folds allows the bag to better compact around shapes.
- Have an approximately 5 cm spacing without flow mesh before the vent, to ensure proper filling before resin starts to bleed out.
- When calculating resin amount, account for losses in buckets, tubing and flow mesh etc.
- Mix enough resin. If the pot is about to run out, there is chance of air getting in.
- Monitor for some time into the post-filling stage. Leakages may occur suddenly.

4.1.2 Mould Type

There was one major lesson regarding mould learnt from Dyrseth's [5] wing manufacturing. Her mould was made from solid medium-density fiberboard (MDF) plates, laminated together and milled. This resulted in a very massive construction, which in turn made it inherently difficult to handle and move around the lab. It has been explicitly expressed by those involved, including lab personnel and HSE coordinator, that future moulds for large scale components work around this issue.

Firstly, there are two possibilities for mould geometry - positive and negative. A **positive mould shape** has the following advantages and disadvantages:

- Pros:
 - Better dimensional accuracy and surface finish on the internal surface. This is an advantage for assembly with internal structure parts.
 - Good access to the part surface during vacuum process.
- Cons:
 - Laminate thickness must be accounted for to achieve accurate external dimensions.
 - Rough external surface.

A **negative mould shape** in turn feature the following:

- Pros:
 - Better dimensional accuracy and surface finish on the external surface. This is an advantage to the aerodynamic properties of the wing and for post-processing time.
- Cons:
 - Laminate thickness must be accounted for in regards to internal dimensions.
 - Poor access during process.

Weighing the various features against each other, it was elected to proceed with a positive mould. The difficult access of negative mould and the fact that skins are assembled with an internal structure were important tipping points. An investigation was made into two possible ways of constructing such a mould.

Foam Mould

This type of mould features a PVC foam, machined to shape using a CNC mill. Subsequently, the surface must be sealed using a sealant/coating.

A test mould was made. For simplicity a shape resembling the leading edge was manually cut from leftover PVC foam. Two layers of epoxy was used as coat-

ing. Figure 4.2 shows the mould prepared with fibre ready for infusion.

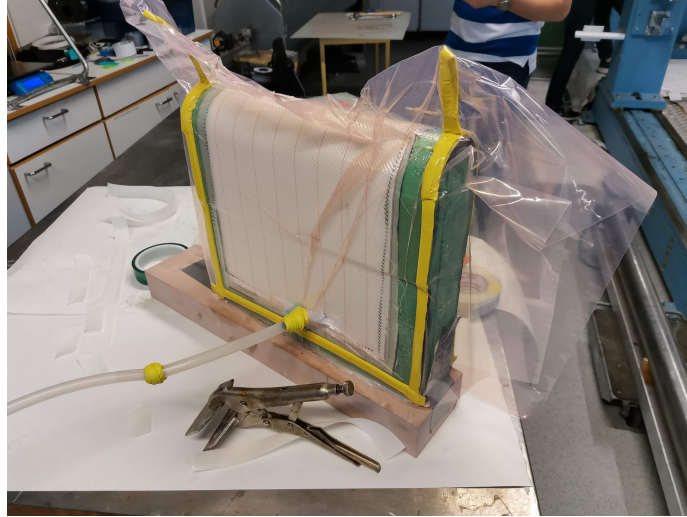


Figure 4.2: VARTM on foam test mould.

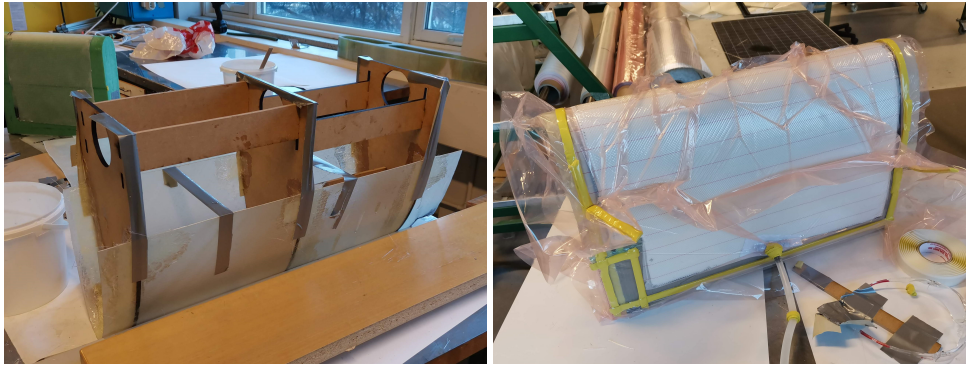
- Pros:
 - Few components.
 - Lightweight.
 - Allows 3-dimensional geometries.
- Cons:
 - Requires CNC machining.
 - Surface finish quality is limited.
 - Multiple layers of coating required to achieve tightness.

GFRP Thin Skin Mould

This type of mould is made possible by the wing profile being a 2D extrusion, i.e. having the same cross section over its entire length. Laser cut 6 mm MDF plates are assembled to give the shape. Thin glass fibre plates are wrapped around and glued in place to make the surface. Plates must be thin enough so that they deform in the elastic regime at this curvature.

By manufacturing and infusing on a test mould, as seen in Figure 4.3, the following list of advantages and disadvantages was made.

- Pros:
 - Easy and quick to make.
 - Lightweight



(a) Assembling the mould requires the skins to be held in place while gluing. Duct tape provides good assistance. (b) Ready to start the infusion. Notice the lower left corner where a major leakage in the skin was avoided by excluding this area.

Figure 4.3: GFRP thin skin test mould.

- Good surface finish
- Less chance of leakage through the face.
- Cons:
 - Many components to be assembled
 - Plates must be joined at low radius curves

Choice



Figure 4.4: The parts made on the two test moulds.

Both infusions experienced some leakages through the mould face. Still, both parts shown in Figure 4.4 came out decent, with a certain degree of porosity. In-

fusing over the geometry against gravity was no issue in either case.

There were no clear decisive aspects for choosing one over the other. Out of novelty, the thin skin mould was appealing to carry forward.

4.1.3 Mould Design and Manufacturing

The decision had been made to make a GFRP thin skin mould.

For the final component to achieve the intended profile, the mould section geometry had to be offset. Accounting for 1 mm component thickness and 1 mm mould skin thickness yields a 2 mm offset, as visualised in Figure 4.5. 2 mm extra was added in the connective region, with the intention of some extra plies of reinforcement to be added here in post-processing. Also, 10 cm extra length is added to leave room for resin gates/vents and cut-offs. Spring in, posed as a problem by [12] in Section 2.2.2, does not need to be accounted for. The part will be forced back into shape by the insertion of the internal structure.

Each mould consists of 12 sections spaced with 25 cm , summing up to 275 cm . This leaves 35 cm excess with regard to the height of the wing. The connecting beam elements come in 6 different variants. All the parts which make up the two mould structures were modelled in *SolidWorks* and exported as .PDF drawings. These drawings were imported to *Inkscape*, where they were converted to specifically formatted vector graphics which are understandable for the laser cutter. Parts are cut from 6 mm MDF plates. Preliminary assembly was done with hot melt glue gun.

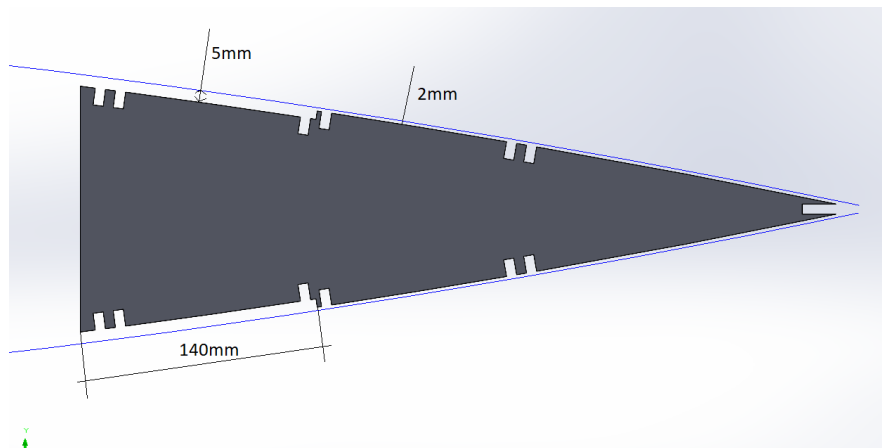


Figure 4.5: The mould rib is offset with respect to the wing profile, accounting for mould and part thickness.

To create the mould skin, two GFRP plates were produced by VARTM. Attain-

ing a large enough moulding surface to make the plates turned out to be difficult. To solve this, two shorter steel plates were taped together. This worked in regards to the process, but it will emerge later in Section 4.1.4 that the joint brought along some complications. Figure 4.6 show the two infusion processes. The joint can vaguely be seen as a green line across the table.

A $600 \frac{g}{m^2}$ biaxial fabric available in the lab was used as reinforcement. Some details on the process are given in Table 4.1. AWJC was used to cut the plates into pieces of the right width. These were then glued with epoxy, and in some places reinforced with CSM, to the internal mould structure. A few steps of this assembly process are shown in Figure 4.7.

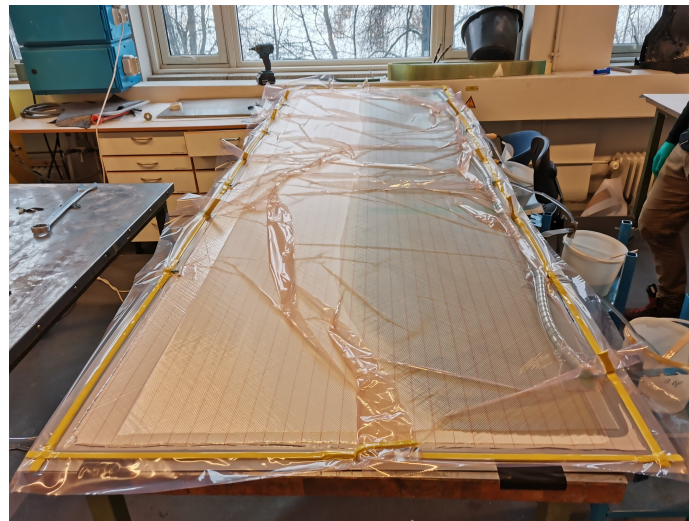
As mentioned in Section 4.1.2, a gap between the plates exists on each side of each mould, which had to be sealed tight. This was done with an adhesive tape.

The vacuum infusions of the mould plates had given quite a good result, but in the demoulding some delamination had occurred a couple of places. These spots were attempted saturated and sealed with epoxy after assembly. Then, the entire moulds were coated with a spray paint which, hopefully, would penetrate and close any micro-cracks or holes.

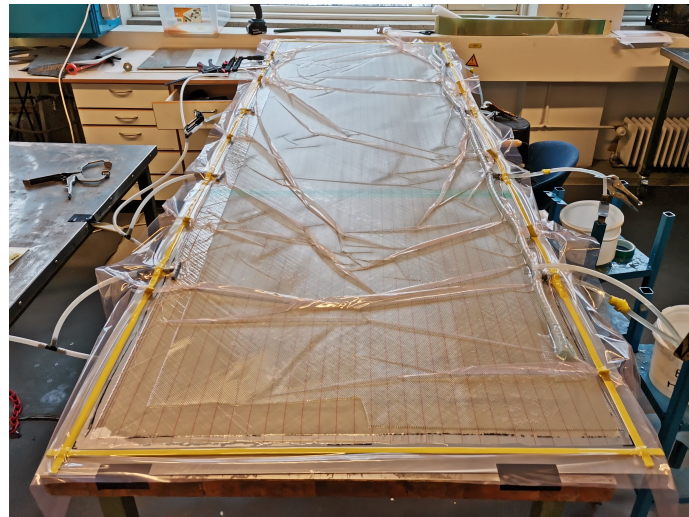
4.1.4 VARTM of Wing Components

Table 4.1: Data on the 8 different VARTM processes to make the moulds and components.

Part	Mould skin 1	Mould skin 2	Side panel	Side panel	Lead. Edge	Trail. Edge	Plate a	Plate b
Size [cm]	90 x 290	90 x 290	85 x 290	85 x 290	75 x 260	75 x 260	90 x 150	90 x 150
Layup thickness [mm]	0.6	0.6	0.9	0.9	0.9	0.9	2.1	2.1
Resin mass [kg]	4	5	4	3.5	3	3	2.5	3
Curing agent RIMR	137	137	137	137	137	137 134 (60/40)	137	137
#gates	4	4	3	2	2	1	1	1
#vents	4	4	4	3	3	3	1	1



(a)



(b)

Figure 4.6: Infusion processes of the two laminates for mould making.

The intention was to use $[0/90]$ woven roving in combination with $[\pm 45]$ bi-axial fabric. Unfortunately, the supplier of the bi-axial fibre misplaced the order, and it was not shipped in time. To tackle this and still stay somewhat within schedule, $[0/90]$ weave oriented at an angle was used as a substitute.

All VARTM processes were performed according to the description in Section 2.2.1. Table 4.1 summarise some detail on the processes, in chronological order. Some clear trends of learning may be recognised. A large number of resin gates was found to be excessive. For components of this scale, the resin will be sufficiently supplied through one gate and distributed through the spiral tube. Waste

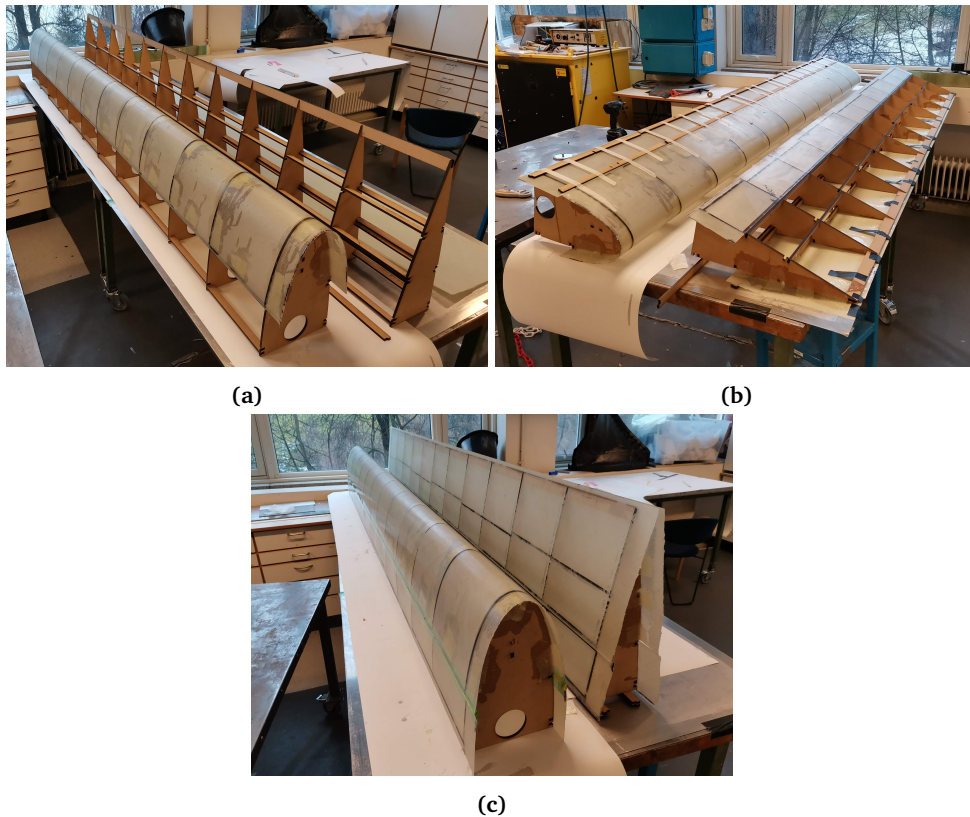


Figure 4.7: Mould assembly stages.

of consumables and resin is reduced, and so is process complexity. With gaining experience, tuning the amount of mixed resin became easier. Each component required between 3 and 8 hours for one person to prepare and perform.

The skin layup was 6 plies of $200 \frac{g}{m^2}$ weave, data sheet available in the Appendix D. As the diagonal plies would consist of discontinuous fabrics, it was avoided to have two of them adjacent. Thereby, the layup was: $[(0/90)/(\pm 45)/(0/90)/(0/90) - (\pm 45)/(0/90)]$. Still, by the lay-up being quasi-isotropic and anti-symmetric desired laminate behaviour is achieved.

It must be noted that none of the laminate parts in this section were post cured at elevated temperature, as they should according to [25], for the quite practical reason that no large enough curing oven is available at NTNU. This means that the epoxy is not 100% cured, and slightly less stiff than the ideal properties imply.

Side Panels

In Figure 4.8 the joint in an oriented fabric ply can be seen. A rule of thumb is that overlap should be at least ten times the ply thickness, however in such a thin fabric it easily becomes more than that. Around 1 cm overlap was targeted to be certain.

Both processes went quite painlessly with highly satisfactory result. There was a slight inlet of air for the first panel, as a pot ran out of resin and the tube was exposed unnoticed for a couple of seconds. This had little to no impact on the component, as the intruded air resided in the flow mesh while the fibre stack below remained saturated.



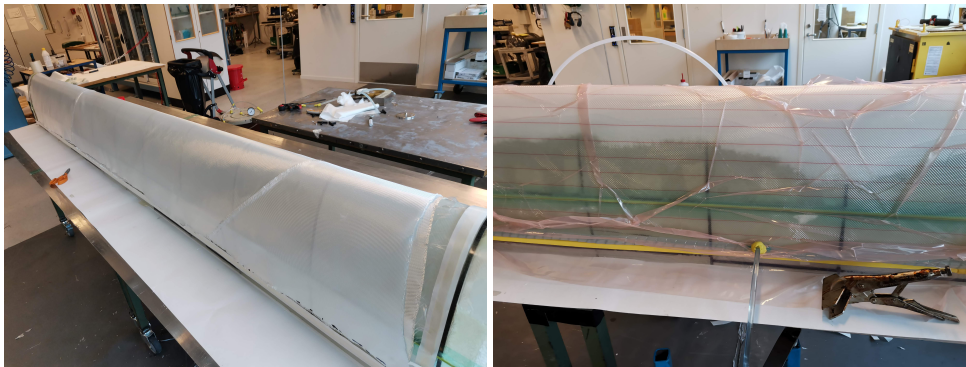
Figure 4.8: The overlapping joint in a ply oriented at 45° .

The panels were water cut along with the internal structure. Delamination occurred frequently as the jet penetrated the laminate. This comes to show especially at the holes, and more extensively in the 2 mm thick structural reinforcement laminate than the thinner side panels. The operator was in training and quite inexperienced with the machine, so it was difficult to know how the process parameters, as discussed in Section 2.3, were tuned.

The number of bolt holes along the panel edges were reduced from the FEA model, from 10 to 5. This is simply to make the assembly easier. If it was to become clear in assembly or physical testing that the number is too low, drilling more holes is a quick fix.

Leading and Trailing Edges

Aligning the diagonal plies on the mould, as seen in Figure 4.9a, proved quite difficult. Making sure they overlapped continuously, maintained their position and were even with no folds was a time consuming challenge, and an adhesive spray was used as help. This was an adhesive intended for such a purpose, and stated to dissolve in the epoxy resin. As the vacuum was applied, one could see some unevenness. This turned out in the final part as protruding waves in the laminate. How these were handled is discussed in Section 4.1.5.



(a) Fabrics being stacked onto the leading edge mould. (b) The resin advances over the leading edge profile.

Figure 4.9: Leading edge VARTM process.

Both leading and trailing edge VARTM processes suffered from a non-intact vacuum. There were in both cases leakages of two different causes, both a result of improperly sealed mould. Some imperfections of the mould skin itself, in form of cracks, dryspots or delaminations, caused air to ingress. The other was leakage under the tape joining the gap between the upper and lower parts of the mould. Remember from Section 4.1.3 that there was an indentation of the mould plate where joining of the steel mould plates had been. This caused a small channel for air to get through under the crossing tape in the leading and trailing edge moulds. An attempt at additional sealing here had apparently been unsuccessful. In Figure 4.10 you can see bubbles emerging from the bottom of the green tape.

For the trailing edge some accelerator was added due to the awareness of the leak, so the resin would gel faster and less resin bleed out by gravity. Comparing the resulting laminate to the leading edge, it is slightly less porous even though they experienced the same approximate level of leakage.

The components were manually cut to net shape with a Dremel cutter. There were clear signs of local heating damage in the outer millimetre along the cut edge, as discussed in Section 2.3. This should not have a considerable negative

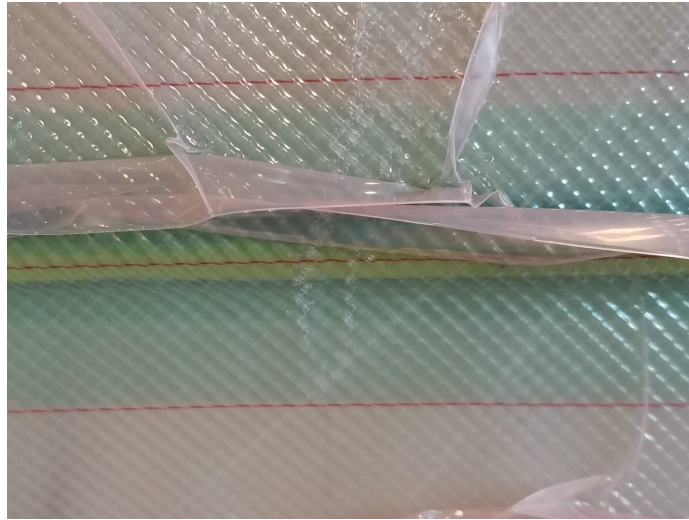
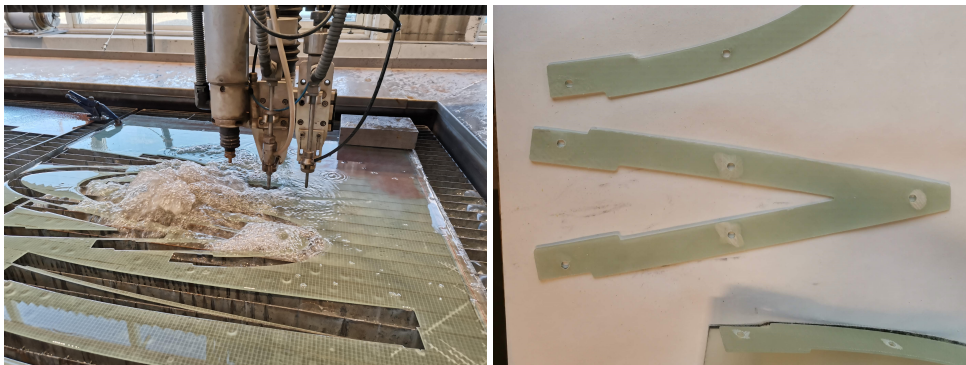


Figure 4.10: Bubbles appearing under the tape, due to the indent in the skin.

effect on the structure, as these areas close to the edge do not play an integral part in load carrying.

Internal Structure

For this laminate, a rather heavy biaxial fabric available in the lab was used in addition to the (0/90) weave. It is $800 \frac{g}{m^2}$ and 0.6 mm thick. The layup for these plates was $[(0/90)/\pm 45/-(\pm 45)/\pm 45/(0/90)]$ amounting to 2.1 mm . See Table 4.1 for more details about the process. Further there was nothing in particular to note from the infusions. The resulting laminates looked immaculate by visual inspection. Figure 4.11a shows the internal structure flanges being cut. The delamination occurring at initial penetration can be seen in Figure 4.11b around the holes.



(a) AWJC in progress.

(b) Delamination can be seen around holes.

Figure 4.11: Abrasive Water Jet Cutting AWJC

4.1.5 Assembly

To hold the flanges in their precise respective positions while glued, slotted bars lasercut from 6 mm MDF was used. It is highly important that the distances between the ribs are precise in the four wing parts, as to not strain the structure when assembled with the section plates. The flanges were correctly positioned, as seen in Figure 4.12. Some additional securement with tape and clamps was added. Epoxy and chopped strand mat CSM reinforcement was used for fastening. The epoxy was prepared with the rapid hardener RIMH134. The supports limited the access, so additional gluing was done after the epoxy had hardened and the supports were removed.

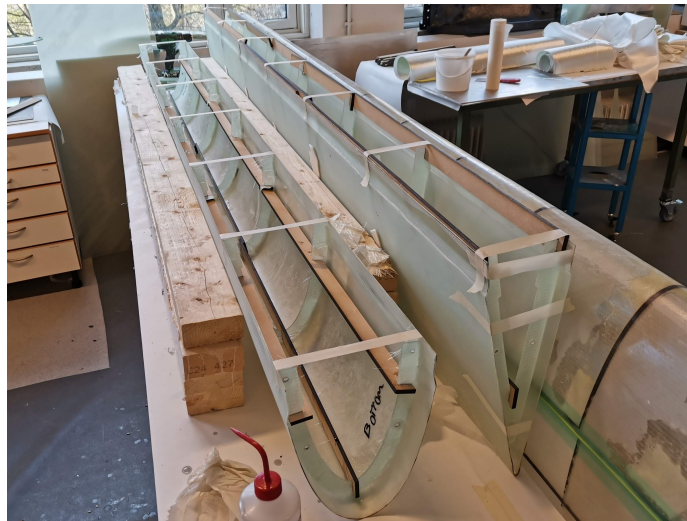


Figure 4.12: The flanges were correctly spaced by the use of slotted bars laser cut from MDF, and adhered with epoxy and CSM.

Up until now it has been claimed that the spacing between the flanges is equal. This is not entirely true. The leading and trailing edges abide by this, but on the side panels the middle and top flanges are adjusted 4 mm upwards. Measurements are given in a drawing in Appendix B. The side panels shall be able to rest atop the profile sections, which in turn rest on the flanges of the leading and trailing edge. This feature is to facilitate assembly, according to step **B6** in the Assembly Guide in Appendix A. Another feature which comes into play here are two taps sticking down from the middle flange through the holes in the section plate. These hinder the side panels from sliding off before being bolted.

The strength of this adhesive joining is an aspect not modelled or investigated in the design/analysis. When gluing, extra care was directed towards the holed flanges, which will connect to the profile sections. These are, with emphasis on the bottom, the ones which are subject to the highest loads. Therefore, these were

adhered with 2-3 layers of glass reinforcement. The preparation of the surfaces is important for proper adhesion. They should be sanded rough and cleaned thoroughly. During the adhesive assembly of the side panels, the realisation arose that working with the wave fabric instead of the CSM was more advantageous. Being thinner, it better adapts to the geometry of the gluing surfaces. Cutting the weave into strips of diagonal orientation promotes every fibre to work for the integrity of the joint.

Assembly of the wing came about very much as planned. Some minor adjustments were required along the way. The top flange in trailing edge was mounted approximately 3 – 4 mm too far back. This caused compression in middle section, leading it to buckle. To fix this, the holes on the trailing edge middle flange were expanded. Other minor adjustments like this were performed.

A4 stainless M6 button head bolts and flange nuts were bought from *skrujernet.no*. These should withstand the marine environment. The bolts are 10 mm long with a head diameter of 13 mm.

The bolting holes in the leading and trailing edge skins were not made until the wing parts were assembled together, and adjusted to satisfaction. To reduce peel-up/push-out delamination, posed as a problem in Section 2.3, a guiding hole using a sharp and fresh small tool was first drilled at very high speed. Then the hole was expanded with the 6 mm tool. This barely caused any delamination visible to the naked eye, incomparable to what occurred at the AWJC holes. The leading and trailing edge had some imperfections, as described in Section 4.1.4. The folds were first cut and ground down. Next, an abundance of epoxy was applied to the whole outside skins of the two parts. The dry spots and porous areas did not completely saturate, but the resin could be clearly seen penetrating into the dry laminate to a large extent. To compensate for the fibre discontinuities, reinforcing plies of fabric were added on the inside where folds had been cut.

The indents in the side panels had to be slightly expanded for the solar panels to fit evenly. It would seem the need for a clearance had been neglected during design. This done, one can see from Figure 4.13 that the solar panels are flush with the skin, coinciding with the intended wing profile. As the solar panel was in place, holes were drilled for bolting. The mounting holes in the solar panel were originally reinforced with metal rings. Removing this lowered the protruding area of the bolt head, as seen if comparing Figure 4.13 (a) and (b), to reduce the drag it creates.

When all adjustments had been made and the whole structure assembled, bolt by bolt was unscrewed and the nuts glued in their respective positions. This is done to facilitate easier assembly. A rapid hardening two-component epoxy glue was used for this.

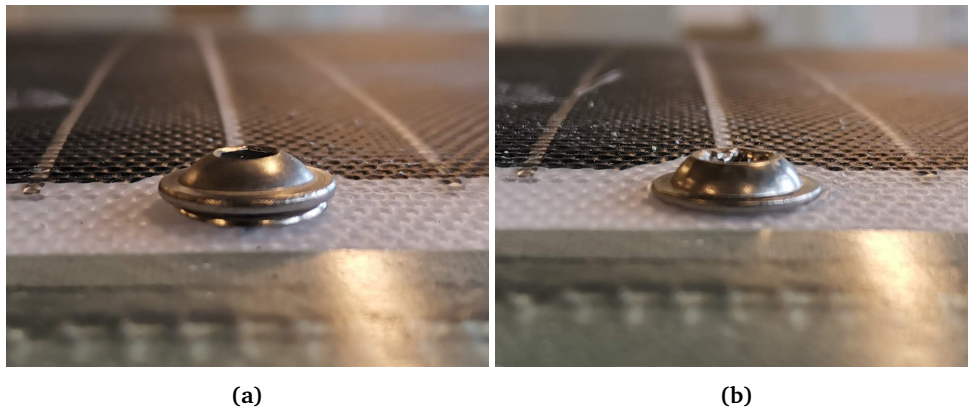


Figure 4.13: Bolting the solar panel (a) before and (b) after removing the metal ring. Note that the solar panel is perfectly flush with the skin.

More extensive reinforcement was added to the bottom wing section than was suggested in Section 3.1.5. The intention there was only to increase the frequency of the eigenmode. However, it is desirable to make the plate stiff enough such that it can hold the weight of the wing before it is bolted in place, referring to step **B3** in the Assembly Guide, Appendix A. The reinforcements seen in Figure 4.14a are 2 cm wide stripes of the same 2 mm laminate that flanges and profile plates were cut from. They were adhered with rapid hardening resin and weave fabric. Some reinforcement was added on the other side of the plate as well, in the longitudinal direction, as seen in Figure 4.14b.



(a) Crossing reinforcement is added under the bottom wing section.



(b) The bottom section is reinforced in the longitudinal direction on the upside, to increase bending stiffness.

Figure 4.14: Bottom section reinforcement.

4.2 Manufacturing the Drive Unit

Table 4.2 summarises the manufacturing or processing of the various drive unit components. It states who performed the operations, which main methods were used and comments on the process and results.

Table 4.2: Summary of components machined for the drive unit.

Component	Method	Performed by	Comments
Shaft bearing support structure, lower	CNC-milling	Workshop personnel	Difficult to machine, the probe of the CNC mill was broken, so workpiece could not be reoriented to be positioned precisely.
Shaft bearing support structure, upper	turning + milling	S.G.	This was turned as one part and cut in the middle. Somewhat difficult to get a precise fit, and to mill the holes in the exact correct positions, but the method is adequate.
Worm Shaft	turning + milling	S.G.	Very precise tolerances were important. Turned out better than expected, at around $+15\mu m$.
Motor flange	turning + milling	S.G.	Precise hole position was difficult due to the authors inexperience. Possible eccentricity.
Motor support bracket	AWJC + welding	Workshop personnel	Very quick and easy, turned out adequate.
Bottom plate	AWJC + CNC-milling	Workshop personnel	Satisfactory result.
Worm gear	turning + drilling	S.G.	A bit difficult to fasten in the lathe chuck for internal turning, as the outside has teeth. Ended up with a little bit eccentricity.
Connector ring	turning + drilling	S.G.	All good.
Box	3d print	-	Not yet manufactured.

4.2.1 Assembly

The assembly guide in Appendix A contains a detailed list of components, including type and quantity of bolts required for assembly.

The bottom plate was fastened with the 5 M6 bolts through the bottom section plate. Steel back plates were made for each hole, to increase the area on which the load acts. These exposed steel parts must be coated before launching the vessel on the water, to protect against corrosion.

The sealing ring fit into the bottom plate was very tight and it was forced in with a rubber hammer. To get it out again without damaging it would be difficult or impossible. Figure 4.15 shows the seal inserted.



Figure 4.15: The sealing ring fitted into the bottom plate.

The bearings were heated to 170°C and the worm cooled to -20°C . Using a manual hydraulic pump, the bearings were pressed in place. After assembly, the bearings turned with slightly more resistance than before, indicating that the pressing process was a bit recklessly performed and loading of only the outer ring happened.

The shaft with bearings sat nicely into the support. The tight fit and poor alignment of the holes in the upper parts, mentioned in Table 4.2, made the bolts hard to tighten, but it all came together very well.

With the worm and worm gear interlocking nicely, the gear was bolted to the connector ring. Four holes were drilled in the mast through the existing holes in the ring, and tapped to M8 such that it was fixed in the precise correct position.

One of the bolts for fastening the motor connector bracket is somewhat difficult to access.

The slip ring stator locks to the mast with four set screws. A hole in the mast was drilled right above the slip ring, which wires were pulled through. As may be noticed in Figure 4.16, proper wiring has not been done, only an interim connection for testing.

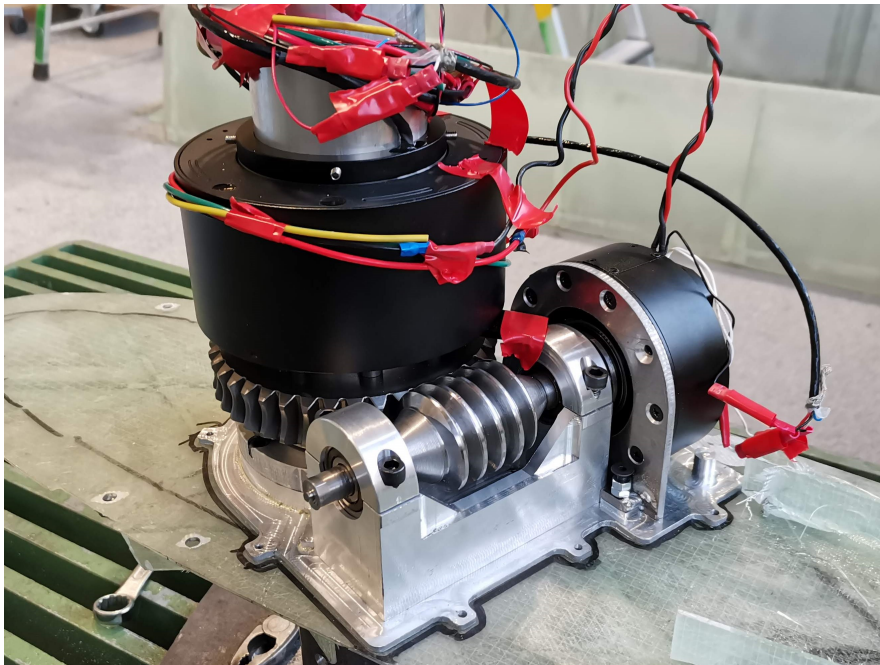


Figure 4.16: The drive system assembled.

4.3 Estimation of Cost

Table 4.4 sums up the estimate cost of producing one wing. The various posts are elaborated below. No freight charges are included in any of the cost estimations.

The weave fabric was bought from *easycomposites.co.uk* [35] at £2.02 per meter. The price per square meter of the biaxial fibre from *Saertex*, which was not used, is almost the same at €1.93. 6 plies of fabric in 4 wing components

Table 4.3: Cost of consumables for one VARTM process of a component of approximately 2.5 m length.

Product	Price £	Amount	Cost £
Sticky tape	3 / 15 m roll	1	3
Flow Mesh	1 / m ²	2.5	2.5
Vacuum bag	1 / m ²	3	3
Tube	0.5 / m	5	2.5
T-piece	0.5 / pc	6	3
Peel ply	1.3 m ²	2.5	3.25
Spiral tube	0.2 / m	2	0.4
SUM £			18.65
SUM NOK			220

Table 4.4: Estimation of cost for the wing, excluding the drive unit.

Product	Price NOK	Amount	Cost NOK
Fibre	23.8 / m	58 m	1400
Epoxy	100 / kg	15 kg	1500
Consumables	220 / process	6	1260
Mast	750 / 6 m	3 m	375
Bolts & nuts	2.06 / pair	81	167
Labour	500 / h	40 h	20000
SUM		≈	25000

2.4 m long amounts to 58 m. This is accounting for any cut-off as waste, while it may actually be used for other applications.

The prices for the epoxy system are volatile and vary a lot depending on quantity and market, but it lay around NOK100/kg the last time it was purchased to the composite lab. Knowing the wing is 20 kg, assuming a fibre fraction of 50% yields 10 kg. If one adds 50% waste the figure reaches 15 kg, which is quite close to what was consumed according to Table 4.1.

For the VARTM process consumables, prices are retrieved from *easycomposites.co.uk*. Prices are in British pounds, and converted to NOK at a rate of $\frac{NOK}{£} 11.8$ (May 26 2021). Table 4.3 summarises this considering a component of the approximate size as each wing laminate part.

To estimate a cost of labour, the hours invested by the author does not give a realistic picture. It has been a simultaneous development, manufacturing and learning process, where achieved efficiency has been nowhere near an acceptable production standard. Imagining the time every operation would take with the

Table 4.5: Cost of components purchased for the drive unit. Dollar rate of 8.4 used.

Part	Price	Price NOK
Worm Gear	NOK1892	1892
Worm	NOK1658	1658
RMD-X8 Pro	\$492	4132
Slip Ring	\$232	1949
Mast Bearing	NOK890	890
Shaft Bearings	NOK546	546
Simmer Rings	NOK173	173
SUM		11240

acquired level of experience, and eliminating all the mistakes made, an order of magnitude may at least be approximated. Spending 20 hours on VARTM processes and 20 hours on post processing and assembly should be possible, amounting to 40 hours total labour per wing. Some process improvements are discussed in Section 6.2.

Table 4.5 lists the price of all components purchased for the drive unit, freight charge not included. The components machined in-house are not included here.

Chapter 5

Experimental Testing of the Wing Assembly



Figure 5.1: Full experimental setup for wing stiffness and actuation testing.

In order to evaluate the performance of the design and prototype, a test campaign was executed at the lab. Part one was an evaluation of the mass. Part two concerned ease of assembly. In part three, deflection under load was measured for the GFRP wing and the CFRP wing for reference. Part four investigated the actuation of the GFRP wing under load.

5.1 Experimental Setup and Method

5.1.1 Test 1 - Mass

Mass is an important aspect according to objective 2 from Table 1.1 in Section 1.5. To evaluate this, components were weighed on a scale.

The various parts of the GFRP wing were weighed separately, on a digital scale normally used for resin mixing. This has a resolution of 0.1 g, and a range up to 15000 g. The carbon wing does not disassemble and its mass exceeds that range. It was therefore placed on an old mechanical scale, with a resolution of 0.1 kg.

5.1.2 Setup

The wing is oriented vertically, similar to the real situation. To facilitate this, a base was made. A 120 mm long section of steel tube was turned internally to act as a socket to fit around the 70 mm mast. It has a hole for an M10 bolt to lock the rotation. The socket was then welded to a square steel plate with holes in the corners. A additional hole in the bottom of the socket lets wires run through. The plate was bolted to a large steel table for required stability. The full setup is seen in Figure 5.1.

5.1.3 Test 2 - Assembly

According to objectives 4 and 6 from Table 1.1 in Section 1.5, simple and intuitive assembly is of high importance. Now, the assembly might be intuitive and quick for the author, who has created the design and repeatedly assembled and disassembled. Someone unfamiliar with the design, however, could think in a different way. Therefore, two subjects were invited to perform an assembly. The achievement of an intuitive design is quantified in terms of the time spent on the procedure and compared.

With reference to the assembly guide, Appendix A, the starting state is according to step **B0**. The timed procedure includes step **B1** through **B7**. The test subjects were first given up to five minutes to study the assembly guide. Then the timer started and was stopped when the wing was fully assembled.



Figure 5.2: Experimental setup for both wings. One ruler above the mast axis and one behind the trailing edge. The line running to the pulley and down to the load can also be seen.

5.1.4 Test 3 - Static Loading

At the top trailing edge of the wing a connection point in the form of a V-shaped steel plate with a large nut welded on it, was adhered at a distance of $a = 910 \text{ mm}$ from the mast axis. From this, a rope runs horizontally to a pulley and down. At the end of the line, weights would be added as seen in Figure 5.4a. The pulley is assumed ideal, such that the force acting on the wing is $F = m \cdot g$, where m is the total mass of the weights in kg and $g = 9.81 \frac{\text{m}}{\text{s}^2}$ is the acceleration of gravity. This will then equvalate a torsional moment about the mast axis $T_m = F \cdot a$.

Deflection was measured at two points, as visualised in Figure 5.3. The first was straight above the mast axis, the second at the trailing edge tip top. Measurements were obtained visually against rulers with 1 mm resolution, and noted on sight. The distance from the wing to the ruler was slightly different for the two

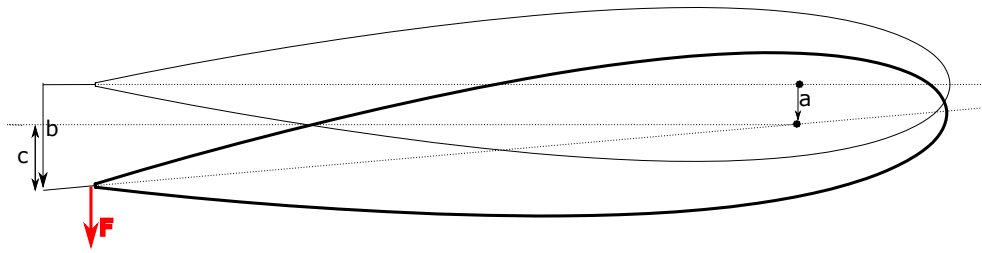


Figure 5.3: The two measurements of deflection at the top of the wing: (a) mast axis and (b) trailing edge. (c) illustrates the difference between the two.

setups. The relative error due to this, however, is way smaller than the accuracy of the visually attained measurements. 5 cm higher measurement at the top of the wing causes an approximate 2% overestimation of deflection. This is neglected. In Figure 5.2 you see the two rulers and the line running through the pulley.

Weights were added in incremental steps. 1, 4 and 10 kg were used. At each load level, deflections were noted and the whole structure visually inspected, looking for any signs of damage or misalignment. Any damages to the prototypes were not wanted, in accordance with the intention of leaving a functional prototype, Table 1.2. To ensure the testing remained nondestructive, the loading was stopped before approaching design level. The nature of the load, acting in one extremity of the wings, is unrealistic and its local effects on the structure unknown.

For boundary condition A, the bottom of the trailing edge was blocked from moving, see Figure 5.4b. This was to better isolate the torsional behaviour of the wing.

Under boundary condition B, the worm gear was engaged to stop the rotation of the GFRP wing. For the CFRP wing, the rotation was stopped by a bolt through the mast base.

5.1.5 Test 4 - Actuation

Actuating the wing, there are some aspects of interest:

- Does the mechanism run smoothly?
- Under how much load can the actuator move the wing?
- How much power is used?
- Are there any signs of damage, strains, yielding, misalignment etc?

The test setup was equal to test 3B, with the mast base fixed and point load at the upper trailing edge. First unloaded actuation was performed. Subsequently weights were added in steps. After testing the assembly was visually inspected,

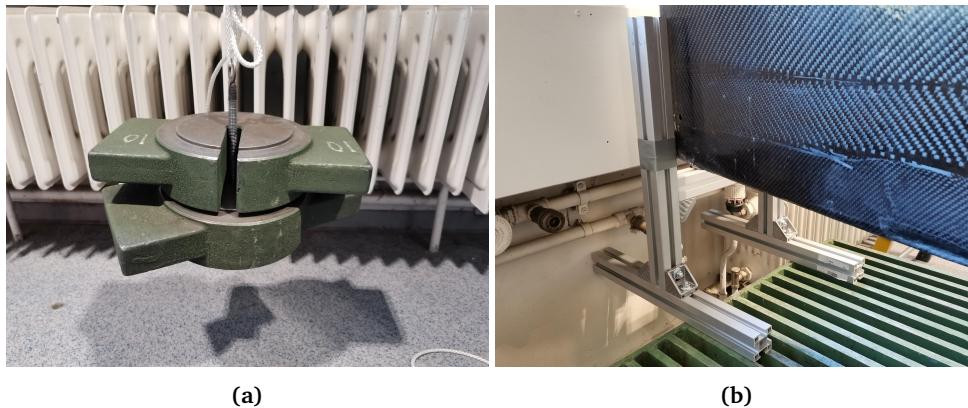


Figure 5.4: (a) Two 10 kg weights. (b) The structure blocking the rotation of the bottom of the wing as boundary condition A.

then disassembled and parts inspected individually.

The actuator used was one not fully functional. It only works in certain control modes, and has some unhealthy noise to it. Damages most likely stemming from intrusion of a foreign object and/or previous uneven loading. So it did probably not run at full capacity.

The actuator was controlled through a manufacturer test software in speed control mode, where the angular velocity of the rotor is given in degrees per second. Dividing by the internal gear ratio of 6 and worm gear ratio of 40 yields wing angular velocity. The motor was energised from a power supply at $V = 30.26\text{ V}$. The optimal working voltage is 48 V . Current draw I was noted from the monitor of the power supply. Power is calculated as by $P = V \cdot I$.

5.2 Results

5.2.1 Test 1 - Mass

Results from the weigh-in are given in Table 5.1 and Table 5.2. They are discussed in Section 6.1.1.

Table 5.1: Weighed mass of the carbon fibre wing.

Component	Measured [kg]
CFRP wing	19.9
Mast base	4.3

Table 5.2: Calculated and measured mass for the GFRP wing components.

Component	Calculated [g]	Measured [g]
Leading edge	2820	3536
Trailing edge	3606	4760
Left side	3383	4326
Right side	3383	4353
Top section	594	681
Middle section	594	632
Bottom section	594	1327
81 bolts		291
SUM WING	14974	19906
Bottom section w/mast		(3322)
Solar panel	3650	4580
Mast		5340
TOTAL		36401

5.2.2 Test 2 - Assembly

Table 5.3 shows the resulting times from the test subjects. Several suggestions to improvements of the assembly guide were brought forth by the test subjects, and updates were made. The results are discussed in Section 6.1.2.

Table 5.3: Results of timed wing assembly.

Subject	Time
S.G.	24 m 45 s
1	36 m 10 s
2	42 m 30 s

5.2.3 Test 3 - Static Loading

Results from the stiffness tests 3A are given in Table 5.4 and Table 5.5, and for stiffness tests 3B in Table 5.6 and Table 5.7. Figure 5.5 and Figure 5.6 respectively visualise the deflections. Results are discussed in Section 6.1.3.

Table 5.4: Carbon fibre wing test results under point load with bottom rotation stopped. Δ is the difference between mast and tail.

Test 3A-CFRP			Deflections [mm]				
m	F	T_m	Mast		Tail		
[kg]	[N]	[Nm]	Measured	Relative	Measured	Relative	Δ
0	0	0	213	0	308	0	0
1	9.8	9	214	1	309	1	0
3	29	27	217	4	312	4	0
5	49	45	220	7	315	7	0
7	69	63	222	9	317	9	0
10	98	89	225	12	320.5	12.5	0.5
13	128	116	229	16	324	16	0
15	147	134	230	17	326	18	1
17	167	152	232.5	19.5	328	20	0.5
20	196	179	235.5	22.5	331.5	23.5	1

Table 5.5: Glass fibre wing test results under point load with bottom rotation stopped. Δ is the difference between mast and tail.

Test 3A-GFRP			Deflections [mm]				
m	F	T_m	Mast		Tail		
[kg]	[N]	[Nm]	Measured	Relative	Measured	Relative	Δ
0	0	0	115	0	264	0	0
1	9.8	9	116.5	1.5	265.5	1.5	0
3	29	27	121.5	6.5	270	6	-0.5
5	49	45	127	12	276	12	0
7	69	63	132.5	17.5	281.5	17.5	0
10	98	89	138	23	288	24	1
13	128	116	144	29	294	30	1
15	147	134	147.5	32.5	297.5	33.5	1
17	167	152	150	35	301	37	2
20	196	179	155.5	40.5	307	43	2.5

Table 5.6: Carbon fibre wing test results under point load with mast base fixed. Δ is the difference between mast and tail.

Test 3B-CFRP			Deflections [mm]				
m	F	T_m	Mast		Tail		
[kg]	[N]	[Nm]	Measured	Relative	Measured	Relative	Δ
0	0	0	212	0	293	0	0
1	9.8	9	214	2	295	2	0
3	29	27	215.5	3.5	299	6	2.5
5	49	45	218.5	6.5	305.5	12.5	6
7	69	63	220	8	311	18	10
10	98	89	224	12	321.5	28.5	16.5
13	128	116	227.5	15.5	329	36	20.5
15	147	134	229.5	17.5	335.5	42.5	25
17	167	152	230.5	18.5	340	47	28.5
20	196	179	235	23	351	58	35

Table 5.7: Glass fibre wing test results under point load with mast base fixed. Δ is the difference between mast and tail.

Test 3B-GFRP			Deflections [mm]				
m	F	T_m	Mast		Tail		
[kg]	[N]	[Nm]	Measured	Relative	Measured	Relative	Δ
0	0	0	111	0	215	0	0
1	9.8	9	112.5	1.5	216.5	1.5	0
3	29	27	115	4	221.5	6.5	2.5
5	49	45	120	9	228	13	4
7	69	63	123	12	234	19	7
10	98	89	128	17	244	29	12
13	128	116	133	22	252	37	15
15	147	134	136.5	25.5	258	43	17.5
17	167	152	142	31	265	50	19
20	196	179	146.5	35.5	278	63	27.5

Note: Movement in the fixing bolt/hole at base, possible yielding in the mast around the hole. Contributor to rotation, observed in loading condition B for both wings.

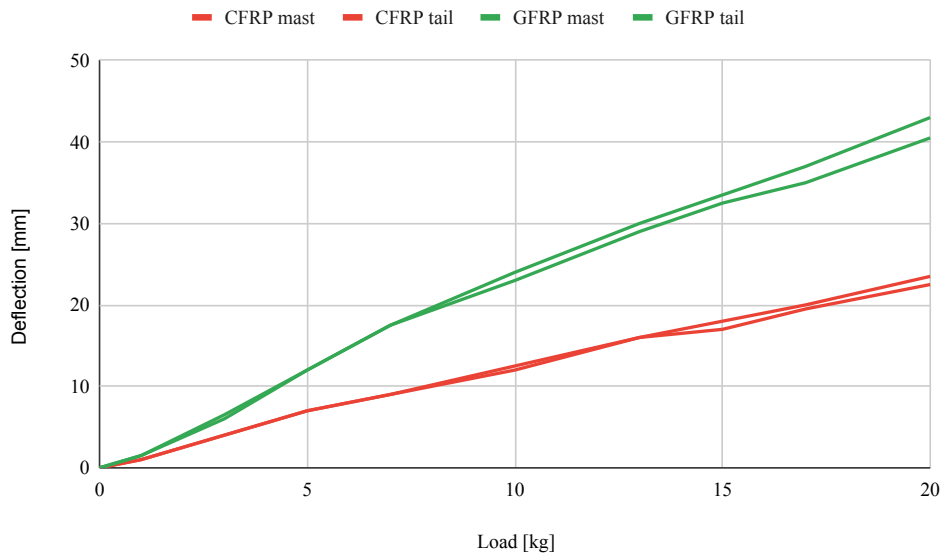


Figure 5.5: Graphical representation of the deflections of the two wings in test 3A.

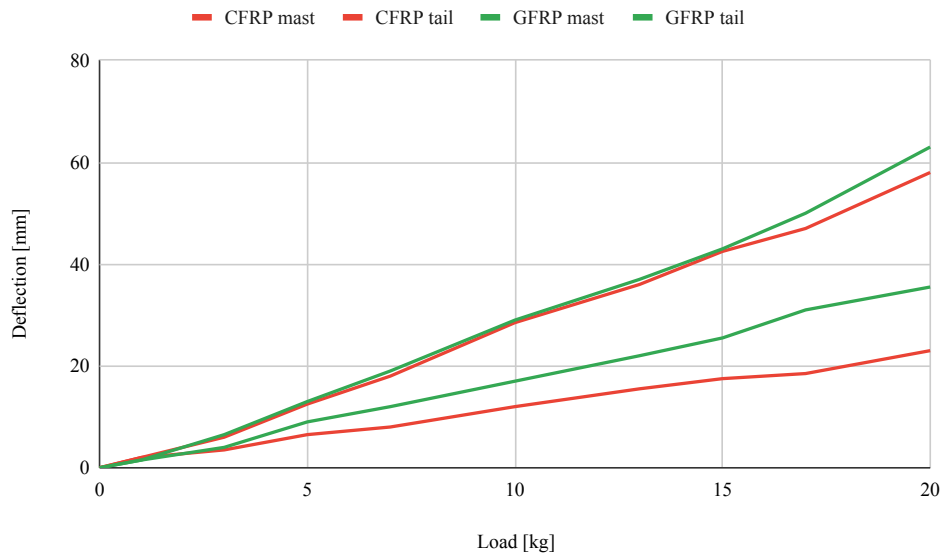


Figure 5.6: Graphical representation of the deflections of the two wings in test 3B.

5.2.4 Test 4 - Actuation

Results from the unloaded actuator test are given in Table 5.8 and graphically visualised in Figure 5.7. Results from loaded actuation is found in Table 5.9. Results are discussed in Section 6.1.4.

Table 5.8: Current draw at various speeds, no load.

Speed control [$^{\circ}/s$]	Equivalent wing angular velocity [$^{\circ}/s$]	Current Draw [A]	Power [W]
0	0	0.03	0.9
200	0.8	0.07	2.2
500	2.1	0.11	3.4
1000	4.2	0.16	4.9
2000	8.3	0.28	8.5
3000	12.5	0.38	11.6
4000	16.7	0.52	15.6
5000	20.8	0.66	19.9

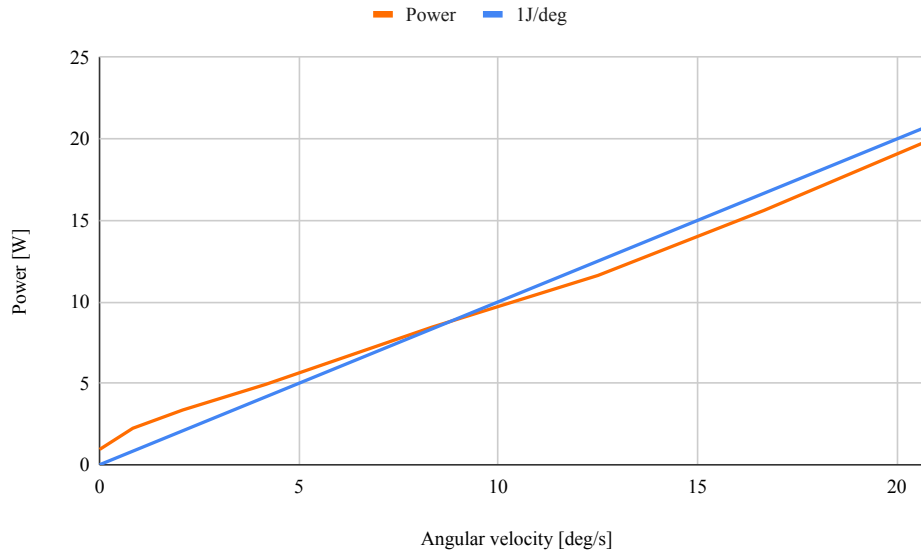


Figure 5.7: Power consumption of unloaded actuation compared to the linear $1J/^{\circ}$.

Table 5.9: Results of loaded actuation test. Power listing applies to the highest current value in each row.

m	T_m	Response	Current Draw [A]			Power [W]
[kg]	[Nm]		Speed control [$^{\circ}/s$]:			
			$\nu = 100$	$\nu = 200$	$\nu = 500$	
0	0	yes		0.07	0.11	3.4
3	27	yes		0.20	0.29	8.7
5	45	yes		0.33	0.45	13.6
7	63	yes		0.48	0.64	19.4
10	89	yes		0.78	0.97	29.4
13	116	yes		1.40	1.47	44.6
15	134	yes, yes, <u>no</u>	1.38	1.46	<u>1.74</u>	<u>52.7</u>
16	143	yes	1.45			43.7
17	152	5 sec and <u>stop</u>	<u>1.61</u>			<u>48.6</u>

Notes:

- No slippage of the gear.
- No aural indications of improper function.
- Unlimited number of wing revolutions.
- No direct visual signs of damage in individual components.
- One of the bolts holding the motor support bracket had come slightly loose.
- Possibly a little bit more slack than before in the gear engagement.

Chapter 6

Discussion

In this chapter what has been done and achieved is discussed with respect to the research questions in Table 1.2 and objectives in Table 1.1.

6.1 Lab tests

6.1.1 Test 1 - Mass

The four main wing components are between 26 % and 32 % heavier than theoretical mass imply, Table 5.2. The main contributor to this is the epoxy and fibre used for assembly. Around 50 g per part come from the nuts. In hindsight, the parts should have been weighed before gluing. This would have brought better insight into the extra weight added by the epoxy, and fibre fraction could potentially have been calculated. However, we do know the leading and trailing edge processes were bad, leading to a thickness different from the ideal. The extra weight of the bottom section naturally comes from the reinforcements not present in the CAD model. All over, 33 % more mass than calculated is not bad.

The CFRP wing made by [5] had a as mentioned in Section 3.1.1 a theoretical mass of 4.5 kg, but somehow ended up at close to 20 kg, Table 5.1. How this came to be is not much of interest here. What is interesting is that the GFRP wing, i.e. without the mast, clocks in at approximately the same mass. Including the mast in this, but neglecting the solar panels, a 36 % increase of mass is the price paid for the change to a considerably cheaper material, as a compromise between objectives 2 and 3 - mass and cost.

The solar panels each weigh 930 g more than claimed by the supplier, i.e. 25 % extra. This is a serious contribution to the total mass of the wing.

Being a main contributor to the total mass of the assembly, replacing the aluminium mast with filament wound glass fibre could benefit in reducing the mass.

This however, comes at a higher cost.

For transportation purposes, the total mass of the wing is not very relevant. In the disassembled state, no component exceeds 5.5 kg. In terms of objective 6 in Table 1.1, they are no issue for any one person to carry.

6.1.2 Test 2 - Assembly

Comparing the assembly times in Table 5.3, the two first-time test subjects spent an average of 57% longer than the author. They both found the instructions understandable and the design reasonable. This can be taken as indication of good coherence with objectives 4 and 6 in Table 1.1, i.e. design for assembly and user friendliness. There is nonetheless no doubt that assembly will be more demanding on a floating vessel than a static fixed support in the lab.

6.1.3 Test 3 - Static Loading

Results of the stiffness testing are presented unaltered in Section 5.2.3.

To comment on the setup, there are a few sources of error. First it must be noted that the measurements of deflection are obtained visually. They are given to the half millimetre, but this may be imprecise within approximately ± 0.5 mm. Second, the force is not as precise as given, as the line running through the pulley causes some loss, though minor. Lastly, as noted with the results, the mast fixture at base was improper, and accounts for some rotation under boundary condition B. Up to 10 mm of the final difference can possibly be attributed to this, for both wings.

Under boundary condition A, if we assume the response can be split into bending and twisting by the principle of superposition, the main takeaway is the wing resistance to torsion. The carbon fibre wing only displays a difference of 1 mm between mast axis and trailing edge at the highest load step, according to Table 5.4. At the same load, the glass fibre wing in Table 5.5 exhibits a difference of 2.5 mm. This is 2.5 times more compared to the carbon fibre wing, or 0.4 times the stiffness.

The result of the finite element model in Section 3.1.4 under 211 Nm torsion was 3.78 mm. With a linear response, this suggests 3.2 mm at 178 Nm. Comparing the measured 2.5 mm of deflection to this, keeping our sources of error in mind, corresponds very well. This provides faith that the FEA model is not entirely unrealistic.

Under boundary condition B the total deflections, given in Table 5.6 and Table 5.7, increase considerably. This is not at the mast axis though, but at the trailing edge.

The difference in deflection here corresponds to 1.7° rotation. However, the aforementioned source of error in the poor fixture of mast base, discredits the accuracy of this result. Be as it may, these deflections are not impacting the wing function. Such high torque occurs only when the wing is in the stalled condition, and precise angle is not of importance.

Affecting the test results for the carbon fibre wing, is that it has an aluminium mast piece as connection between the carbon fibre mast and the base. Some of the bending action can be attributed to this, which is not intended in the design.

The deflection of the GFRP wing is dominated by the bending of the mast. It becomes apparent that the mast itself might be underdesigned with regards to stiffness. Its dimensions were set in [10] based on static stress and deflection evaluation, but the deflectional constraints were probably too loose, and no investigation in the dynamics was performed. These aspects should have been returned to in the re-analysis of the wing.

All in all, the glass fibre wing is between $\frac{1}{2}$ and $\frac{1}{3}$ as stiff as the carbon fibre wing.

6.1.4 Test 4 - Actuation

The contents of this subsection refers to the actuation test results in Section 5.2.4.

Referring to Table 5.9, the wing let itself actuate without issue up to a load equivalating $140 Nm$ of torsional moment about the mast. This is about 60% of the stated design torque in Table 1.5.

Knowing from Equation (1.1) that the wind force is proportional to the square of the wind speed, turning against $16 \frac{m}{s}$ wind corresponds to $135 Nm$ by the same model. In terms of prototype sea trials, such weather conditions are rare on the Trondheim Fjord as well as being outside the scope of safe testing. Based on this, the actuation will suffice for any load condition experienced during vessel tests in the foreseeable future.

A question is whether not reaching design torque can be attributed to dysfunction of the actuator and lower working voltage V , as implied in Section 5.1.5. The fully functional motor might still provide sufficient power. If this is not the case, it means the frictional losses in the mechanism are ridiculously high. $35 Nm$ motor torque through a 40:1 gear ration not sufficing to produce $211 Nm$, would correspond to a total mechanism efficiency $\eta_{tot} \leq 0.15$. The gear itself is stated with $\eta = 0.46$, so expected efficiency should be somewhat lower than this, $\eta_{tot} \in (0.30, 0.45)$. Having a look at the current and power of the motor in Table 5.9 confirms the suspicion that the actuator can be blamed. The motor stalls out at

around $1.7A$, corresponding to a power of $50W$. According to the actuator data sheet in Appendix D the motor has a nominal current of $6.5A$ and power of $330W$. This leaves no doubt that it is the deficiency of the actuator preventing the reaching of the design load.

The motor support bracket must be improved. The fact that a bolt had begun to come loose means that there had been movements of the bracket. A simple improvement of the bracket design is suggested in Figure 6.1. The movement itself, however, indicates transmission of forces, axial or radial, through the shaft-to-motor connection. This could be due to eccentricity of a poorly made motor connector flange, as mentioned in Table 4.2. Along with the knowledge attained in Section 3.2.4 that this connection is a weak point, machining a new connector flange according to the suggested design in Figure 3.22 should be a priority. The shaft has been left with excess material on the opposite end, which the counterpart of the connection can be milled from.

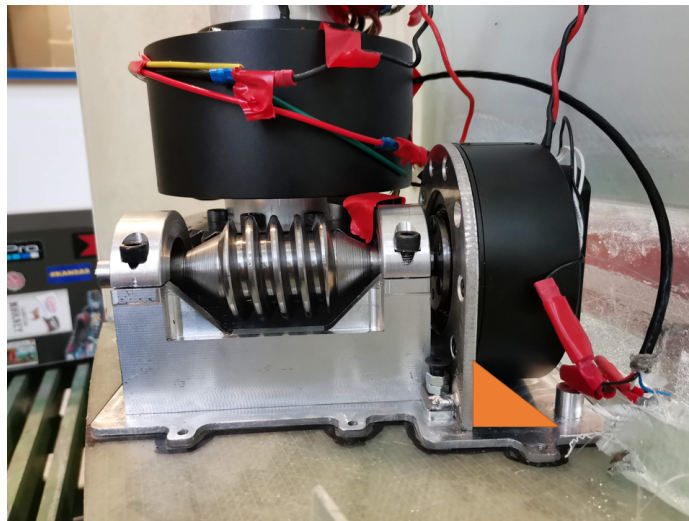


Figure 6.1: The orange triangle indicates a suggested improvement to the motor support bracket.

It was hard to tell if there had really been a change, but if the slack in the gear had increased, it means the mast and shaft axes had diverged. This may come from yielding of the bottom plate. The contact force from the worm gear has a component normal to the worm shaft axis which was not considered. The slack may also stem from play in and around the mast bearing. It might be that a double row rather than single row deep groove ball bearing would provide better stability. A stiffer bottom plate would probably be a good idea anyway.

Despite the manufacturer stressing that the gear couple is not self locking, no slippage seem to occur. Presumably this means that the friction in the bear-

ings and actuator provide enough resistance to counteract this. In terms of power consumption, as highlighted by [2] in Section 1.2, this means the actuator can entirely shut off and draw zero current while the sail maintains a position.

While the wing is in the lift condition the resultant force should go through the mast axis due to the rig being balanced, as discussed in Section 1.2. This means we can draw parallels to the unloaded test results in Table 5.8. At the angular velocities from $10^\circ/s$ to $20.8^\circ/s$, Figure 5.7 clearly shows that energy consumption is less than 1 joule per degree. Exemplifying, this means that the energy demanded to move the wing 90° , i.e. $90J$, can be produced by a $150W$ solar panel with decent conditions in *one second*. Adding to this that the wing might stand still for minutes between each actuation, the drive unit can definitely be claimed to adhere to the overall vessel design requirement of self-sustainable power consumption/generation in Table 1.4.

The deflection of the wing/mast under load does not seem to have any implications of the function of the drive system.

6.2 Manufacturing Methods and Cost

Despite the unsuccessful sealing of the leading and trailing edge moulds, causing imperfect components in Section 4.1.4, the mould concept for the manufacturing of these components is adequate. With proper sealing, and not half-measure attempts at such, there is no apparent reason for a more advanced mould type. One improvement should be to use a few plies of thinner fabric to make the mould skins, as this could make a better and more even laminate, also less prone to delamination upon demoulding.

A bit more extra room along the mould edges would be beneficial, as the 10 cm added to the mould rib in Figure 4.5 were somewhat tight to work with. Regarding the offset from the wanted profile, going all the way to 5 mm along the connecting edges was excessive. The intention was to reinforce the side panels along this edge with $1 - 2\text{ mm}$, but this seems not necessary. So a 3 or 3.5 mm offset here would be better.

Stacking the fabric plies would have been substantially easier using the proper biaxial fibre instead of the angled weave. An estimated hour would be cut off the time preparing the stack. The problem of unevenness/folds in the component skin should also be eliminated by this, attributing to a better final product.

The AWJC introduced some delamination in the laminates. With proper tuning of parameters, this can to a large extent be avoided and the method is suitable

and efficient.

The strength of the adhesive joints between skins and flanges is still not known. We have seen that they can handle the loads applied during the test campaign, but these tests have been designed to be non-destructive and not push any limits. The joining could be too weak and a source of failure, or it could be plenty strong with excessive reinforcement. If the first is the case, the bottom flanges are experiencing the highest loads and is most likely to fail.

The lack of post-curing at elevated temperature means the matrix properties are different from the optimal. The structural effects of this are not too great, as the stiffness of the composite laminate is mainly ruled by the fibres. Yet, for production, the issue of post curing should be solved.

One could consider buying bolts which are 2 mm longer. In some of the connections of the wing it can be difficult to get the bolts to enter the nut threads.

The way the bottom wing section is connected to the box bottom plate is not ideal, and another possible locus of failure. The bottom plate and section could have been assembled before the addition of stiffeners, such that one larger back-plate could be applied to distribute the load over a larger area.

It is evident from Table 4.4 that the by far largest contribution to the cost of the wing is labour. This in itself is an estimation with massive uncertainties. The material cost below NOK5000 is very low, of which less than NOK1500 stem from the fibre. Carbon fibre fabrics cost between 10 and 30 times more than glass, by price comparison at easycomposites.co.uk. Less material is naturally needed when building with carbon fibre than glass. Yet, if half the amount is used of the cheapest carbon fibre cloth, it still amounts to NOK7500 for reinforcement or NOK11000 total. With a more expensive carbon fibre, like the PrePreg used by [5], the total might reach NOK18500. This indicates material cost savings in the regime 55% – 75%.

Measures to reduce manufacturing time may bring much larger savings than reducing epoxy waste or negotiating lower material prices. A larger mould surface could for instance allow the VARTM of both side panels in one process, and the same for internal structure. This eliminates setup time for two processes. Minimising the number of gates and vents, as experienced through the processes in Table 4.1, also reduces the setup time.

The wings ability for disassembly increases the complexity of the manufacturing process, and thereby the number of hours of labour. The advantages of this must be weighed up against the added cost it entails. This is something that cannot be answered now, but is to be learned over the next phases of the ORCA project.

CNC is expensive and time-consuming. There are 9 components to the actuation mechanism which require machining. The simpler these operations are, the lower the cost. If the mechanism can be assembled mainly from sheet metal and/or water jet cut plate parts, cost can be assumed to go down considerably. This would further increase the coherency with objectives 3 and 5 in Table 1.1. Such improvements should be investigated if the ORCA is to go into batch production.

The drive unit design rests largely on the criterion from subsection 3.2.3 of unlimited rotation, with the advantage of improved manoeuvrability. Limiting the rotation to e.g. $\pm 90^\circ$ or $\pm 180^\circ$ would have brought some other advantages and a simpler design. First of all continuous wiring into the wing could have been used, eliminating the cost, mass and complexity brought by the slip ring. Introduction of a linear actuator would have been possible, simplifying the whole drive unit. Even though these arguments can make it seem like limited rotation is more advantageous for increased integrity by lowered complexity, the picture is on so simple. Better manoeuvrability may assist in significantly decreasing the loads experienced, e.g. when turning the boat on a down wind course, and ensure better survival of the vessel that way.

Chapter 7

Conclusion

7.1 Conclusion

To answer the research questions in Table 1.2 a full scale prototype glass fibre reinforced polymer GFRP rigid wing with internal actuation through a worm gear transmission has been developed, built and tested.

Testing of the prototypes in the lab show that the glass fibre wing design has lesser, but comparable, properties to the carbon fibre wing. Performance relating to objective 1 - rigidity - of Table 1.1, has been evaluated through static load tests. The GFRP wing is between $\frac{1}{2}$ and $\frac{1}{3}$ as stiff as the CFRP wing. The largest contributor to the GFRP wing compliance is the aluminium mast, which may be underdesigned. Yet, the deflections are small enough that they do not seem to impact the function of the wing. Considering objective 2 - mass - the glass fibre wing is 36% heavier.

Vacuum assisted resin transfer moulding VARTM has been used to manufacture GFRP components, and has proven itself suitable. A low cost, lightweight mould was developed, and the resulting components are adequate despite some imperfect processes. When manufacturing with glass fibre material costs are very low, totalling below *NOK*5000 and cohering well with objective 3. Labour is what drives the cost of the wing up. The wing design facilitates disassembly according to objective 4, and this increases complexity and manufacturing time. The total evaluation of this design boils down to how you value objectives 1, 2 and 3, in this compromise between rigidity, mass and cost.

The worm gear drive unit works as intended for angular positioning. The wing maintains its orientation without use of energy, due to the self-locking capabilities of the transmission. In testing, actuation was only achieved up to 67% of the 211 Nm design load due to a malfunctioning motor, while at full effect the data implies that it should be achieved with ease. The drive unit is contained within an oil filled compartment to protect against corrosion.

According to objective 4 and 6, the wing may be disassembled for easy transport and storage, with all components weighing 5 kg or less. The structure may be assembled in 25 minutes by trained and 40 minutes by untrained personnel.

This design entails a lot of compromises which cannot here and now be determined if are justifiable. Some open questions are:

- Is this reduction of stiffness worth the cost savings?
- Is the added mass worth the cost savings?
- Is the fixed mast and actuation within the wing beneficial when considering vessel robustness?
- Is disassembly of the wing advantageous, and worth the reduction of rigidity and added cost it entails?

Only proper and repeated vessel trials and testing may shed light on this.

At the time of writing the prototype is as good as ready to be mounted on a hull and taken out to sea, in accordance with the intention in Table 1.2. The reader is very much advised, if he or she wants a proper understanding of this product, to have a look at the assembly guide in Appendix A.

Bibliography

- [1] R. Stelzer and K. Jafarmadar, 'History and recent developments in robotic sailing,' in *Robotic sailing*, Springer, 2011, pp. 3–23.
- [2] M. F. Silva, A. Friebe, B. Malheiro, P. Guedes, P. Ferreira and M. Waller, 'Rigid wing sailboats: A state of the art survey,' *Ocean Engineering*, vol. 187, p. 106 150, 2019.
- [3] (), [Online]. Available: <https://www.nationalgeographic.org/encyclopedia/ocean/> (visited on 08/06/2021).
- [4] J. Kimball, *Physics of sailing*. CRC Press, 2009.
- [5] M. Dyrseth, 'Development and design of a wingsail for an autonomous surface vessel,' 2019.
- [6] M. Neal, 'A hardware proof of concept of a sailing robot for ocean observation,' *IEEE Journal of Oceanic Engineering*, vol. 31, no. 2, pp. 462–469, 2006.
- [7] (), [Online]. Available: <http://www.sailbuoy.no/> (visited on 24/05/2021).
- [8] (), [Online]. Available: <https://www.saildrone.com/> (visited on 24/05/2021).
- [9] R. Gården Rovik, 'The concept development for designing an autonomous sailboat,' 2017.
- [10] S. Gauden, 'Development and prototyping of an ocean going autonomous surface vessel for research applications,' 2020.
- [11] R. F. Gibson, *Principles of composite material mechanics*. CRC press, 2016.
- [12] K.-T. Hsiao and D. Heider, 'Vacuum assisted resin transfer molding (vartm) in polymer matrix composites,' in *Manufacturing techniques for polymer matrix composites (PMCs)*, Elsevier, 2012, pp. 310–347.
- [13] S. Van Oosterom, T. Allen, M. Battley and S. Bickerton, 'An objective comparison of common vacuum assisted resin infusion processes,' *Composites Part A: Applied Science and Manufacturing*, vol. 125, p. 105 528, 2019.
- [14] H. Rydarowski and M. Koziol, 'Repeatability of glass fiber reinforced polymer laminate panels manufactured by hand lay-up and vacuum-assisted resin infusion,' *Journal of Composite Materials*, vol. 49, no. 5, pp. 573–586, 2015.

- [15] R. Komanduri, 'Machining of fiber-reinforced composites,' *Machining science and technology*, vol. 1, no. 1, pp. 113–152, 1997.
- [16] B. Kavad, A. Pandey, M. Tadavi and H. Jakharia, 'A review paper on effects of drilling on glass fiber reinforced plastic,' *Procedia Technology*, vol. 14, pp. 457–464, 2014.
- [17] U. A. Kumar, S. M. Alam and P. Laxminarayana, 'Influence of abrasive water jet cutting on glass fibre reinforced polymer (gfrp) composites,' *Materials Today: Proceedings*, vol. 27, pp. 1651–1654, 2020.
- [18] R. Sharma, 'Effect of obliquity of incident light on the performance of silicon solar cells,' *Heliyon*, vol. 5, no. 7, e01965, 2019.
- [19] K. Soga and H. Akasaka, 'Influences of solar incident angle on power generation efficiency of pv modules under field conditions,' *Journal of Asian Architecture and Building Engineering*, vol. 2, no. 2, pp. 43–48, 2003.
- [20] (), [Online]. Available: <http://www.solarelectricityhandbook.com/solar-angle-calculator.html> (visited on 20/05/2021).
- [21] (), [Online]. Available: <https://abaqus-docs.mit.edu/2017/English/SIMACAECSTRefMap/simacst-c-fastener.htm> (visited on 04/06/2021).
- [22] A. Echtermeyer, K. Lasn and S. Shchebetov, 'Typical static ply properties for composites,' 2013.
- [23] K. Lasn, A. Klauson and A. Echtermeyer, 'Back-calculation of elastic moduli of a ply from the moduli of cross-ply laminates,' *Mechanics of Composite Materials*, vol. 51, no. 1, pp. 55–68, 2015.
- [24] (), [Online]. Available: <http://airfoiltools.com/> (visited on 08/02/2021).
- [25] (), [Online]. Available: https://www.metyx.com/wp-content/uploads/PDF_Files/Hexion/TDS/TDS%5C%20RIMH%5C%20137.pdf (visited on 04/06/2021).
- [26] (). 'Self-locking worm gears: Fact or fiction?' [Online]. Available: <https://www.machinedesign.com/motors-drives/article/21834661/selflocking-worm-gears-fact-or-fiction> (visited on 04/06/2021).
- [27] (). 'Worms and worm gears, general basics and overview,' [Online]. Available: http://smarthost.maedler.de/datenblaetter/schnecken_EN.pdf (visited on 04/06/2021).
- [28] (). 'Rmd-x8 pro,' [Online]. Available: <http://www.gyems.cn/866757.html> (visited on 30/05/2021).
- [29] (), [Online]. Available: <https://medias.schaeffler.us/en/deep-groove-ball-bearings#19913716875> (visited on 20/05/2021).
- [30] (), [Online]. Available: <https://abaqus-docs.mit.edu/2017/English/SIMACAECSARefMap/simagsa-c-ctmmeshconverg.htm> (visited on 04/06/2021).
- [31] (), [Online]. Available: <https://www.alumeco.no/> (visited on 04/06/2021).

- [32] G. Härkegård, *Dimensjonering av maskindeler*. Fagbokforlaget, 2004.
- [33] (), [Online]. Available: <https://submer.com/blog/what-is-immersion-cooling/> (visited on 06/06/2021).
- [34] E. Greene *et al.*, 'Design guide for marine applications of composites,' Ship Structure Committee, Tech. Rep., 1997.
- [35] (), [Online]. Available: <https://www.easycomposites.co.uk/> (visited on 06/06/2021).

Appendix A

Wing Assembly Guide








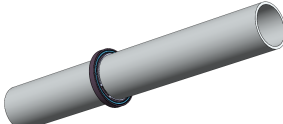
The assembly guide, as referenced to through the thesis, is an essential document for those handling this product.

Wing Assembly Guide

Read carefully before attempting to assemble the wing. A printed version of this document should always be brought along.



Components list (white for wing, green for actuation system):

	Component	Picture
1	Leading Edge	
2	Trailing Edge	
3	Side Panels, L and R	
4	Top Section Plate	
5	Middle Section Plate	
6	Bottom Section Plate	
7	Solar panel, 2pcs	
8	Mast Stub	

9	Mast	
10	A4 M6x10mm TX30, 81pcs	
11	Worm Gear	
12	Worm	
13	Gear Ring	
14	Lower Bearing Hold	
15	Upper Bearing Holds, 2pcs	
16	Motor Mounting Bracket	
17	Motor Shaft Flange	

18	Bearing Cap	
19	RMD-X8 Pro	
20	M8x20 mm, 4pcs	
21	M6x16mm, 10	
22	M6x35mm, 8pcs	
23	M5x8 mm, 2pcs	
24	M4x5mm sunk, 10pcs	
25	M4x8mm sunk, 3pcs	

Tools (white for wing, green for actuation system):

Tool	
TX30 screw driver	
H5	
H3	
H2	
PH2	

Assembly A does not need to be stored disassembled, so most of the time assembly of the wing can start from step **B0**.

A1 - Slide the Bottom Plate(4) onto the Mast Stub(8) from below. Tighten the 6 M6x16 bolts on the Bearing Cap(18)

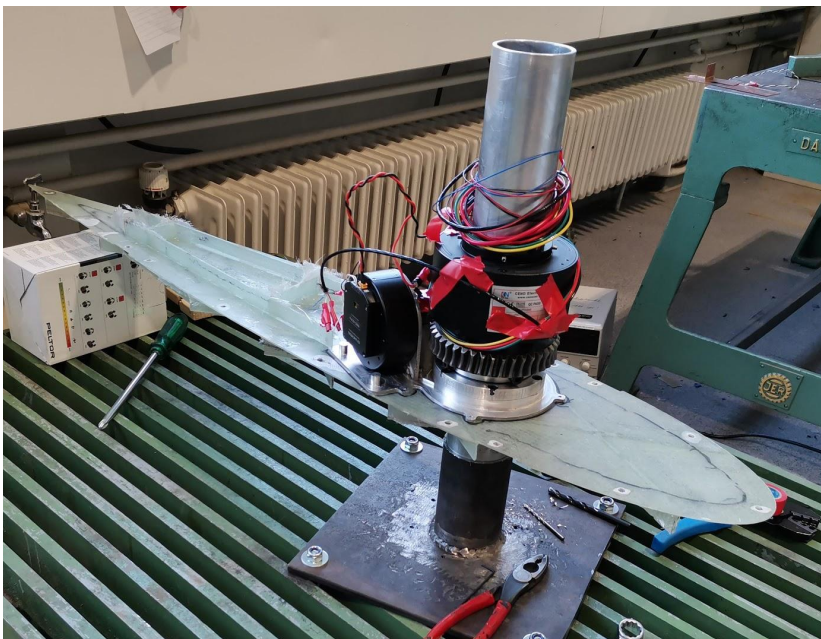
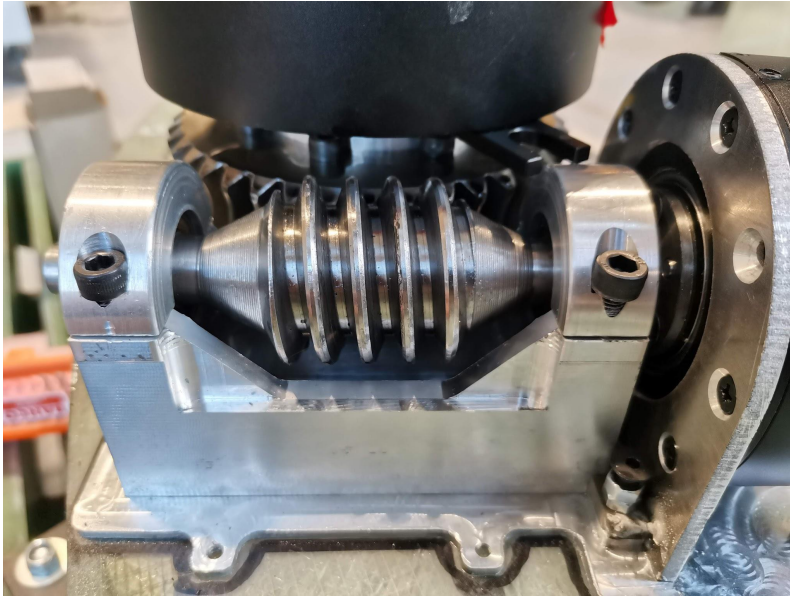
A2 - Slide the Gear Ring(13) onto the Mast Stub(8) from above. Tighten the 4 M8x20 bolts.

A3 - Slide the Worm Gear(11) onto the Mast Stub(8) from above. Engage it with the Worm(12) with bearings. Lower them until the worm gear meets the Gear Ring(13) and bearings sit into the Lower Bearing Hold(14). Tighten the 4 m6 bolts on the Upper bearing holds and 8 M6x16 bolts on the gear.

A4 - Mount the RMD-X8 Pro(19) to the Motor Mounting Bracket(16) using 10 sink head M4x5mm bolts. **DO NOT USE LONGER BOLTS!!!**, as they will engage the rotor and damage the motor. Fasten the Motor Shaft Flange(17) to the RMD-X8 Pro(19) using 3 sink head M4x8 bolts.

A5 - Insert the motor assembly such that the tap engages the groove on the Worm Shaft(12). Fasten with 2 M5 bolts.

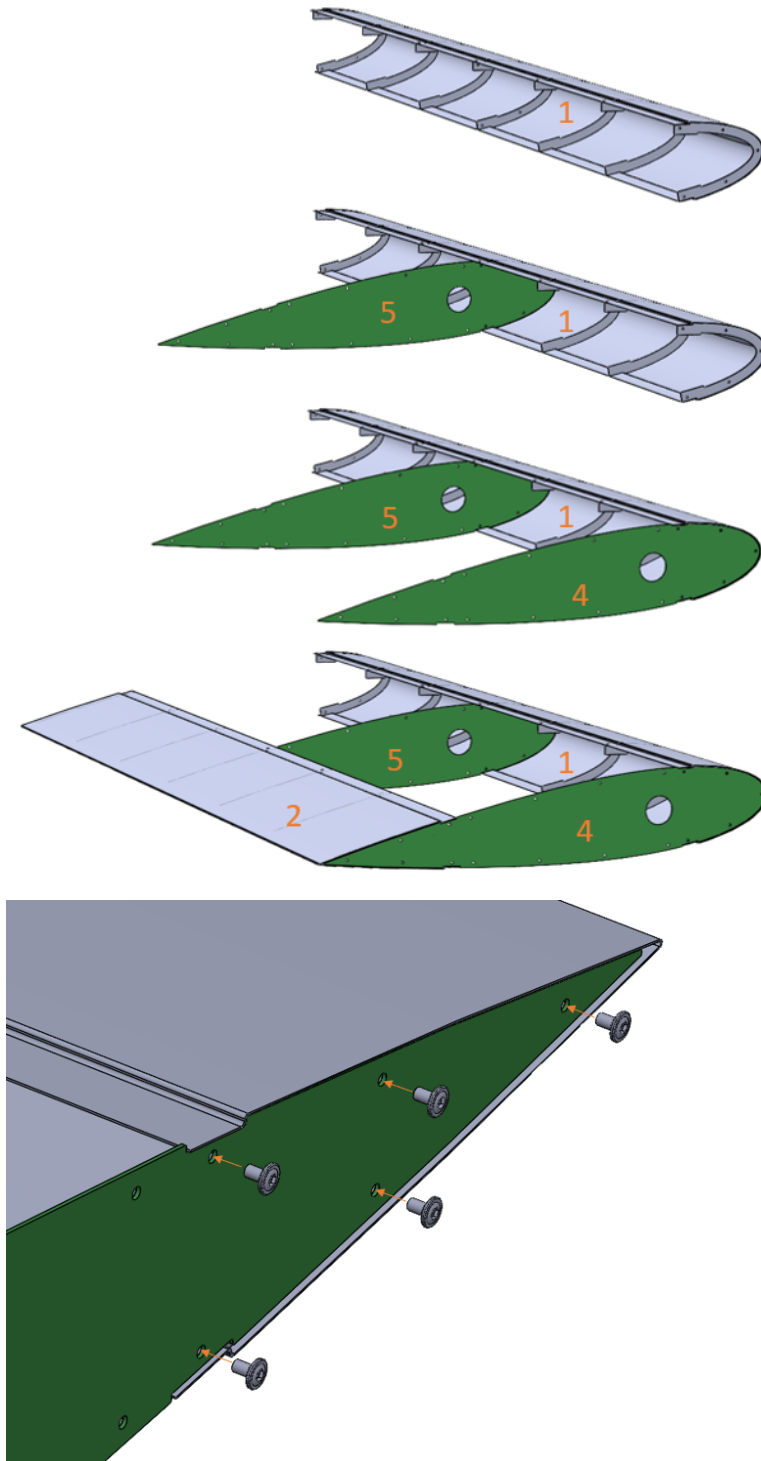
A6 - Slide the Slip Ring onto the Mast Stub. Pull the wires and seal the hole..



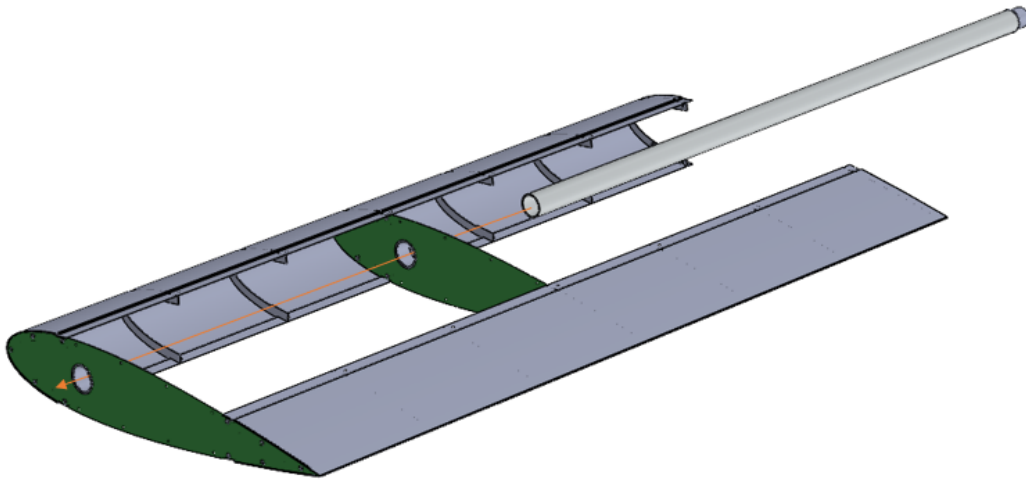
Assembly A

B0 - Place the entire assembly(A) on the boat by sliding the mast stub into the socket. Fasten. Connect wires. Perform test of function. Place and fasten box. Seal.

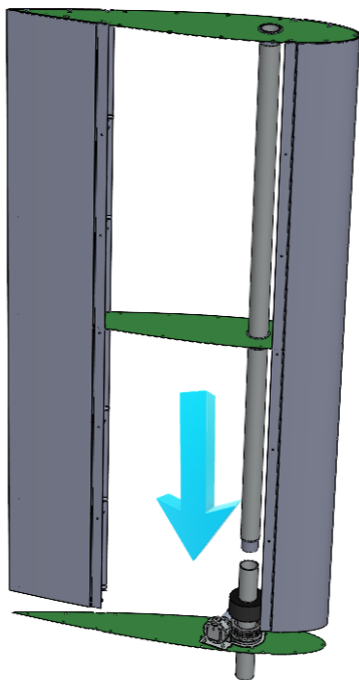
B1 - Place the Leading Edge(1) flat on the ground. Insert and fasten the Middle Section Plate(5) right above the middle flange, and Top Section Plate(4) above the top flange. Add the Trailing Edge(2). Everything fastens with the A4 M6x10mm T30 bolts, inserted from above. The top is where the flange is closest to the edge.



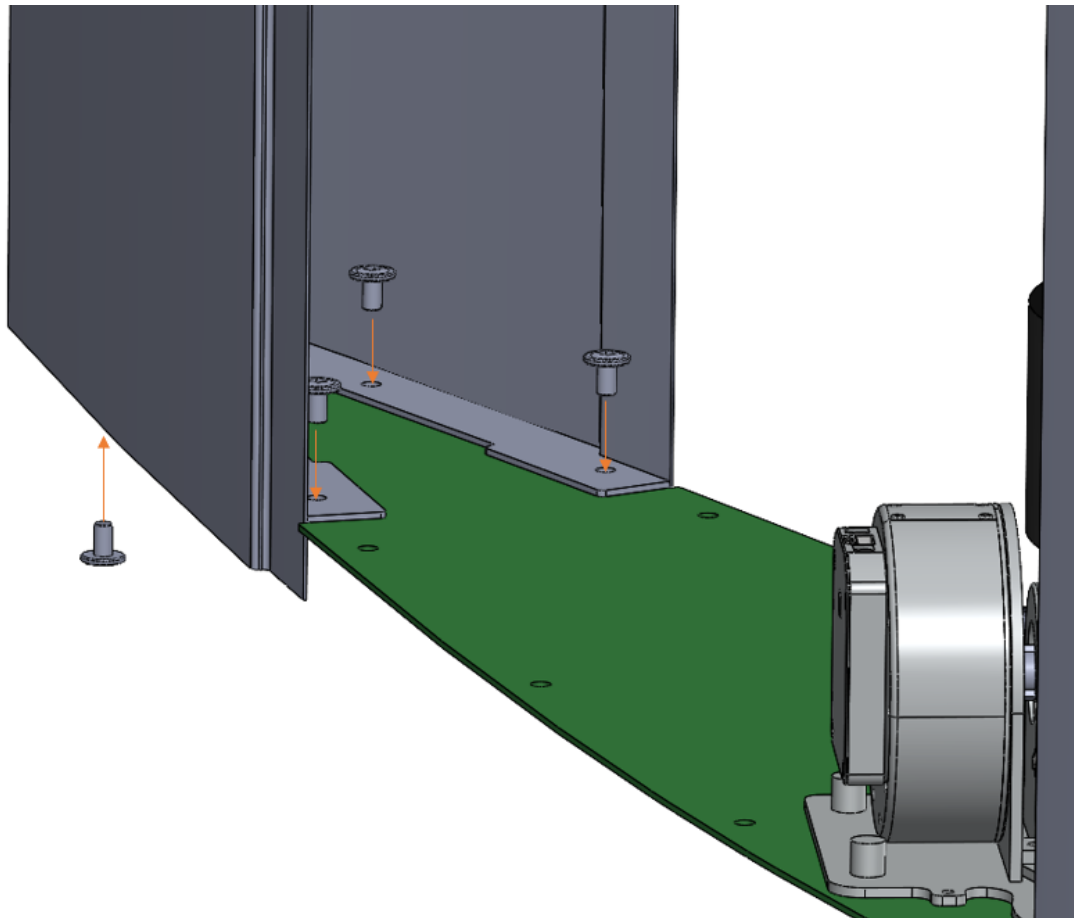
B2 - Slide the Mast(9) in through the holes in the plates.



B3 - It is recommended to be two people for this next step. Lift the whole assembly(B) from the ground and place atop the bottom plate, such that the leading and trailing edge coincide with the plate, and the Mast joint(9) slides into the Mast Stub(8).

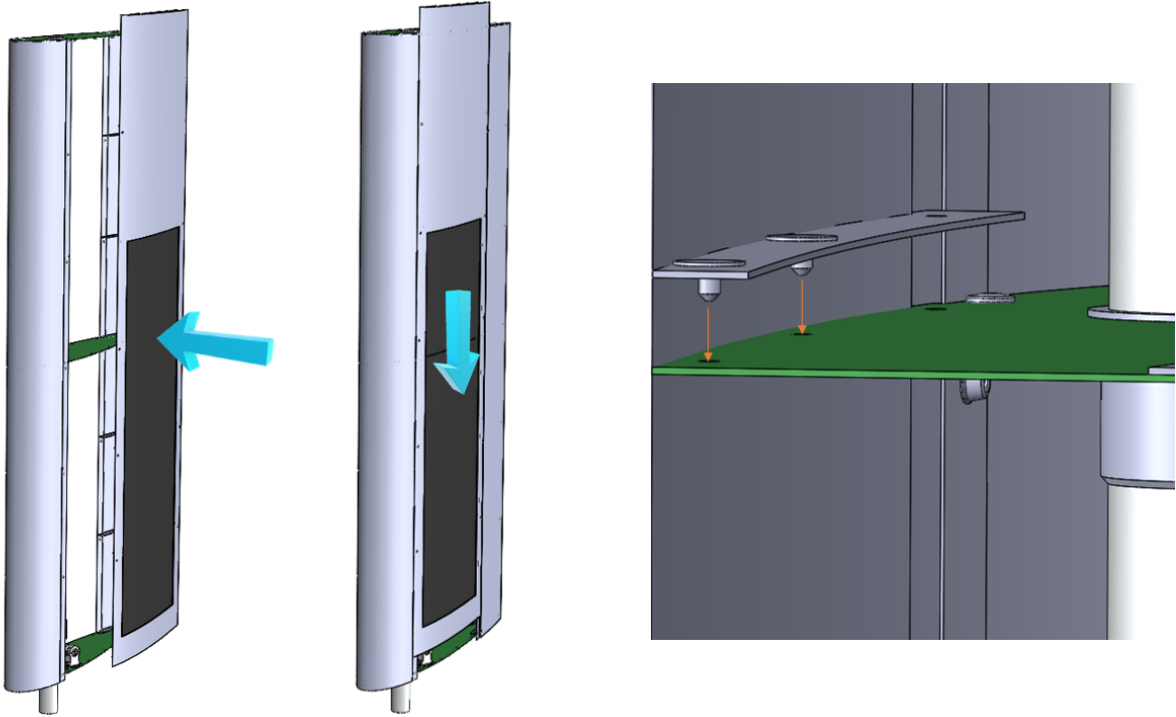


B4 - Fasten from the overside with 5 bolts through the flange of the Leading Edge and 4 through the Trailing Edge. The backmost bolt on the Trailing Edge enters from the underside.

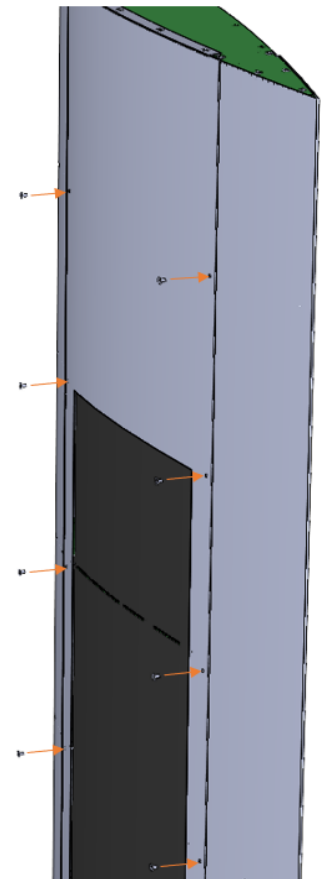
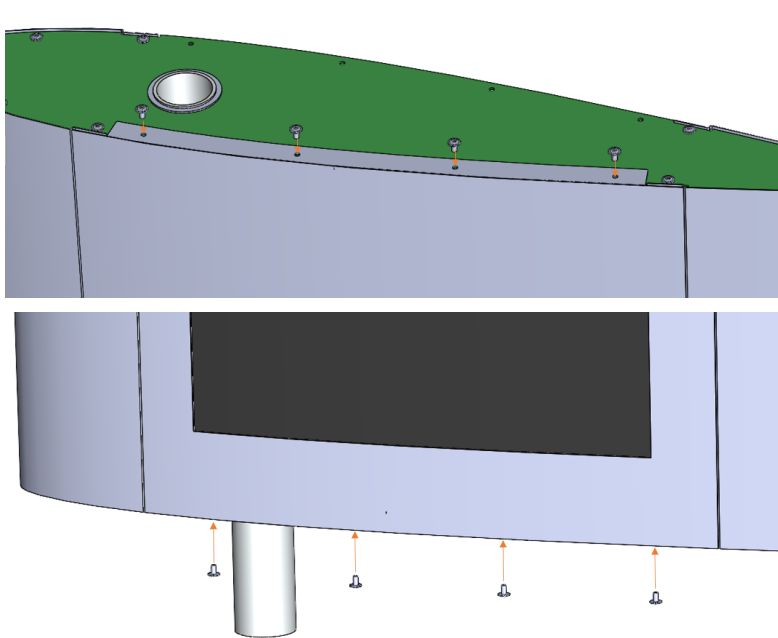


B5 - Place the Solar Panel(7) in the indent of the Side Panel(3) and thread the wire through the hole. Fasten with 8 bolts.

B6 - Connect the solar panel wires. Lift the Side Panel up, and put it to the side of the wing, slightly above its intended position. Slide it down so that the 2 taps on the middle flange enter the holes on the Middle Section Plate. The Side Panel will now maintain its position.



B7 - Fasten, in order, with 4 bolts from the top, 4 from the bottom, and 5 along each side. Insert buoyancy elements/airbags before repeating procedure **B5-B7** with the adjacent Side Panel(3).



Appendix B

Mechanical Drawings

Here are mechanical drawings of all components of the actuation/transmission system. There are also some drawings of wing components, e.g. providing details for insertion of flanges. CAD models are available from the author upon request. Do not hesitate to contact regarding this or any other information you might require.

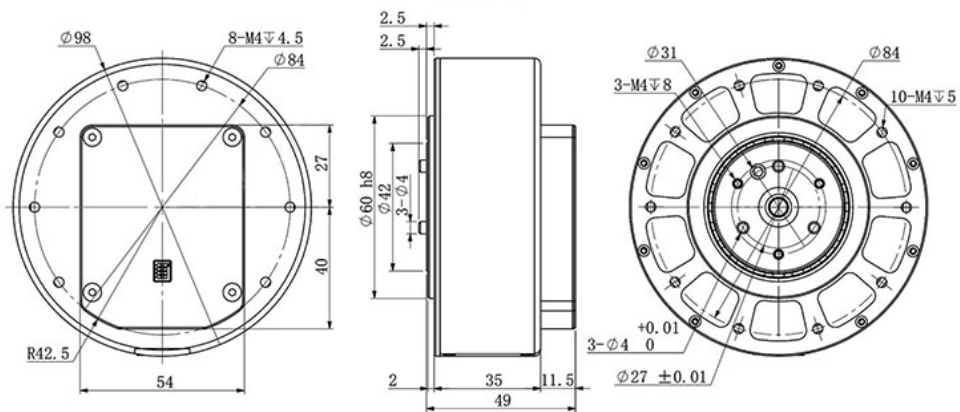
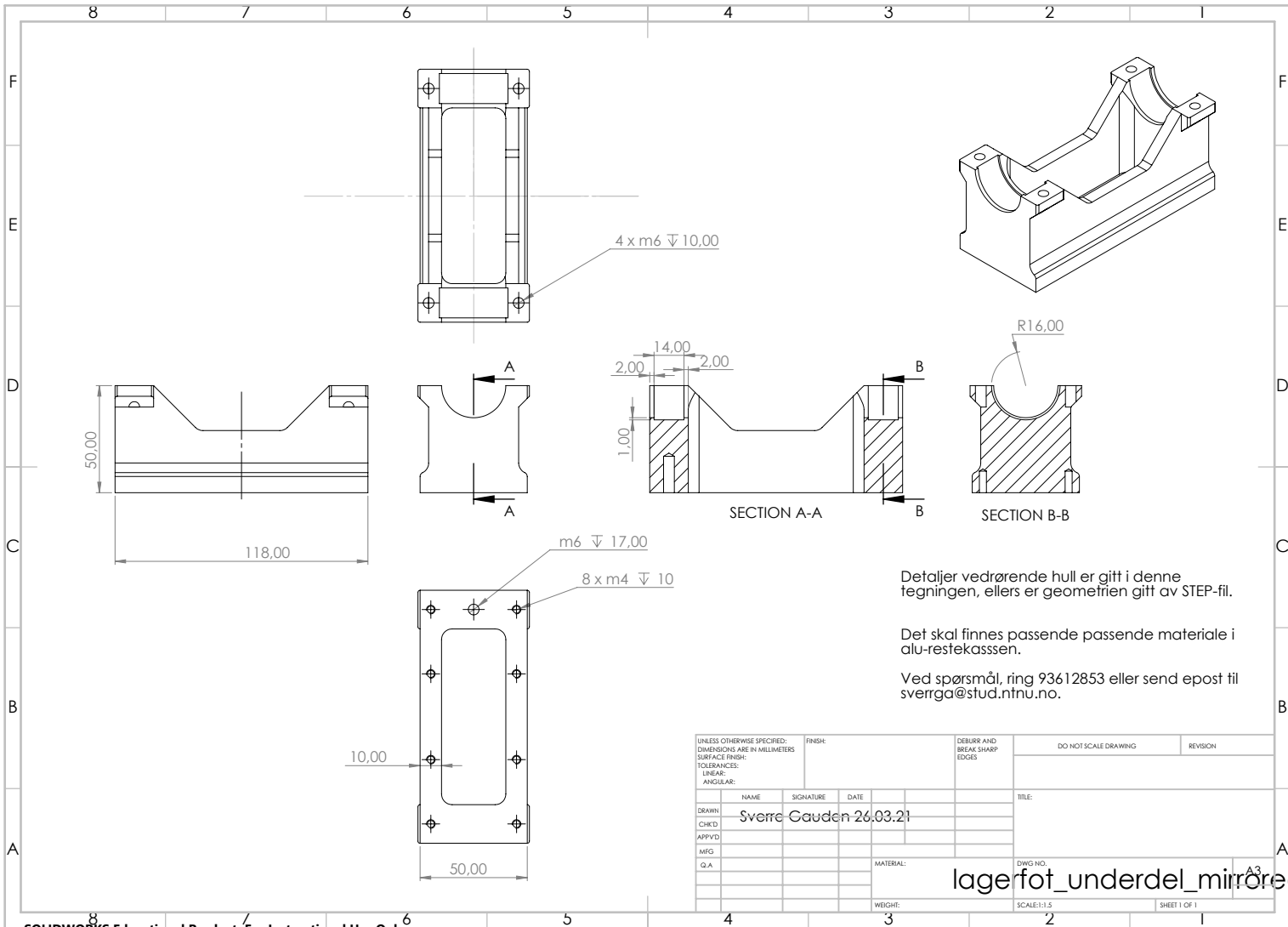
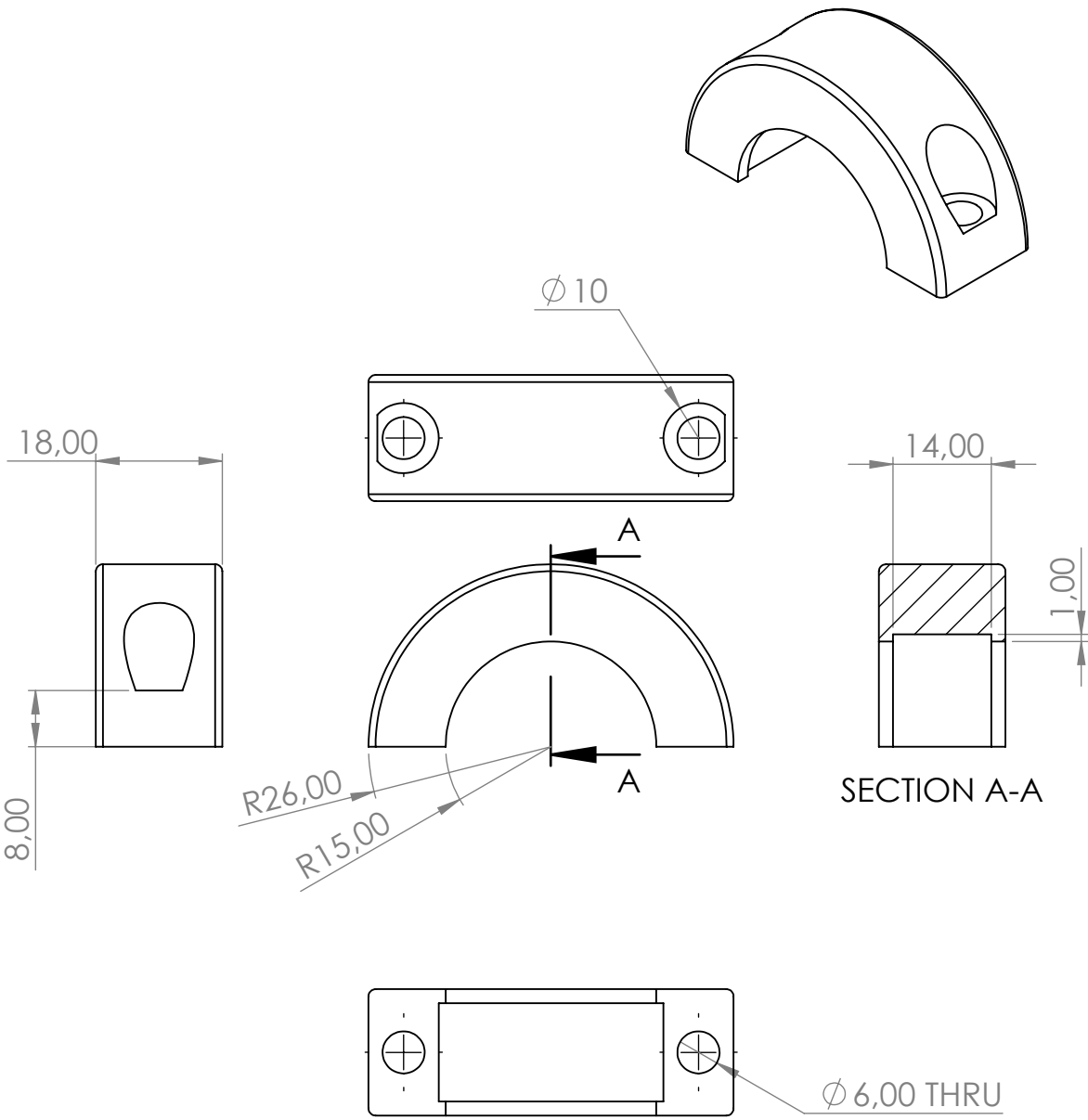


Figure B.1: RMD-X8 Pro actuator mechanical drawing.



UNLESS OTHERWISE SPECIFIED: DIMENSIONS ARE IN MILLIMETERS		FINISH:		DEBURR AND BREAK SHARP EDGES		DO NOT SCALE DRAWING		REVISION	
SURFACE FINISH:									
TOLERANCES:									
LINEAR:									
ANGULAR:									
DRAWN:		NAME	SIGNATURE	DATE			TITLE:		
CHKD:		Sverre Gauden		26.03.21					
APPVD:									
MFG:									
Q.A:					MATERIAL:		DWG. NO.:		
							SCALE: 1:1.5		
					WEIGHT:		SHEET 1 OF 1		

lagerfoto_underdel_mirrorred



2 stk av denne delen

Det skal finnes passende passende materiale i alu-restekassen.

prosjektnummer: 70442941

Ved spørsmål, ring 93612853 eller send epost til sverrga@stud.ntnu.no.

UNLESS OTHERWISE SPECIFIED:
DIMENSIONS ARE IN MILLIMETERS
SURFACE FINISH:
TOLERANCES:
LINEAR:
ANGULAR:

FINISH:

DEBURR AND
BREAK SHARP
EDGES

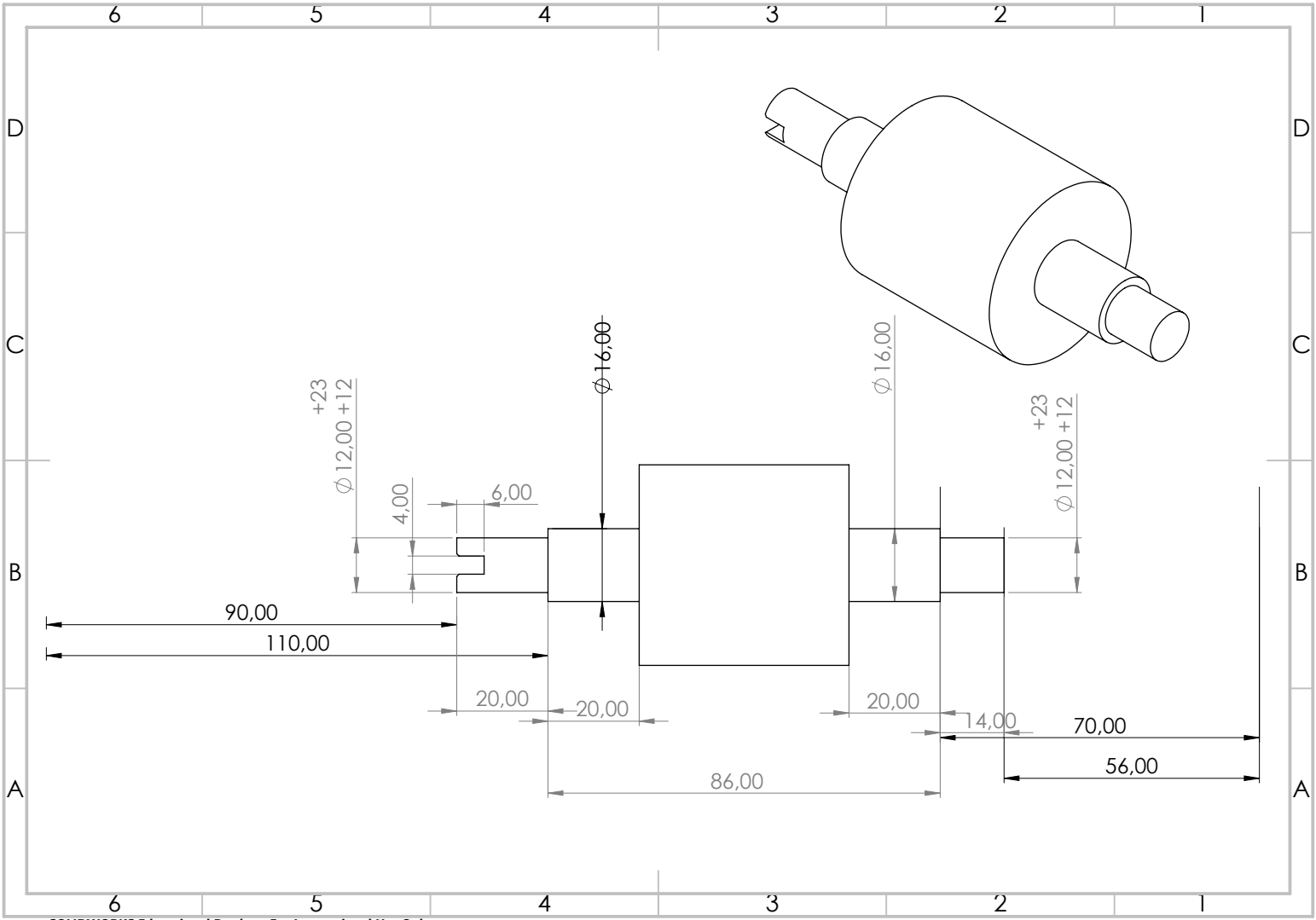
DO NOT SCALE DRAWING

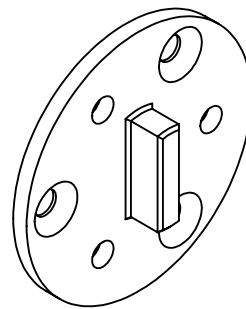
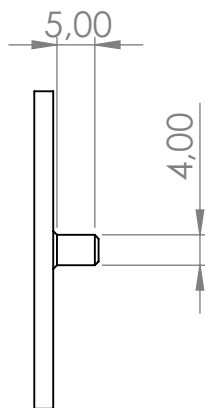
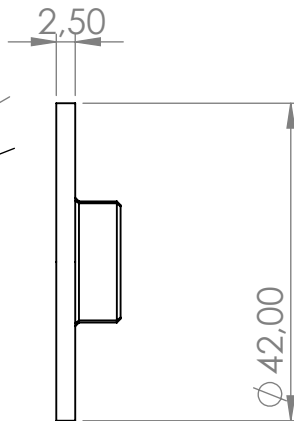
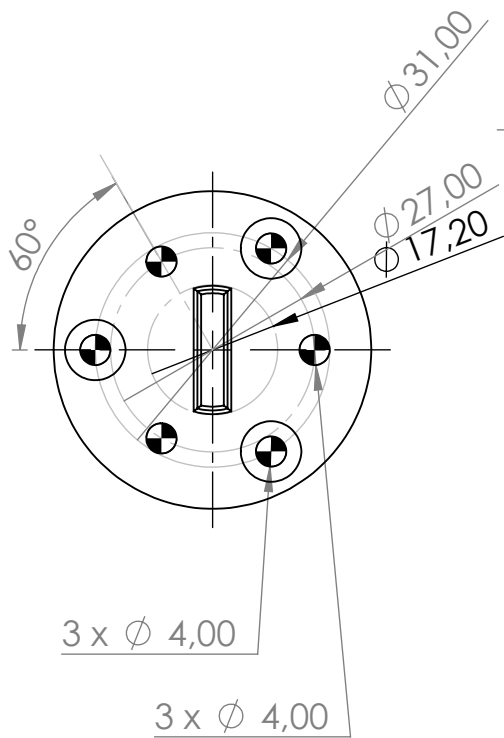
REVISION

	NAME	SIGNATURE	DATE
DRAWN	Sverre Gauder		26.03.21
CHK'D			
APPV'D			
MFG			
Q.A			

TITLE:	
MATERIAL:	Aluminium
DWG NO.	lagerfot_overde
WEIGHT:	
SCALE:1:1	SHEET 1 OF 1

A4





UNLESS OTHERWISE SPECIFIED:
 DIMENSIONS ARE IN MILLIMETERS
 SURFACE FINISH:
 TOLERANCES:
 LINEAR:
 ANGULAR:

FINISH:

DEBURR AND
 BREAK SHARP
 EDGES

DO NOT SCALE DRAWING

REVISION

	NAME	SIGNATURE	DATE
DRAWN	Sverre gauden		9.04
CHK'D			
APPV'D			
MFG			
Q.A			

TITLE:

MATERIAL:

Stainless steel AISI 316

DWG NO.

WEIGHT:

SCALE: 1:1

SHEET 1 OF 1

4 3 2 1

F

F

Kan cuttes med waterjet

maskinert overflate

Kan cuttes med waterjet

E

E

4,00

D

D

10 x ϕ 4,50
forsenket

C

C

50,00

10,00
4,00

98,00

3,00

15,00

Det skal finnes passende
passende materiale i alu-
restekassen.

Ved spørsmål, ring 93612853
eller send epost til
sverrga@stud.ntnu.no.

B

B

prosjektnummer: 70442941

UNLESS OTHERWISE SPECIFIED:
DIMENSIONS ARE IN MILLIMETERS
SURFACE FINISH:
TOLERANCES:
LINEAR:
ANGULAR:

FINISH:

DEBURR AND
BREAK SHARP
EDGES

DO NOT SCALE DRAWING

REVISION

A

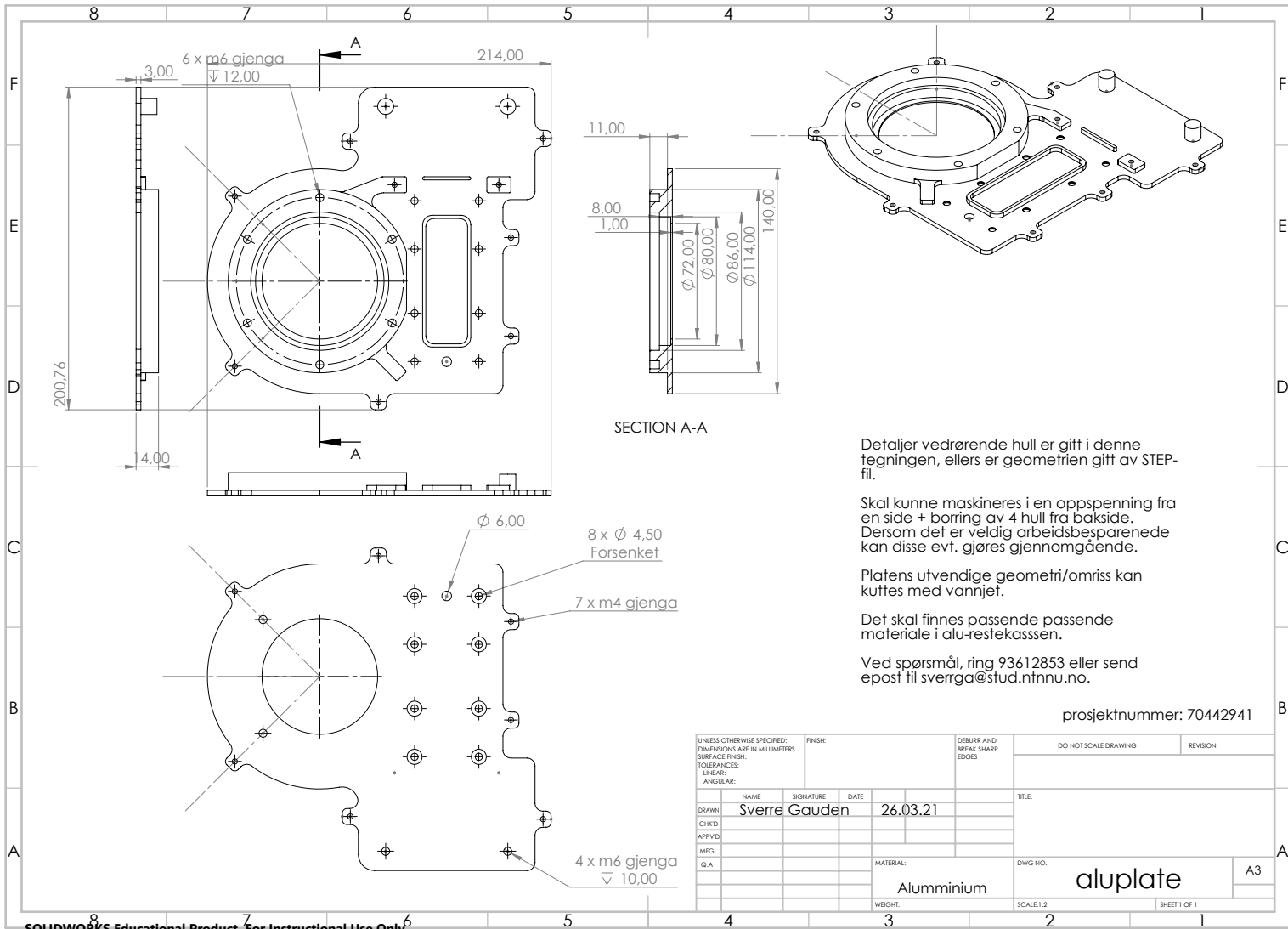
A

NAME	SIGNATURE	DATE
DRAWN	Sverre Gauden	26.03.21
CHK'D		
APPV'D		
MFG		
Q.A		

TITLE:	
MATERIAL:	Aluminium
DWG NO.	motor_mount
WEIGHT:	
SCALE:1:1	SHEET 1 OF 1

A4

4 3 2 1



Detaljer vedrørende hull er gitt i denne tegningen, ellers er geometrien gitt av STEP-fil.

Skal kunne maskineres i en oppspenning fra en side + boring av 4 hull fra bakside. Dersom det er veldig arbeidsbesparende kan disse evt. gjøres gjennomgående.

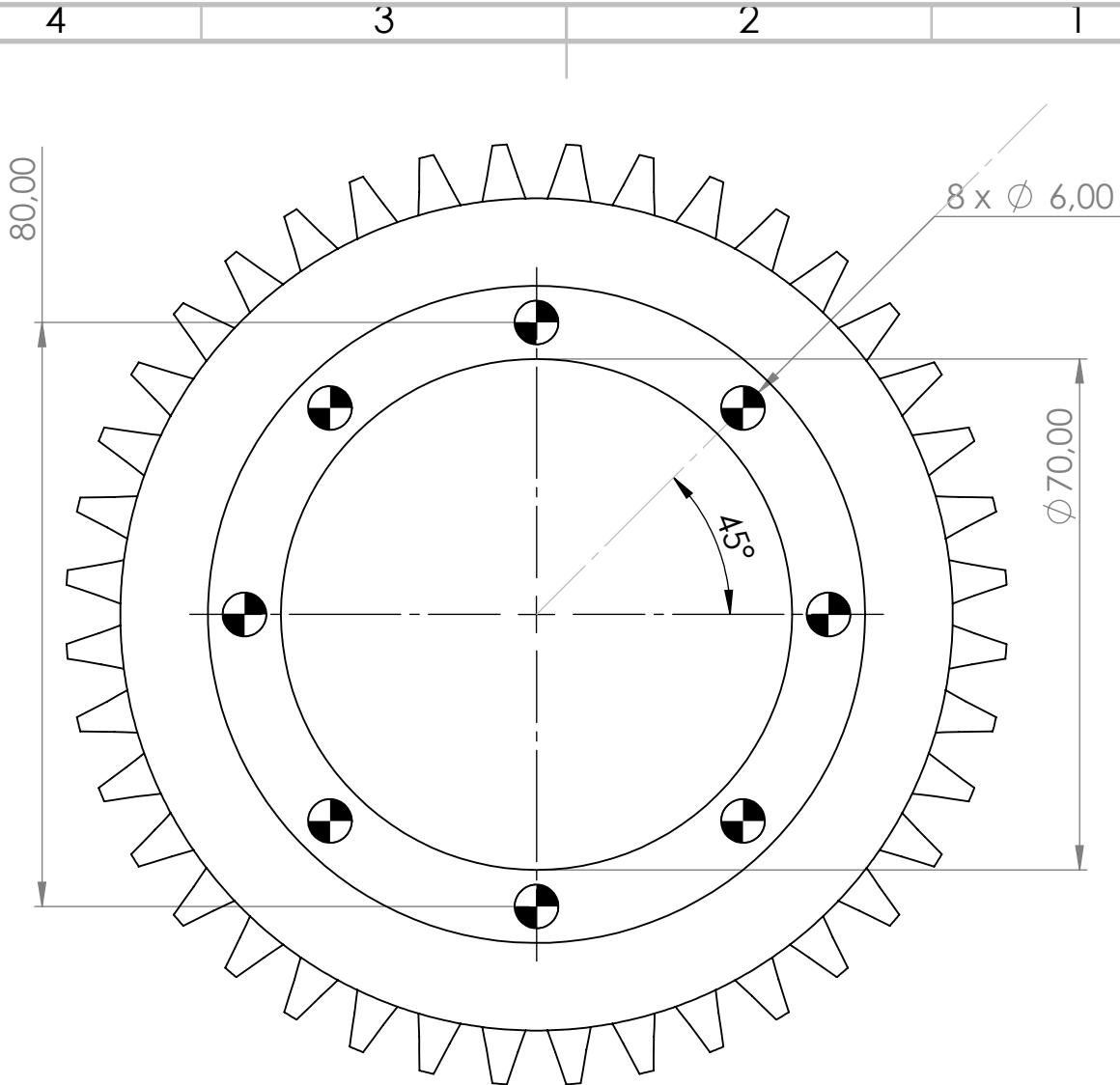
Platens utvendige geometri/omriss kan kuttles med vannjet.

Det skal finnes passende materiale i alu-restekassen.

Ved spørsmål, ring 93612853 eller send epost til sverrga@stud.ntnu.no.

prosjektnummer: 70442941

UNLESS OTHERWISE SPECIFIED: DIMENSIONS ARE IN MILLIMETERS		FINISH:	DEBURR AND BREAK SHARP EDGES	DO NOT SCALE DRAWING	REVISION
SURFACE FINISH:				TITLE:	
TOLERANCES:				DWG NO.	
LINEAR:				SCALE:1:2	
ANGULAR:				SHEET 1 OF 1	
DRAWN	NAME	SIGNATURE	DATE		
CHKD	Sverre	Gauden	26.03.21		
APPVD					
MFG					
Q.A.					
	MATERIAL:			Aluminium	
	WEIGHT:			A3	



UNLESS OTHERWISE SPECIFIED: DIMENSIONS ARE IN MILLIMETERS SURFACE FINISH: TOLERANCES: LINEAR: ANGULAR:	FINISH:	DEBURR AND BREAK SHARP EDGES	DO NOT SCALE DRAWING	REVISION

	NAME	SIGNATURE	DATE
DRAWN	Sverre Gauden		12.04.20
CHK'D			
APPV'D			
MFG			
Q.A			

TITLE:	PART- 31001800- DESC	
DWG NO.	31001800	A4
SCALE:	1:1	SHEET 1 OF 1

4 3 2 1

F

F

E

E

D

D

C

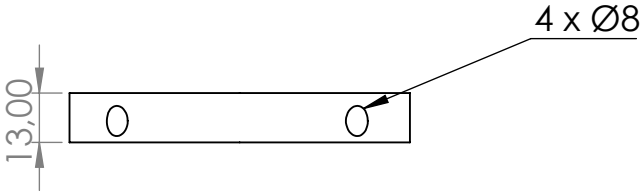
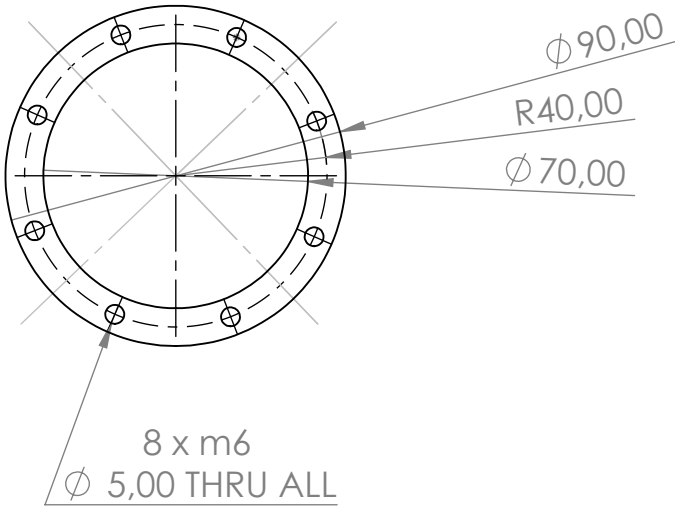
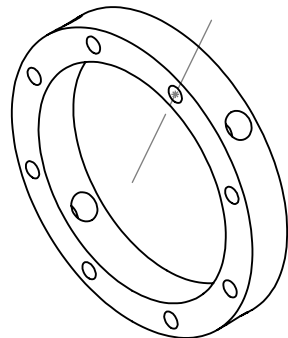
C

B

B

A

A



UNLESS OTHERWISE SPECIFIED:
 DIMENSIONS ARE IN MILLIMETERS
 SURFACE FINISH:
 TOLERANCES:
 LINEAR:
 ANGULAR:

FINISH:

DEBURR AND
 BREAK SHARP
 EDGES

DO NOT SCALE DRAWING

REVISION

	NAME	SIGNATURE	DATE	
DRAWN				
CHK'D				
APPV'D				
MFG				
Q.A				

TITLE:

MATERIAL:

DWG NO. **gearing**

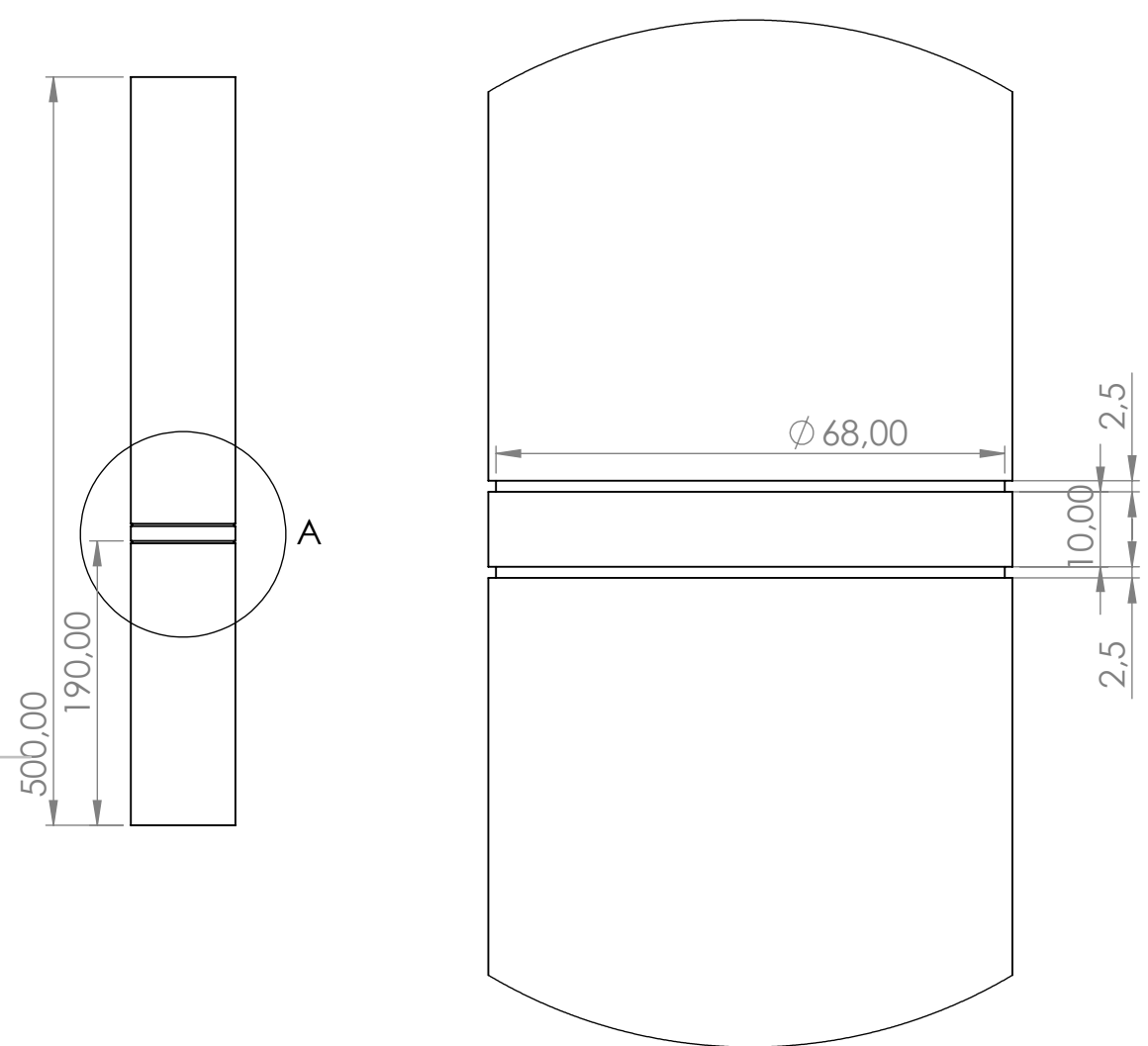
SCALE: 1:2

WEIGHT:

SHEET 1 OF 1

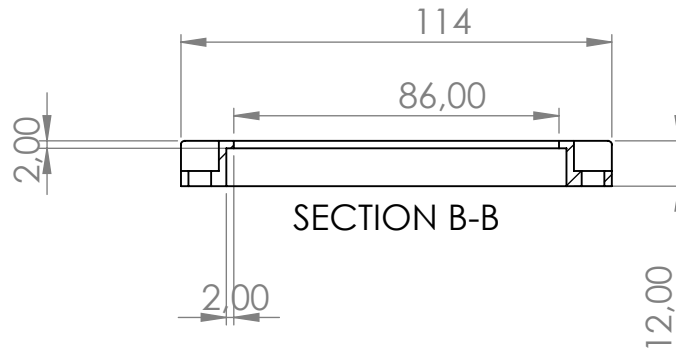
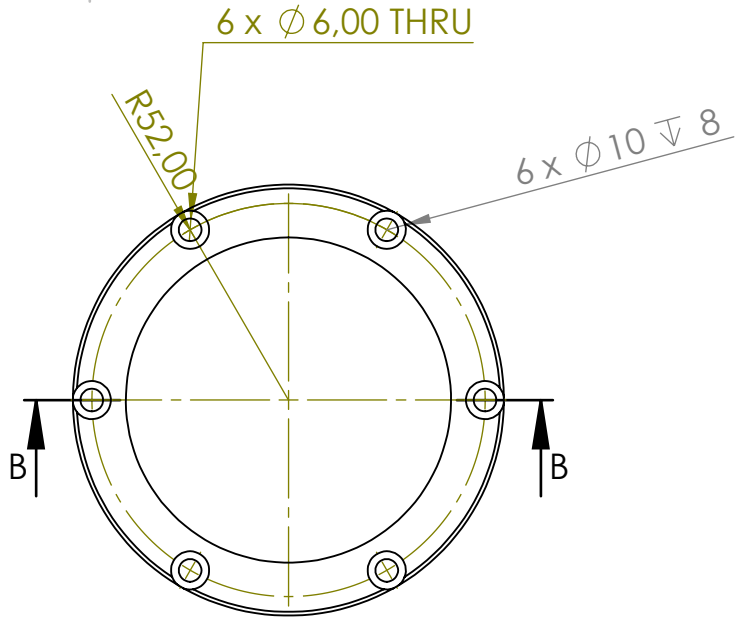
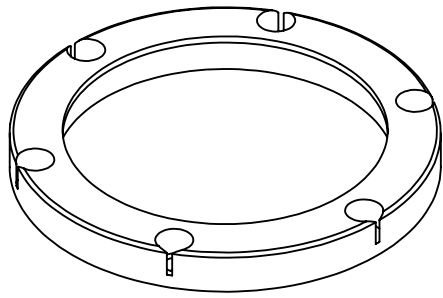
A4

4 3 2 1



DETAIL A
SCALE 1 : 1

UNLESS OTHERWISE SPECIFIED: DIMENSIONS ARE IN MILLIMETERS SURFACE FINISH: TOLERANCES: LINEAR: ANGULAR:			FINISH:	DEBURR AND BREAK SHARP EDGES	DO NOT SCALE DRAWING	REVISION
NAME	SIGNATURE	DATE			TITLE:	
DRAWN						
CHK'D						
APPV'D						
MFG						
Q.A			MATERIAL:	DWG NO.	mast_short	
					A4	
			WEIGHT:	SCALE:1:5	SHEET 1 OF 1	



Se også vedlagt STEP-fil.

Det skal finnes passende materiale i alu-restekassen.

Ved spørsmål, ring 93612853 eller send epost til sverrga@stud.ntnu.no.

UNLESS OTHERWISE SPECIFIED:
DIMENSIONS ARE IN MILLIMETERS
SURFACE FINISH:
TOLERANCES:
LINEAR:
ANGULAR:

FINISH:

DEBURR AND
BREAK SHARP
EDGES

DO NOT SCALE DRAWING

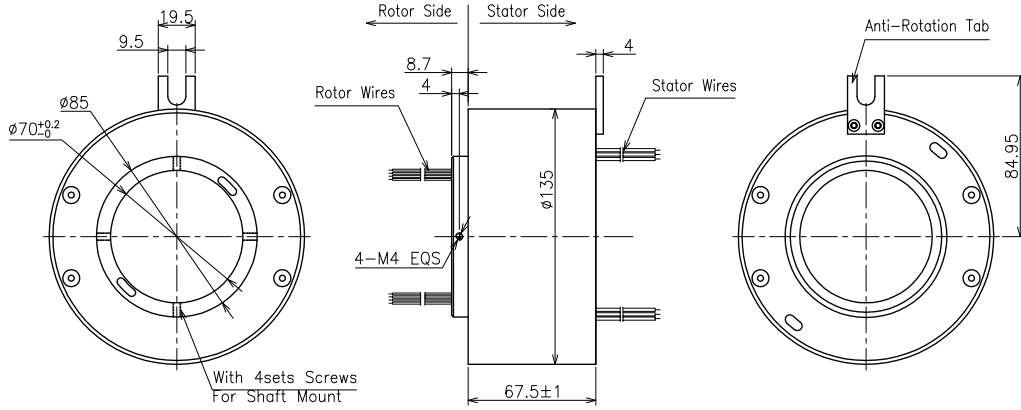
REVISION

	NAME	SIGNATURE	DATE
DRAWN	Sverre Gauden		26.03.21
CHK'D			
APPV'D			
MFG			
Q.A			

TITLE:	bearing_cup_drawing
DWG NO.	
MATERIAL:	aluminium
WEIGHT:	
SCALE: 1:2	SHEET 1 OF 1

Model: ECN070-04P3-04S

Mark	Content of amendment	Date	Draw	Approve



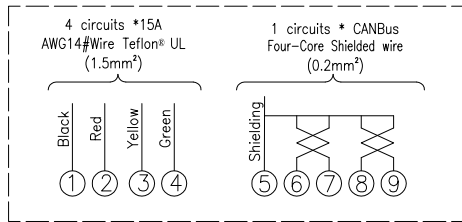
Technical parameters:

Protection(IP Grade): IP51
 Working Humidity: 60%RH
 Working Temperature: $-20^{\circ}\text{C} \sim +60^{\circ}\text{C}$

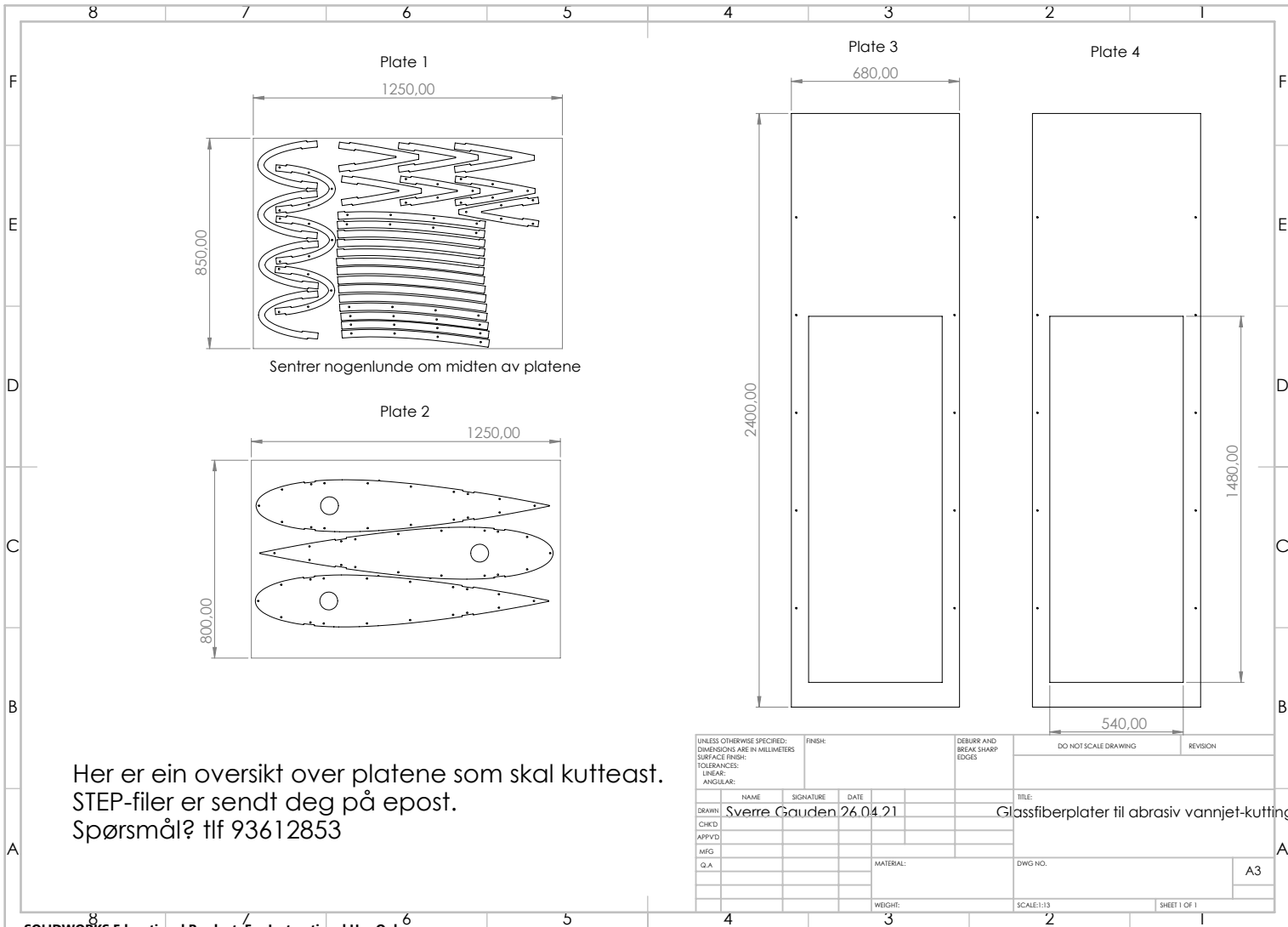
Lead Wire Size: AWG14# Wire Teflon® UL
 Four-Core Shielded wire
 Rating Voltage: 0~380VAC/VDC
 Circuits & Current: 4 circuits * 15A;
 1 circuits * CANBus(Signal)
 Dielectric Strength: $\geq 1500\text{VAC}@50\text{Hz(Power)}$
 $\geq 300\text{VAC}@50\text{Hz(Signal)}$
 Insulation Resistance: $500\text{M}\Omega@500\text{VDC(Power)}$
 $100\text{M}\Omega@100\text{VDC(Signal)}$
 Electrical Noise: Max $30\text{m}\Omega$ (50rpm)

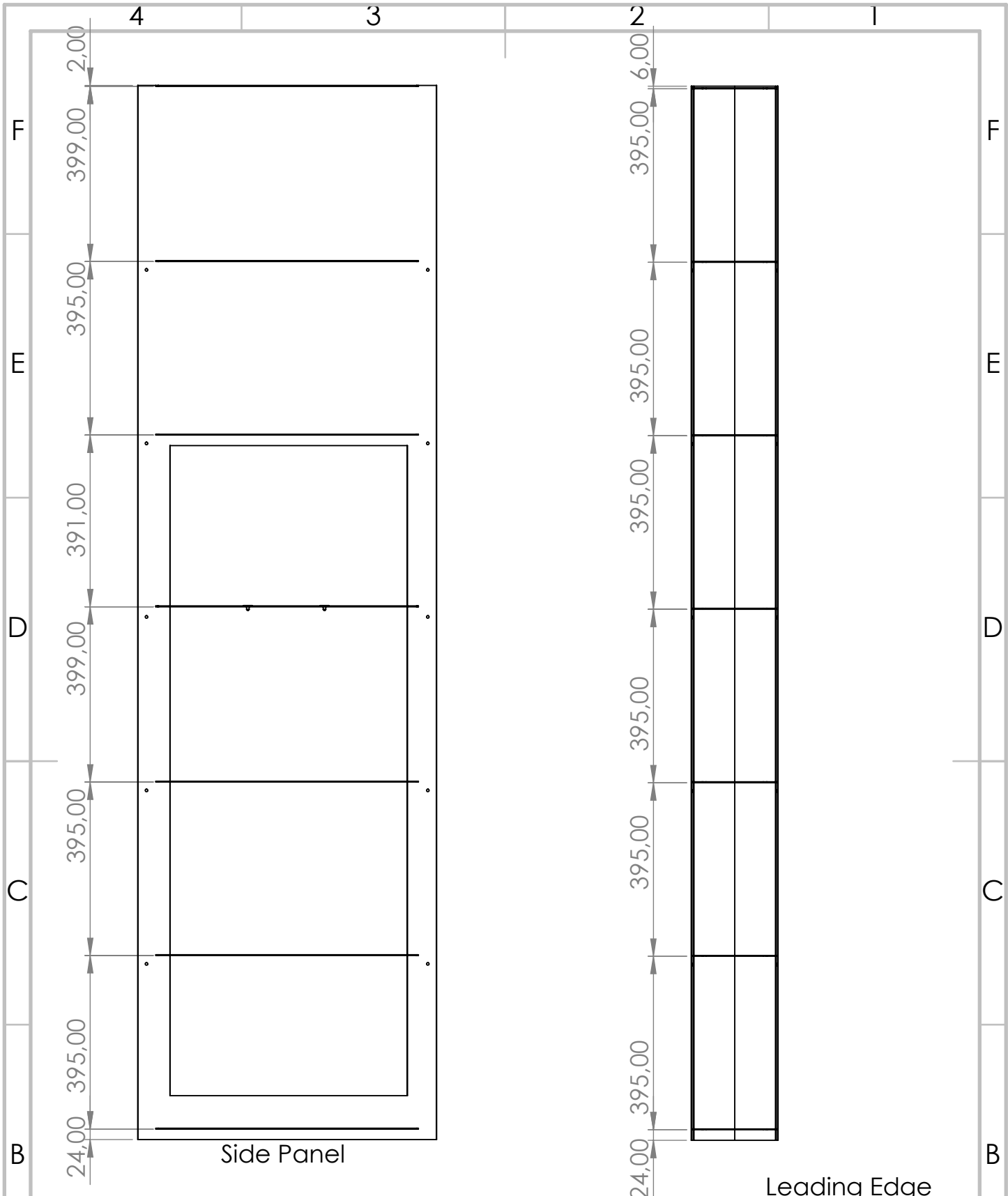
Lead Wire Length: Rotor: 300mm
 Stator: 300mm
 Working Speed: 0~50rpm
 Rotation Way: Fix up stator side with
 anti-rotation side Shaft drives rotor running
 Contact Material: Precious Metal
 Housing Material: Aluminum alloy
 Inner Diameter: $\phi 70\text{mm}$

Wiring Diagram



SLIPRING CENO Electronics Technology Co.,Ltd(ShenZhen)							
Unit	mm	Tol Unless Specified	Model	ECN070-04P3-04S			
Scale	1:1	LINEAR 0~18 ±0.1 >18~80 ±0.15 >80~250 ±0.2 ANGLE ° ±0.5	Title	Outline drawing			
Qty			Part No.				
Design	Sail	Date	2021.03.26	Material			
Checked	Guohui Rao	Date	2021.03.26	Finished			
Technics		Date		Rev	S0	Customer type	A
Standardization		Date		Proj		Page	1/1
Quality Countersign		Date					
Approve		Date					





UNLESS OTHERWISE SPECIFIED:
DIMENSIONS ARE IN MILLIMETERS
SURFACE FINISH:
TOLERANCES:
LINEAR:
ANGULAR:

FINISH:

DEBURR AND
BREAK SHARP
EDGES

DO NOT SCALE DRAWING

REVISION

NAME	SIGNATURE	DATE
DRAWN		
CHK'D		
APPV'D		
MFG		
Q.A		
MATERIAL:		
WEIGHT:		

TITLE:

Flange placement.
Measurements are from/to
underside of the flanges.

DWG NO.

Assem_side

A4

SCALE:1:12

SHEET 1 OF 1

Appendix C

Previous FEA

Results of the FEA campaign of the feasibility study for the wing design performed in [10]. 10 analyses performed with various boundary conditions, load and layups. Referred to in subsection 3.1.1.

Boundary conditions	Constraints	Layup	Load	U _{max}	Tsai-Hill	Comments	
a	End 1 flange fixed	Ends and middle sections constrained	Skin: 0/90/+45/+45/0 and flanges: 0/90/+45/+45/0/sym	500 N pressure 300 N endpoint load	<2 mm	<0.1	Local buckling behaviour of panel close to base
b			200 Nm torsion	<0.5 mm	<0.1		
c			700 Nm pressure	<1mm	<0.1	Very low deflections so far. Unrealistic or overdimensioned?	
d	3 point supported beam:	Ends and middle sections constrained.	700 Nm pressure	1.9 mm	<0.2	Trailing edge panel cave in.	
e	End 1 fixed.		500 Nm torque	2.4 mm	<0.2		
f	Middle and end2:		700 Nm pressure	2.0 mm	<0.2		
g	U1=U2= UR1=UR2=0		700 Nm pressure	2.74 mm	<0.2		
h			700 Nm pressure				
i	Mast end encastered (200mm from wing bottom)	End 1 locked to mast. Mid+end2 free to rotate about mast.	700 Nm pressure	23 mm	<0.2, except base flange: 0.9	Mast bending dominated deflection. Peak T-H most likely due to nature of constraint.	
j			500 Nm torque	7.4 mm	<0.2		

Appendix D

Relevant Data Sheets

TECHNICAL DATASHEET

SAP No. 30009055 Article Description X-E-302g/m²-1270mm

Textile Structure 7008669 SAERTEX®

ARTICLE CONSTRUCTION (in accordance with EN 13473-1)

Layer	Construction	Areal weight	Tolerance	Material
4	45 °	145 g/m ²	+/- 5,0 %	E-glass 200 TEX
3	90 °	4 g/m ²	+/- 5,0 %	E-glass 68 TEX
2	0 °	2 g/m ²	+/- 5,0 %	E-glass 68 TEX
1	-45 °	145 g/m ²	+/- 5,0 %	E-glass 200 TEX
Stitching		6 g/m ²	+/- 1 g/m ²	PES [Polyester] 76 dtex

Fiber input can be determined individually

FURTHER CHARACTERISTICS

Gauge	5,0	Stitching pattern	warp	Width (nominal)	1270 mm
Stitch length	3,00 mm	Total tolerance	+/- 5,2 %	Total areal weight	302 g/m ²

Labelling (Standard) Every roll is equipped with a label in the core. A further label is located outside on the foil or on the box.

Packaging (Standard) Every roll is wound on a cardboard core and wrapped in foil. Further packaging options can be determined individually.

Storage With original packaging: No moisture recommendation and direct sunlight. To avoid problems with humidity and electrostatic charge, fabrics to be conditioned 24 hours prior to processing, independent of storage conditions.

Fibre Specifics	EC9-33X1TEX	
Weave	2 x 2 Twill	

Weight and Dimensions

Thickness	0.2	mm
Width	1000	mm
Consolidated Thickness	0.2	mm
Areal Weight	200	g/m ²

Product Data

Colour	White	
Format	Woven Fabric	
Fibre Type	Glass Fibre	

Mechanical Properties

Ends	13	/cm
Picks	13	cm

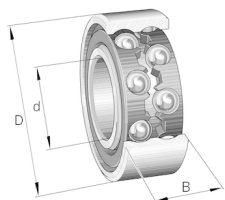
Compatible With

Compatible With	Epoxy	Yes
Compatible With	Polyester	Yes
Compatible With	Vinylester	Yes

General Properties

Gross Weight	0.2	kg
--------------	-----	----

Figure D.1: [0/90] woven fabric data sheet.



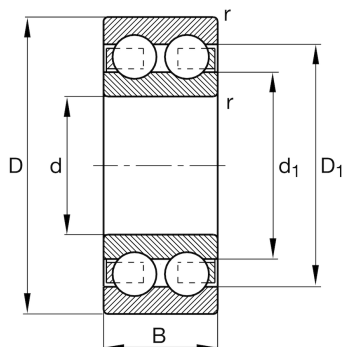
FAG

4201-BB-TVH

Deep groove ball bearing

Schaeffler ID:
0219415050000Deep groove ball bearing 42...BB-TVH,
double row, plastic cage

Technical information

**Main Dimensions & Performance Data**

d	12 mm	Bore diameter
D	32 mm	Outside diameter
B	14 mm	Width
C_r	11,100 N	Basic dynamic load rating, radial
C_{0r}	6,100 N	Basic static load rating, radial
C_{ur}	320 N	Fatigue load limit, radial
n_G	19,000 1/min	Limiting speed
n_{gr}	19,100 1/min	Reference speed
	51 g	Weight

Dimensions

r_{min}	0.6 mm	Minimum chamfer dimension
D_1	25.8 mm	Shoulder diameter outer ring
d_1	17.8 mm	Shoulder diameter inner ring

Mounting dimensions

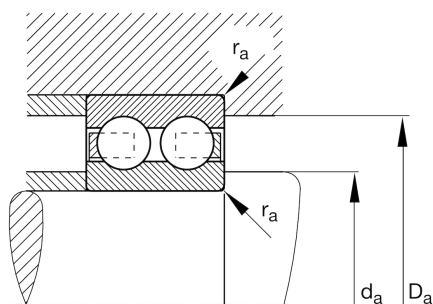
$d_{a min}$	16.2 mm	Minimum diameter shaft shoulder
$D_{a max}$	27.8 mm	Maximum diameter of housing shoulder
$r_{a max}$	0.6 mm	Maximum fillet radius

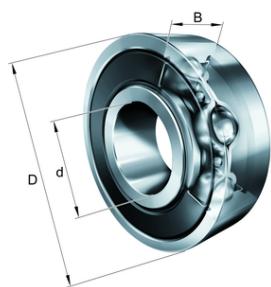
Calculation factors

f_0	12.3	Calculation factor
-------	------	--------------------

Temperature range

T_{min}	-20 °C	Operating temperature min.
T_{max}	120 °C	Operating temperature max.





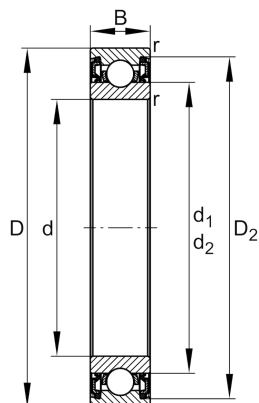
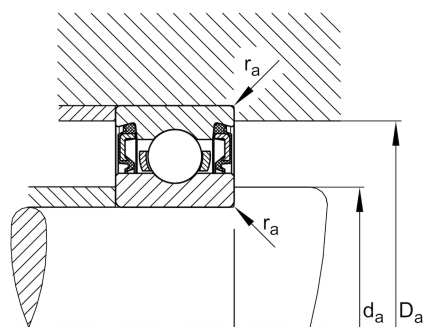
FAG

61814-2RZ-Y

Deep groove ball bearing

Schaeffler ID:
0797294600000Deep groove ball bearing 618..-2RZ-Y,
single row, shields, brass sheet metal cage

Technical information

**Temperature range**

T_{\min}	-20 °C	Operating temperature min.
T_{\max}	110 °C	Operating temperature max.
	0.14 kg	Weight

Main Dimensions & Performance Data

d	70 mm	Bore diameter
D	90 mm	Outside diameter
B	10 mm	Width
C_r	13,200 N	Basic dynamic load rating, radial
C_{0r}	12,400 N	Basic static load rating, radial
C_{ur}	820 N	Fatigue load limit, radial
n_G	9,000 1/min	Limiting speed
n_{gr}	5,300 1/min	Reference speed

Dimensions

r_{\min}	0.6 mm	Minimum chamfer dimension
D_2	85.5 mm	Caliber diameter outer ring
d_1	76.6 mm	Shoulder diameter inner ring

Mounting dimensions

$d_{a\min}$	73.2 mm	Minimum diameter shaft shoulder
$D_{a\max}$	86.8 mm	Maximum diameter of housing shoulder
$r_{a\max}$	0.6 mm	Maximum fillet radius

Calculation factors

f_0	16.1	Calculation factor
-------	------	--------------------

产品参数 PRODUCT PARAMETERS		
产品型号 (Item name)		RMD-X8 PRO
匝数 (Turns)	T	13
额定电压 (Nominal voltage)	V	48
空载转速 (No-load Speed)	rpm	225
额定转速 (Nominal Speed)	rpm	155
额定电流 (Nominal current)	A	6.5
额定功率 (Nominal power)	W	330
额定扭矩 (Nominal torque)	N.M	13
最大瞬时电流 (Max stall current)	A	12.5
最大瞬时扭矩 (Max stall torque)	N.M	35
线电阻 (resistance)		0.55
接线方式 (wire connect)		Y
相间电感 (Phase to phase inductance)	mH	0.54
转速常数 (Speed constant)	rpm/v	30
扭矩电流常数 (Torque constant)	N.M/A	3.30
径向负载 (Radial load)	N	1200
轴向负载 (Axial load)	N	300
转子惯量 (Rotor inertia)	gc m ²	1450
极对数 (Number of pole pairs)		20
电机重量 (Motor weight)	g	710
工作温度范围 (working temperature)	°C	(-20 ~ 80 °C)
最高退磁温度 (Max demagnetize temperature)	°C	120°C
减速机速比 (Reducer ratio)		6:1
减速箱背隙 (Backlash)	Arc min	5
适配驱动类型 (Drive)		DRC20
驱动器输入电压范围 (input voltage)	V	12-50
驱动器电流范围 (Current)	A	Normal : 15A Instant: 30A
额定功率 (Normminal power)	W	700
通信方式 (Communication)		CAN BUS
编码器 (encoder)		16bit magnetic encoder
波特率 (baudrate)	bps	1M
通信频率 (Communication frequency)	HZ	2K
控制频率 (Control frequency)		Torque loop:32KHZ Speed loop:8KHZ Position loop :4KHZ
控制模式 (control mode)		Torque loop/speed loop/position loop
加速度曲线 (S-Curve)		YES
地址选择开关 (ID switch)		YES
接插件 (connector)		XT2.0
温度传感器 (temperature sensor)		YES

Figure D.2: RMD-X8 Pro actuator data sheet.

